

Fluorine-Free approach to fabrication of liquid repelling surfaces

*This Thesis is submitted in partial fulfilment of the requirements for
the Degree of Doctor of Mechanical Engineering.*

Norbert Jaroslaw Janowicz

Supervised by Professor M. K. Tiwari, I. Papakonstantinou, C. J.

Carmalt, I. P. Parkin

University College London

Department of Mechanical Engineering

2021

Declaration

I, Norbert Jaroslaw Janowicz, confirm that the work presented in this thesis is wholly my own. Where information has been derived and obtained from other sources, I confirm that this has been indicated as such.

Acknowledgments

I would like to extend by deepest gratitude to Professor Manish Tiwari for always finding the time to talk to me when work was getting to me and being very understanding of any situation that came up that diverted my attention from the work. Thank you also for reminding me that a PhD is not something to be taken lightly and reminding me that “I could do your research in a week if I had the time and I could walk you through it in a month but that is not why I am here. It is your PhD and what you make of it. I see the potential in you to be one of the greats and am waiting for you to see that.” This encouragement was what kept me going to finish the project.

Thanks to Professors Ivan Parkin and Claire Carmalt for spending a good half hour every other week wondering what is it that I am telling them about and always finding a way to bring me down to earth and organise my work so that it makes sense. The time working on developing me into a researcher is much appreciated.

Professor Ioannis Papakonstantinou, thank you for showing me that a PhD is not only doing the lab work and making fancy coatings, but it is also understanding why they work. Early on in my first year you had meetings with me attempting to go through what now seems a basic introduction book to Wetting and Capillarity and I gave nothing but blank face back at you. This has resulted in me reading around the subject so that I could avoid looking that way again.

Finally like to thank my family and friends who have always supported me in this crazy time where I was quitting at least 10 times a day and running away at least once a month. Big shout out to my fiancé Shay for putting up with me constantly asking for some feedback.

Abstract

This thesis presents research into enhancing durability of transparent fluorine-free superhydrophobic surfaces through the hybridisation of polydimethylsiloxane (PDMS) with titanium dioxide. Sample preparation was achieved via a variety of wet deposition techniques such as spray coating, spin coating and aerosol assisted chemical vapour deposition (AACVD) resulting in self-cleaning, near transparent and durable materials.

To address the main concern of adhesion and durability of transparent coatings containing PDMS, metal oxide hybridisation was achieved resulting in nano-pockets of titanium within the network that showed little to no detrimental effect on the transparency reaching 89% compared to glass 94%. As such, when combined with anatase and fumed silica, it resulted in a stable coating that showed self-cleaning through Cassie-Baxter wetting and resistance to UV over 21 days as shown with a stable water contact angle above 160° and no change in FTIR analysis.

Finally, a composite consisting of 3-Aminopropyltriethoxysilane (APTES) functionalised porous silica (25% mass grafted) and the hybrid Ti-PDMS was used as the precursor mixture for transparent (90%) superhydrophobic (168°) coatings achieved through AACVD with high durability of more than 25 abrasion cycles and homogenous in wetting behaviour pillar like structures. The coating was also shown to be self-cleaning with droplet roll off due to Cassie-Baxter wetting.

Impact Statement

The work conducted throughout this doctorate has been focused on the design and application of titanium hybrid polydimethylsiloxane (PDMS) in Cassie-Baxter durable and transparent superhydrophobic coatings. This was achieved through a greener fluorine-free approach with a variety of coating methods.

The overall approach to the surface modifications was aimed to facilitate the process and increase scalability, as such nanocomposites were the primary focus as the precursor mixtures. This has focused the initial stages of the project around the key components: particles and polymer. As such, reproducible and scalable synthesis of structured silica particles was optimized from a previously reported method. The resulting particles demonstrated uniform hexagonal porosity of 3 nm and particle size of 120 ± 5 nm even in the scaled up system. Due to the polar nature of the synthesis, 3-Aminopropyltriethoxysilane (APTES) functionalisation was designed to improve dispersibility of the particles in organic solvents and reduce agglomeration to further benefit the transparency of manufactured coatings.

Hybrid polymers consisting of inorganic and organic components have been gaining popularity in recent years due to the ability to not only maintain most of the desired properties of the polymer but further enhance and tailor functionalities based on the metal oxides used for crosslinking. As such this work tailored titanium isopropoxide crosslinking of PDMS, first as hydroxy terminated then optimized for commercial Sylgard 184 without additional binding sites for which typically platinum catalyst is used for bridging. The films

showed hydrophobic behaviour even at 120 : 1 ratio of titanium to PDMS and exhibited excellent transparency of up to 89% compared to 93% for untreated glass.

The hybrids were then applied as coatings by forming a composite from anatase particles and fumed silica as stability dopants for self-cleaning and photoactive coatings. The surfaces achieved contact angles of 164° and exhibited stability when exposed to UV rays for 21 days. The addition of the titanium in the polymer seemed to enhance the anatase properties and cause a weakening of the properties of the polymer causing discolouration at higher concentrations whilst the lower concentration seems to have benefited the stability of the coating.

Finally, several coating methods were used to benefit on the properties achieved from the particles and the hybrid polymer to fabricate durable and transparent coatings. First, spray coating was used to optimize composite preparation and to assess the potential of the hybrid polymer using off the self particles as a coating. This resulted in improved adhesion of 12° based on one tape peel test cycle however it was hypothesised that the transparency and durability might benefit from a different approach. To that extent a single type of composite was tested using spin coating and aerosol assisted chemical vapour deposition (AACVD) which resulted in coatings exceeding current literature with transparency comparable to glass, contact angles of 168° and durability of over 25 sandpaper abrasion cycles.

Therefore, considerable advancements to the field of polymer hybridisation and surface wettability have been recorded in the three research streams presented

in this thesis. The research developed materials not only show high applicability in both industrial and commercial settings but with small refinements and further tests, have potential to be marketable coatings, especially in the case of the hybrid photocatalytic coatings.

Contents

Declaration	i
Acknowledgments	ii
Abstract	iv
Impact Statement	v
List of Equations	xi
List of Figures	xii
List of Tables	xix
Abbreviations	xxi
General Introduction	1
1.1 Defining surface wetting behaviour	2
1.1.1 Young State	6
1.1.2 Surface morphology directed states of wetting: Wenzel, Cassie-Baxter and Transition states	9
1.1.3 Sliding Angle and Contact angle hysteresis.....	13
1.2 Liquid repellence in nature	15
1.3 Reducing surface energy and the hazards of fluorinated silanes	21
1.4 Surface fabrication methods.....	27
1.6 Design and application of superhydrophobic coatings	32
1.6.1 Anti-Icing.....	35
1.6.2 Self-Cleaning	35
1.6.3 Anti-corrosion.....	35
1.6.4 Drag Reduction.....	36
1.6.5 Bactericide	36
1.6.6 Oil-water separation.....	36
1.7 Design and application of Superoleophobic surfaces.....	37

1.8 Summary	39
Fabrication of APTES functionalised silica nanoparticles with high control over pore size and shape	42
2.1 Introduction.....	42
2.1.1 Synthesis of silica nanoparticles with controlled morphology.....	44
2.1.2 Functionalisation of silica nanoparticles.....	48
2.2 Chapter outlook	49
2.3 Experimental	50
2.3.1 Materials	50
2.3.2 Particle synthesis and functionalisation with APTES	51
2.3.3 Characterization.....	53
2.4 Results and Discussion	54
2.4.1 Chemical composition.....	54
2.4.2 Particle morphology	58
2.5 Conclusion.....	59
Titanium dioxide hybridization of polydimethylsiloxane for applications in photo responsive superhydrophobic coatings	60
3.1 Introduction.....	60
3.1.1 Titanium hybridization of PDMS for additional functionalities.....	61
3.1.2 Titanium photocatalysts and its place in liquid repelling coatings	63
3.2 Chapter Outlook	66
3.3 Experimental	68
3.3.1 Materials	68
3.3.2 Metal Oxide Crosslinking	69
3.3.3 Liquid repelling coatings	70
3.3.5 Characterization.....	72
3.3.6 Functionality.....	73

3.4 Results and Discussion	73
3.4.1 Polymeric network	73
3.4.2 Characterisation of coatings	76
3.4.3 UV stability study	88
3.4 Conclusion	90
Assessing coating methods for non-polar solvent based scalable fabrication of transparent and fluorine-free superhydrophobic nanocomposite coatings.....	93
4.1 Introduction	93
4.1.1 Formulating stable nanocomposites for non-polar solvent coatings .	96
4.1.2 Understanding the principles of optical properties of particle roughened surface modifications	98
4.2 Chapter outlook.....	101
4.3 Experimental	104
4.3.1 Materials	104
4.3.2 Nanocomposite synthesis	104
4.3.3 Spray Coating	105
4.3.4 Spin Coating	106
4.3.5 Aerosol Assisted Chemical Vapour Deposition (AACVD)	106
4.3.6 Curing	107
4.3.7 Characterization.....	108
4.3.8 Functionality and durability assessment	109
4.4 Results and Discussion	110
4.4.1 Spray Coating	110
4.4.2 Spin Coating	120
4.4.3 Aerosol Assisted Chemical Vapour Deposition (AACVD)	129
4.4.4 Comparison of fabricated coatings	137

4.5 Conclusion.....	149
Conclusion	151
Publications.....	158
References.....	159
Appendix	189

List of Equations

Equation 1.1 Components of the net force in one direction of the phase interfaces: α , β , and θ are the angles shown in Figure 2; γ_{xy} is surface energy between indicated phases. ⁴⁰	5
Equation 1.2 Young's equation. The relation of the surface tensions between the three phases. ²⁹	7
Equation 1.3 The Tadmor equation for calculating the equilibrium contact angle. ⁴³	8
Equation 1.4 The spreading coefficient (S) by Dupré and Drying parameter (D) by Quéré. ^{42,44}	8
Equation 1.5 The Young-Dupré equation combining the spreading coefficient and Young's equation. ^{42,44,45}	9
Equation 1.6 The Wenzel equation relating the roughness to contact angle.	9
Equation 1.7 Cassie's law and Cassie-Baxter equation for calculating apparent contact angle of heterogenous rough surfaces. ³¹	11
Equation 1.8 Simplified version of the Cassie-Baxter model proposed by Quéré <i>et al.</i> ⁴⁹	12

Equation 1.9 Condition required for the transition between Cassie & Baxter and Wenzel state: θ_c – critical contact angle; ϕ – interphase fraction of the drop contact with surface; r – roughness of the solid (in case of flat surfaces $r = 1$). 12

Equation 1.10 Contact angle hysteresis where $\Delta\theta$ is the hysteresis, θ_A is the advancing and θ_R is the receding contact angles..... 14

Equation 1.11 The relationship between surface tension and contact angle at equilibrium.26

List of Figures

Figure 1.1 Wetting behaviour of water on a solid (a) Low contact angle and low wetting (b) Intermediate (c) High contact angle and high wetting3

Figure 1.2 Representation of the coexistence of the three phases and their contact angles both in (a) diagram and in (b) Neumann's triangle5

Figure 1.3 Young relation and derived three states of wettability.^{30,31,41}6

Figure 1.4 Schematic of sliding angle by tilting the solid until droplet just starts rolling. Sliding angle is represented by θ . The arrow represents the rolling direction of the droplet. 13

Figure 1.5 Schematic representation of the “Petal effect” mechanism of high adhesion superhydrophobic surface. 13

Figure 1.6 Morphological analysis of the lotus leaf and microscopic analysis of water droplet on the surface of the leaf.²⁶ 16

Figure 1.7 Cicada insect wing structure analysis.²⁷ 17

Figure 1.8 Illustration of (a) True hierarchical and (b) pseudo hierarchical structures. (l_1 and l_2 represent the hierarchical difference in length)..... 18

Figure 1.9 SEM images of <i>T. bielanensis</i> . showing papillose structures covered by a rhombic comb-like nano tubercles mesh. ⁶¹	20
Figure 1.10 Silanization process forming a layer of functional groups between the liquid and the solid where the r-group represents any functionality of the selected silane. ^{62,63}	21
Figure 1.11 Schematic illustrations of our AACVD coating procedure using a nanocomposite.....	27
Figure 1.12 Schematic of dip coating process showing immersion (left); withdrawal (middle) and drying (right). ⁹⁵	29
Figure 1.13 Schematic illustrations of Spin coating procedure.....	30
Figure 1.14 Schematic illustrations of Spray coating procedure.....	31
Figure 1.15 (a) Image of droplets on a superhydrophobic coating with contact angle measured. ⁸² (b-c) SEM images of Cu/CuO@PFDTCS micropillar arrays. ¹¹⁹ (e-f) contact angle and sliding angle of different liquids on Cu/CuO@PFDTCS micropillar arrays. ¹¹⁹	33
Figure 1.16 (a) Schematic representation of spray coated superoleophobic coating. ¹⁶⁸ (b) SEM image of re-entrant geometry with schematic hypothesized liquid interaction of PC–nanoparticle composite surface. ¹⁷⁵ (c) SEM images of arrays of 3D printed doubly re-entrant pillars with various magnifications. ¹⁷⁶ (d) Example of various oils repelled by superoleophobic coatings. ¹⁷¹	38
Figure 1.17 Flow diagram illustrating the key concepts for achieving the desired product.....	39
Figure 2.1 Examples of mesoporous silica particles and their key fabrication steps.	43

Figure 2.2 Schematic representation of spherical mesoporous silica synthesis using a cationic surfactant for example CTAB (a) 3D and (b) 2D.	45
Figure 2.3 Visualization of the effect functionalization of the silica particle has on dispersion in solvent.	49
Figure 2.4 Schematic representation of spherical mesoporous silica synthesis and APTES functionalisation (a-b) Micelle formation and arrangement (c) Particle formation (d) Particle functionalization.	51
Figure 2.5 Chemical analysis of the particles (a) ATR-FTIR; (b) ²⁹ Si-ssNMR and (c) TGA of both mesoporous and APTES functionalized silica (the a indicates area of loss of moisture and b indicates area of loss of amino functionality from APTES).....	55
Figure 2.6 Morphology analysis of the (a-b) SEM of mesoporous silica (c) TEM of mesoporous silica and (d) SEM of amorphous silica.	58
Figure 3.1 Theorised polymer network resulting hybrid network.	62
Figure 3.2 Heterogeneous photocatalytic mechanism with TiO ₂ as a semiconductor.	64
Figure 3.3 Applications of titanium dioxide in superwetting materials (a) Self-cleaning windows ²⁷² (b) anti-fogging surfaces ²⁷³ (c) oil-water separation mesh ¹¹⁷ (d) photocatalytic paints ²⁸⁹ (e) Water purification membranes ²⁷⁶ (f) Micro-reaction arrays ²⁷⁷	65
Figure 3.4 Analysis of hybrid polymeric networks by (a) Contact Angle Measurements (b) Transparency measurements done using UV-Vis.....	74
Figure 3.5 Chemical analysis of the polymer films by (a) XPS Ti2p spectra of samples A0 – E0 and (b) ATR-FTIR analysis.	75

Figure 3.6 Schematic describing the fabrication of the photocatalytic coatings A – E . The first step was to fabricate the Ti-PDMS hybrid polymer network to which the particles and carboxylic acid was added.....	77
Figure 3.7 Characterisation of samples A - E (a) Contact angle measurements (b) ATR-FTIR chemical analysis (c) and (d) SEM images of samples A and E at two different magnifications.	78
Figure 3.8 Characterisation of samples A1 – A6 (a) Contact angle measurements (b) ATR-FTIR chemical analysis (c) Carbon XPS elemental analysis of samples A1 – A3 (d _{i-iii}) and (e _{i-iii}) SEM images of samples A4 – A6 at two different magnifications respectively.....	83
Figure 3.9 Characterisation of samples F – H (a) Contact angle measurements (b) ATR-FTIR chemical analysis (c) and (d) SEM images of samples at two different magnifications.	86
Figure 3.10 UV exposure study on the effect of titanium crosslinker on the stability of the coating over duration of 21 days as analysed by (a-d) ATR-FTIR for each sample in order A, C, E , and H respectively (e) key for FTIR graphs (f) Image of the coating before and after exposure and (g) Contact angle measurements.	89
Figure 4.1 Visual representation of Rayleigh and Mie Scattering.....	100
Figure 4.2 (a) Preparation of Sylgard 184 (b) Preparation of TiO-PDMS hybrid (c) diagram representation of the hybrid PDMS and (d) formation of the nanocomposite.....	105
Figure 4.3 Schematic illustrations of our Spin coating procedure.....	106

Figure 4.4 Curing process demonstrating the reaction between the metal oxide sites and glass substrate. Silica particles were not shown in this diagram for clarity.⁸ 108

Figure 4.5 Sonication effect analysis using RX300 at constant concentration and spray passes. (a) contact angle (b) transparency and (c) AFM topologies. 112

Figure 4.6 Wetting and Transparency analysis and morphology analysis of the selected spray coated samples. (a) Contact angle measurements (b) photon transmission data (c) SEM images of the optimal coatings (RX6B- left, MP5B- middle and FMP7A- right) (d) AFM morphology and phase analysis (RX6B- left, MP5B- middle and FMP7A- right). 114

Figure 4.7 Comparison of the selected coatings for the standard and the hybrid RX300 series (a) Contact angle and (b) photon transmission..... 117

Figure 4.8 Adhesion tape test of the selected nanocomposite concentrations for RX300; MNPS120; FMNPS120; and RX300Ti (hybrid). 119

Figure 4.9 Visualization of the effect functionalization of the silica particle has on dispersion in solvent. 121

Figure 4.10 Morphology and chemical analysis of SC1A (a) SEM-EDS analysis with data in table. Evaluated zone shown in (ai) and data in (aii). SEM images of spin coated samples (b-j) where (b-d) is SC1A (e-g) SC2A and (h-j) SC3A... 124

Figure 4.11 (a) ATR-FTIR sample analysis and (b) UV-Vis analysis of coatings with varying particle concentrations (wt%) and heat treatment. 126

Figure 4.12 Functionality analysis of coatings by (a) dynamic contact angle measurements showing advancing contact angle (θ_A) and hysteresis ($\Delta\theta$) and (b) AFM morphology analysis of SC3A..... 128

Figure 4.13 Morphology and chemical analysis of AACVD sample (a-b) SEM of AD3A (c) SEM-EDS analysis with composition map where Si - blue, Ti - yellow and O - pink. (d) ATR-FTIR of the coating (e) XPS survey spectra..... 132

Figure 4.14 Schematic of the hypothesized annealing process for the conversion of titanium oxide particles to anatase.^{8,334} 133

Figure 4.15 Functionality analysis of coatings (a-b) Advancing contact angle and hysteresis of samples with varying (a) temperature and (b) particle concentration (c) UV-Vis analysis of coatings based on change in deposition time (AD1A15-60) and particle conc. (AD1-3A) (d) AFM 3D imaging of AD1A. 134

Figure 4.16 Morphology and wettability comparison. SEM analysis of (a) AD1A (b) is SC1A (c) SC2A and (d) SC3A. Influence of (e) particle concentration and (f) temperature on dynamic contact angles of coatings fabricated by both methods (g) self-cleaning of AD1A sample showing before, during and after cleaning. AFM study of (h) SC3A and (i) AD1A. 138

Figure 4.17 SEM images depicting the impact of (a) film growth time³³⁹ (b) temperature³⁴⁰ (c) concentration and choice of precursor³⁴¹ and (d) carrier solvent³⁴² on the morphology of thin films as prepared by AACVD.³³⁸..... 141

Figure 4.18 Functionality test (a) Cyclic tape peel test to assess substrate adhesion and durability of coatings. AACVD sample are stable well above 10 cycles. (b) Sandpaper abrasion test of AD1A showing durability above 25 linear abrasion cycles. AFM characterization of the surface of AD1A (c) before and (d) after the sandpaper test.⁸ 143

Figure 4.19 Surface morphology comparison between (a) AD1A sample and (b-c) two other coatings from literature fabricated using AACVD.^{82,83} 148

Figure 5.1 Summary of Chapter 2.....	155
Figure 5.2 Summary of Chapter 3.....	156
Figure 5.3 Summary of Chapter 4.....	157
Supplementary Figure 1 Sonication study of 41 %w/w RX300 coating (a) Contact angle measurements (b) Photon transmission test results (c) AFM topographic analysis	190
Supplementary Figure 2 Full contact angle analysis of the manufactured coatings	192
Supplementary Figure 3 Full optical transparency study conducted using photon transmission.....	194
Supplementary Figure 4 Complete concentration study of the Ti-PDMS hybrid for the RX300 particles	195
Supplementary Figure 5 Complete study of photon transmission for all the concentrations of the RX300 particles	196

List of Tables

Table 1.1 The relation between contact angle and wettability of surfaces with water.	4
Table 1.2 Ideal material properties for Young contact angle. ³⁵	6
Table 1.3 Fluorinated silanes used in surface modification ordered based on surface tension.....	23
Table 1.4 Alternative to fluorinated silanes used in research with structures and surface tensions.....	25
Table 1.5 Examples of methods used for fabrication of superhydrophobic coatings with key advantages, disadvantages and examples of coatings in literature. The list also indicates in bold the three methods used in this project to fabricate the coatings.....	28
Table 2.1 Description of the Q1 - Q4 environments as indicated in Figure 2.5b.	56
Table 3.1 Calculated metal oxide content and metal/Si atomic ratios of the hybrid-PDMS based on complete reaction.....	70
Table 3.2 Superhydrophobic coating composition. Each coating was fabricated using 0.4 g anatase, 0.1 g OX50 and 0.665 g stearic acid.....	70
Table 3.3 Superhydrophobic coating composition. Each coating was fabricated using 0.4 g anatase, 0.1 g OX50.....	71
Table 3.4 Superhydrophobic coating composition. Each coating was fabricated using 0.1 g OX50 and 0.665 g stearic acid.	72
Table 4.1 Experimental design of sonication effect on the quality of the superhydrophobic coatings.	111

Table 4.2 Experimental design of superhydrophobic coatings for Spray coating method where RX = RX300, MP = mesoporous silica particles, FMP = functionalised mesoporous silica particles, number refers to concentrations and A/B indicates number of spray passes..... 113

Table 4.3 Evaluation of the effect of mesoporous silica on coating properties versus non-porous silica particles through contact angle and transparency... 122

Table 4.4 Experimental design of titanium crosslinked PDMS superhydrophobic coatings for Spin coating with indication of secondary heat treatment or not.. 123

Table 4.5 Experimental design of superhydrophobic coatings for AACVD method where AD = AACVD, 1-3 refers to particle concentrations and A-C indicates temperature of the system during deposition. 130

Table 4.6 Selection of coatings for comparison of the two methods based on highest concentration of particles for each method..... 137

Table 4.7 Summary comparison of the coatings based on particle concentration and durability tests and transparency. 145

Table 4.8 Comparison between manufactured coatings and literature based on particle concentration, transparency and advancing contact angle (θ_a). (*) indicates fluorinated components.^{119,127-129} 147

Abbreviations

²⁹ SI SSNMR	Silicon 29-isotope Solid State Nuclear Magnetic Resonance Spectroscopy
AACVD	Aerosol Assisted Chemical Vapour Deposition
AC	Acetic Acid
AFM	Atomic Force Microscopy
AMNPS	APTES Mesoporous Nanoparticles
APTES	3-Aminopropyl)triethoxysilane
ASNP	Amorphous silica nanoparticles
ATR-FTIR	Attenuated Total Reflectance Fourier-Transform Infrared Spectroscopy
BA	Benzoic Acid
CA	Carboxylic Acid
CTAB	Hexadecyltrimethylammonium bromide or cetrimonium bromide
CTAC	Hexadecyltrimethylammonium chloride or cetrimonium chloride
CVD	Chemical Vapour Deposition
DI	Drop Impact
DLS	Dynamic Light Scattering
DNPS	Dendritic Nanoparticles
EDS/EDX	Energy-dispersive X-ray spectroscopy
ETOH	Ethanol

FDTs or PFTS	Perfluorodecyltrichlorosilane
GLYMOS	(3-Glycidyloxypropyl)trimethoxysilane
IPA	Isopropanol
LS	Light Scattering
MNPS	Mesoporous Nanoparticles
OA	Octanoic Acid
PA	Palmitic Acid
PDMS	Polydimethylsiloxane
PDMS-OH	Hydroxy terminated Polydimethylsiloxane
PFCAs	perfluorinated carboxylic acids
POTS	Polyfluorooctyl trialkoxysilanes
PT	Photon Transmission
Rz	Resazurin
SA	Succinic Anhydride
SEM	Scanning Electron Microscopy
SiO ₂	Silicone Dioxide
TEM	Transition Electron Microscopy
TEOS	Tetraethyl orthosilicate
TiO ₂	Titanium Dioxide
TMODS	Trimethoxy(octadecal)silane
TTIP	Titanium Isopropoxide
UV/Vis	Ultraviolet-visible
XPS	X-ray Photoelectron Spectroscopy

XRD	X-ray Diffraction
Γ	Surface Tension
$\Delta\theta$	Contact Angle Hysteresis
θ_A	Advancing Contact Angle
θ_R	Receding Contact Angle

Chapter 1

General Introduction

This thesis summarizes the significant changes towards production of liquid repelling, fluorine-free, photoactive and near transparent commercially viable coatings and near transparent superhydrophobic fluorine-free self-cleaning thin films. Key literature background follows this preface which works to outline key definitions and publications that set premise throughout this thesis. Advancements to the mentioned research fields have been recorded in Chapters 2-4.

Growing demands for super liquid repelling surfaces such as superhydrophobic and/or superoleophobic materials has been mainly driven by the increasing range of applications in expanding areas, including self-cleaning surfaces,¹ reduction of drag,² anti-icing,^{3,4} self-healing⁵ and various other areas.⁶ As such, developments in polymer properties and structures,^{7,8} particle morphology⁹⁻¹⁴ and functionality¹⁵⁻¹⁷ as well as composite stability¹⁸⁻²¹ have been thoroughly studied to better enhance the fabrication process and to facilitate the distribution of the technologies into further fields of application. The key aspects of environmental stability and sustainability have been central to the new design of smart water retardant materials leading to a focus on durability and the use of low hazard materials to minimize impact from production and use.

Transparent and durable water repelling surfaces have been of growing interest especially within the microfluidics^{22–25} and smart windows fields. Based on examples found in nature such as the lotus leaf²⁶ or cicada wings,²⁷ aspects of both can be noted in many surfaces fabricated in literature where silanes are used to lower surface energy and hierarchical roughness is achieved to decrease the contact between solid and liquid phases. Current difficulties faced by a fluorine-free approach to mimicking nature designs are combining durability and transparency when aiming to achieve coatings within Cassie-Baxter regimes especially through facile and low cost methods and materials.²⁸

1.1 Defining surface wetting behaviour

The basic understanding of the models and mathematical solutions developed to comprehend liquid-solid interfacial behaviour is necessary to appreciate the conditions needed to achieve superhydrophobicity and superoleophobicity. The models were developed with water-solid interactions but are highly applicable to both water and oils as such the chapter discusses and demonstrates the models in terms of water-solid phase behaviour.

The discovery of wetting behaviour denoted by Young and the ideal conditions described,²⁹ lead to further development into rough surfaces and their behaviour primary in the works of Wenzel and Cassie & Baxter where the need for hierarchical structuring was proposed.^{30,31} These models, suggested by them, still have impact on mathematical models currently used to calculate surface contact angles and energies.

When considering what is wetting, how it defines superhydrophobicity, it is important to note that most liquids have surface interactions with a solid based on contact angles and surface energies. These interactions are of equilibrium forces and examples of these can be seen in Figure 1.1 with different droplet spreads or wetting of the surface of a solid. Depending on the types of interaction, variation of the behaviour is displayed.³²⁻³⁸

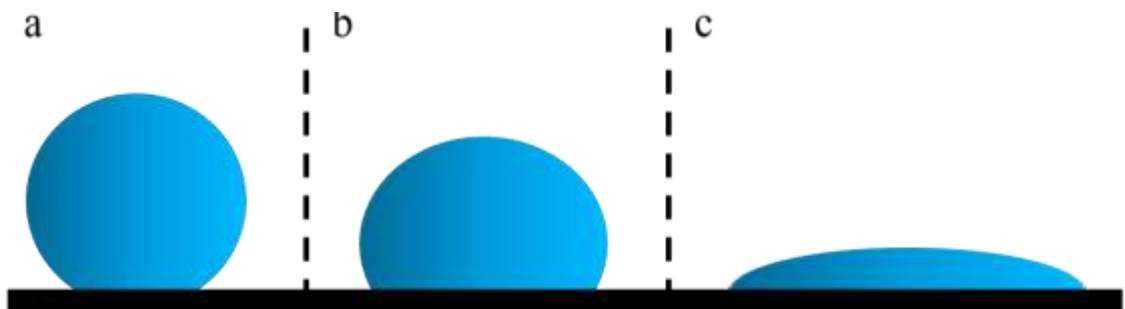


Figure 1.1 Wetting behaviour of water on a solid (a) Low contact angle and low wetting (b) Intermediate (c) High contact angle and high wetting

This is best explained by the example of water as the liquid; if a surface is super water repelling or superhydrophobic then a low contact between the liquid and the solid is preferred to minimise the energy differences between them (Figure 1.1a), whilst if the solid surface attracts water, i.e. is hydrophilic, then the droplet spreads to minimise the energies again (Figure 1.1c) but this time it is preferential to not maintain the droplet shape.^{32,34,36}

In plain, contact angles are a representative measure of the balance of the adhesive and cohesive forces present during the interaction between a liquid droplet and the surface of a solid. ³² Depending on which force is optimal the value of the contact angle between the droplet and the solid changes, as illustrated in Figure 1.1 from when the cohesive forces are preferred resulting in

low spreading to where adhesive forces are dominating as seen by high spreading.

When focusing on a single contact line, dynamic measurements of the angle can be made where the droplet is placed on a surface then retracted. This results in advancing and receding contact angles.^{35,39} The resulting values for advancing contact angle can indicate the type of interaction the liquid has with the surface as shown by Table 1.1 and illustrated in Figure 1.1.

Figure 1.1	Contact angle	Wetting	Type of interaction
a	$\theta \geq 150^\circ$	Low	Superhydrophobic
b	$90^\circ < \theta < 150^\circ$	Medium	Hydrophobic
c	$\theta \leq 90^\circ$	High	Hydrophilic

Table 1.1 The relation between contact angle and wettability of surfaces with water.

The difference between the two measurable angles can be used to determine the wetting effect of the liquid on the solid known as the contact angle hysteresis. For self-cleaning application or for when the surface is designed to have droplet mobility the ideal value for hysteresis is 0° as this means there are no adhesion forces acting on the droplet once it is placed on the surface. However, it is generally accepted to fit the function when the contact angle hysteresis is below 10° .

When thinking about the three phase interactions of a droplet on a surface it is important to first consider the equilibrium in a non-planar spherical mode as is the shape of the droplet placed on the surface of a solid. This is clearly

illustrated in Figure 1.2a where each phase is also indicated by its contact angle.

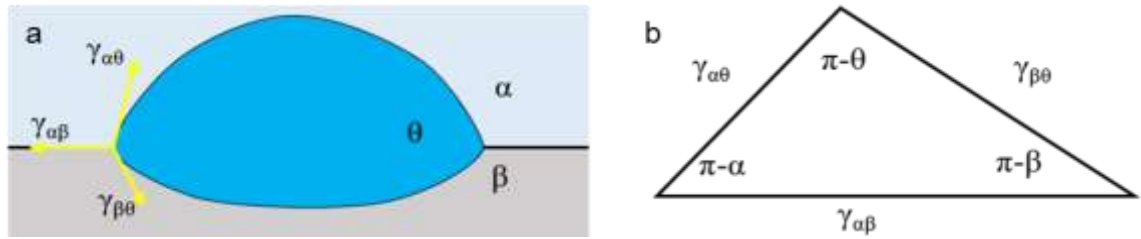


Figure 1.2 Representation of the coexistence of the three phases and their contact angles both in (a) diagram and in (b) Neumann's triangle

$$\gamma_{\alpha\theta} \cos(\theta) + \gamma_{\theta\beta} + \gamma_{\alpha\beta} \cos(\beta) = 0$$

$$\gamma_{\theta\alpha} + \gamma_{\theta\beta} \cos(\theta) + \gamma_{\alpha\beta} \cos(\alpha) = 0$$

$$\gamma_{\alpha\theta} \cos(\theta) + \gamma_{\theta\beta} \cos(\theta) + \gamma_{\alpha\beta} = 0$$

Equation 1.1 Components of the net force in one direction of the phase interfaces: α , β , and θ are the angles shown in Figure 2; γ_{xy} is surface energy between indicated phases.⁴⁰

From the diagram, at equilibrium the net force acting along the boundary line where the phases meet must be equal to zero which leads to the definitions for net force in any direction along each of the interfaces, as shown in Equation 1.1. With that, the interactions can be expressed similarly in a Neumann's triangle which is held by the restriction that the sum of all the angles is equal to 180° or 2π .⁴⁰

To further explain the interactions between solid surfaces and liquid droplets, the three models along with an example of transition state have been briefly

illustrated in Figure 1.3 with the forces of interaction between a liquid (in this case water) and a solid shown for the Young relation. From the models, it is crucial to know that the interaction of water and solid is dictated by an equilibrium of three main forces at the mutual contact point which are respective of the phases of solid, liquid and gas or vapour but have been simplified to a planar geometry.

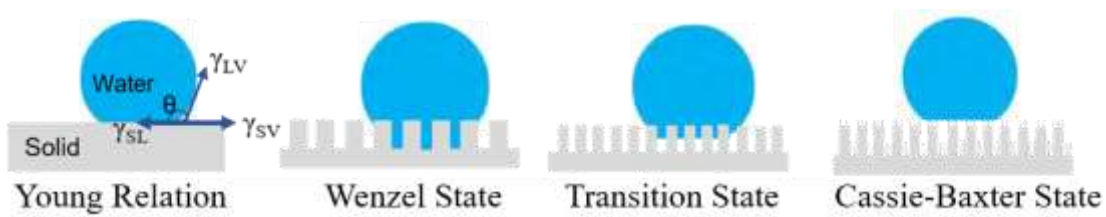


Figure 1.3 Young relation and derived three states of wettability.^{30,31,41}

1.1.2 Young State

In 1805, Young described a model of ideal interactions between a liquid and a solid, as shown by the Young relation in Figure 1.3a.²⁹ Both the liquid and the solid follow a strict list of requirements to fit into the ideal state as described in Table 1.2.³⁵ The model however is limited to perfectly smooth and homogenous solid surfaces.

Ideal solid	Ideal liquid
Clean and smooth	Homogenous and pure
Homogenous	Has a low viscosity
Unreactive with liquid used	Does not evaporate
No surface adsorbed gases or vapours	

Table 1.2 Ideal material properties for Young contact angle.³⁵

When considering the β phase from Figure 1.2 as a rigid, smooth and most importantly flat solid surface the angle at that point is equal to π which allows for the simplification of the net force equation into the Young equation, shown in Equation 1.2:

$$\gamma_{SV} = \gamma_{SL} + \gamma_{LV} \cos(\theta)$$

Equation 1.2 Young's equation. The relation of the surface tensions between the three phases.²⁹

Form the equation, the relation between surface tensions of the three phases is clearly shown and allows for the prediction of a contact angle of a droplet on a solid surface if the surface energies are known. The equation can be also applied to a scenario where the gas phase or α in Figure 1.2 is an immiscible liquid to the droplet. The ability to predict a value for θ , also known as the chemical or even the Young's angle,⁴² allows for a theoretical approach to evaluate experimental methods when designing a surface. This angle however tends to be limited by the lack of roughness that would allow the transition from hydrophobic to superhydrophobic or the jump above 120° .⁴²

In the case of Young's model, the assumptions made are experimentally impractical for many of the cases listed in Table 1.2. When considering Young's surface, it is a perfectly smooth and indefinitely rigid solid. Even if a surface of a solid could be designed at sub-nano smoothness the solid will still show a degree of flexibility hence are finitely rigid. This problem was looked at by Tadmor, where it was noted that the triple phase line energy is a function of any

local surface defects.⁴³ He proposed that the contact angle will reach an equilibrium point between the advancing and receding angles which he called the equilibrium contact angle and proposed how to calculate this, as shown in Equation 1.3 with the r terms fully explained by Tadmor,⁴³ but these are relating to surface roughness.

$$\theta_E = \arccos \left(\frac{r_A \cos(\theta_A) + r_R \cos(\theta_R)}{r_A + r_R} \right)$$

Equation 1.3 The Tadmor equation for calculating the equilibrium contact angle.⁴³

Considering still the ideal wetting in Young's model, a droplet will still show a spectrum of spreading on the surface. In 1869, it was noted by Dupré that the behaviour of a droplet is dictated by the spreading coefficient which was developed further into the spreading and drying parameters, as explained by Quéré.^{42,44} The two parameters are inverse of each other, as shown in Equation 1.4.

$$S = \gamma_{SA} - (\gamma_{SL} + \gamma_{LA})$$

$$D = \gamma_{SL} - \gamma_{SA} - \gamma_{LA}$$

Equation 1.4 The spreading coefficient (S) by Dupré and Drying parameter (D) by Quéré.^{42,44}

The work by Dupré dictates that neither the surface energy between solid-liquid phase and solid-gas phase can be larger than the total of two remaining surface energies.^{44,45} This in turn results in an ability to predict whether the droplet will

completely wet the surface, which is the case when $\gamma_{SA} > (\gamma_{SL} + \gamma_{LA})$, or be non-wetting, when $\gamma_{SL} > (\gamma_{SA} + \gamma_{LA})$. This means that the S coefficient dictates that complete wetting will occur when $S > 0$ but only partial wetting will occur when $S < 0$.^{42,44,45} This was then related to the Young's equation forming the Young-Dupré equation as show by Equation 1.5 where when combined with the wetting described by S coefficient has only physical solutions for when $S < 0$.^{44,45}

$$S = \gamma_{LA}(\cos(\theta) - 1)$$

Equation 1.5 The Young-Dupré equation combining the spreading coefficient and Young's equation.^{42,44,45}

1.1.3 Surface morphology directed states of wetting: Wenzel, Cassie-Baxter and Transition states

The Wenzel state (1936) shown in Figure 1.3b describes a water droplet interacting with a rough surface where the water displaces the air trapped by the roughness.³⁰ This relation is seen in materials where the pinning prevents the droplet rolling-off of the surface. Wenzel has defined that the roughness affects a homogenous surface by a factor r and what can be measured is the apparent contact angle which corresponds to the contact angle at the equilibrium, as shown in Equation 1.6.³⁰

$$\cos \theta^* = r \cos \theta$$

Equation 1.6 The Wenzel equation relating the roughness to contact angle.

Equation 1.6 builds on the understanding of the Young model with the Young's angle (θ) but shows that roughness plays a factor in the apparent contact angle (θ^*). By introducing the roughness ratio (r), Wenzel accounts for the apparent roughness as a ratio of the area to the solid surface to the apparent area which affects the wettability.³⁰

However, despite showing that roughness results in a different contact angle to the intrinsic angle presented by the Young model, it fails to account for the existence of hysteresis. From Figure 1.3, it is clear that this model only holds true when the droplet pins the surface (the liquid fills the roughness of the surface completely) and therefore there is no receding contact angle.

With increasing understanding of the relation between roughened surfaces and their wettability, in 1944 Cassie & Baxter developed a model that shows that when the roughness is not uniform or in a high enough degree, air is trapped by the surface features as depicted in Figure 1.3d.³¹ This prevents pinning often seen in Wenzel state allowing for the droplet to be removed from the rough surface with ease.³⁰ As the material is air-saturated it needs minimal energy to move the droplet due to low hysteresis.

The non-uniform surface shown in Figure 1.3d has been designed to abide by Cassie's laws shown briefly in Equation 1.7. The law is then further transcribed into the Cassie-Baxter equation which combines Cassie's laws with the Wenzel model.

$$\cos(\theta_E) = f_1 \cos(\theta_1) + f_2 \cos(\theta_2)$$

$$\cos(\theta^*) = r_f f \cos(\theta_Y) + f - 1$$

Equation 1.7 Cassie's law and Cassie-Baxter equation for calculating apparent contact angle of heterogenous rough surfaces.³¹

Cassie's law describes the relationship of the components of the fraction area (f) and effective contact angle (θ_E) on a composite surface. The law helps to understand the key role trapped air has on the value of the observed contact angle. This is because any liquid has a contact angle of 180° with air resulting in the formation of spherical droplets.³¹ This results in the simplification of the law through cosine rules where $\cos(180) = -1$ simplifying the second term of the law which means θ_C is dependent on the solid phase component and with small f_1 and large θ_1 , surfaces with large contact angles are possible to design.^{31,42,46,47}

The Cassie-Baxter equation can be represented in various ways depending on the desired output which is described elsewhere.^{31,42,48} But it is key to point out that when the fraction of the solid surface area that is wet $f = 1$ and the ratio of the roughness of the wet surface $r_f = r$, the equation becomes the Wenzel equation, as seen in Equation 1.6, as the surface became homogenously wet and the heterogenous nature of the composite did not affect the apparent contact angle.

This has led to the simplification of the equation by Quéré *et al.*,⁴⁹ particularly it is useful for when the resulting surface is not contain repeating regular structures. This is because for such surfaces – as the one focused within this

thesis in later chapters – it is difficult to obtain a comprehensive understanding of the relationship between water phase and solid phase interact as the specific positions for these interactions cannot be accurately identified or characterised.⁵⁰ The equation described in **Equation 1.8** considers the different phase interactions (solid-liquid and liquid-vapour) as planar, hence removing the roughness factor and allows for the interfaces to be considered as fractional areas.

$$\cos \theta_{CB} = \phi_s \cos \theta_e + \phi_s - 1$$

Equation 1.8 Simplified version of the Cassie-Baxter model proposed by Quéré *et al.*⁴⁹

This transition between Cassie & Baxter and Wenzel state, occurs when the roughness trapping the air pockets is disrupted by either impact force or pressure which results in the transition, as seen in Figure 1.3c. There have been two main transitions defined in Equation 1.9, which describe the mushroom state or partial penetration, shown in Figure 1.3c. The penetration front spreads until the edges of the droplet, resulting in the full Wenzel state as a means of reducing energy to reach a new equilibrium.^{46,51}

$$\cos(\theta_c) = \frac{\varphi - 1}{r - \varphi}$$

Equation 1.9 Condition required for the transition between Cassie & Baxter and Wenzel state: θ_c – critical contact angle; φ – interphase fraction of the drop contact with surface; r – roughness of the solid (in case of flat surfaces $r = 1$).

1.1.4 Sliding Angle and Contact angle hysteresis

Contact angle typically refers to the static behaviour between a liquid deposited on a solid. However, there is a fundamental lack of accountability for droplet mobility, as in how readily the droplet rolls/ slides off the surface as shown in Figure 1.4.

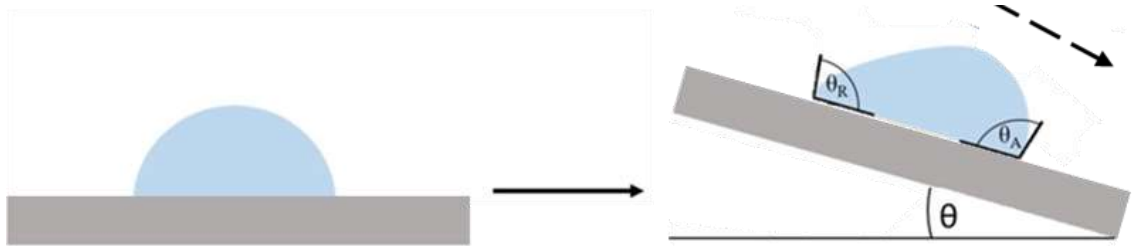


Figure 1.4 Schematic of sliding angle by tilting the solid until droplet just starts rolling. Sliding angle is represented by θ . The arrow represents the rolling direction of the droplet.

Sliding angle (SA), is a dynamic characterization method used to assess the mobility of liquid droplets.⁵² Importantly, it is not an angle between a liquid and a solid, but the titled angle of the solid surface when the droplet just starts rolling or sliding. In some literature, sliding angle is also referred to as the rolling angle (RA) and tilting angle (TA).^{53,54}

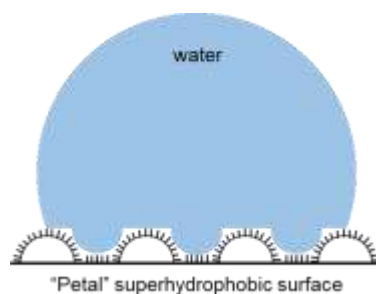


Figure 1.5 Schematic representation of the “Petal effect” mechanism of high adhesion superhydrophobic surface.

This measure allows for the separation of the superhydrophobic material (for example) into two subcategories: 1. Low adhesion and 2. High adhesion. Low adhesion surface is considered to show contact angle greater than 150° and hysteresis below 10° . These surfaces tend to exhibit good self-cleaning properties as droplets placed on such surfaces bead-up, roll off and pick up any dirt particles as they do so.⁵⁵ High adhesion surfaces see the liquid droplet pinned to its surface. This effect is often referred to as the “Petal effect” and occurs within a surface exhibiting both Wenzel and Cassie-Baxter state, as shown in Figure 1.5, where the water droplet can be upheld by the nanostructures however the separation of the microscale roughness promotes the filling of the gaps hence resulting in pinning.^{55,56}

Roughened surfaces are known to alter the contact angles between water droplets and surfaces.^{30,31,34,37,42} This is a primary requirement that is not covered by Young’s relation (ideally flat surfaces only). This concept of roughness or lack of perfect homogeneity at the surface of a solid gives rise to a phenomena called contact angle hysteresis which is defined by Equation 1.10.^{41,42}

$$\Delta\theta = \theta_A - \theta_R$$

Equation 1.10 Contact angle hysteresis where $\Delta\theta$ is the hysteresis, θ_A is the advancing and θ_R is the receding contact angles.

Hysteresis phenomena measured by dynamic contact angles is universally expressed by the difference between the advancing and receding contact angles and is seen on real rough surfaces where the liquid droplet does not

adhere or pin to the solid.^{42,46,57} The physical basis of contact angle hysteresis ($\Delta\theta$) is still unclear,^{42,57} however it has been studied to show that the phenomenon occurs due to non-ideal properties of real surfaces resulting in several metastable states or thermodynamically stable contact angles. Pinning of a droplet occurs because the deposition on the surface is slow enough for the contact line to form between the solid and liquid phase resulting in partial wetting where the Young-Dupré equation holds true.⁵⁸

There are two methods for measuring the contact angle hysteresis: 1. The tilting-plate goniometry and 2. Captive-drop goniometry.⁵⁹ The first method captures the advancing and receding contact angle on both sides of the droplet when the surface is tilted to the sliding angle (between 0 and 90°). The second method records the advancing angle as volume is added into the droplet to the maximum before the increase of the contact line of solid-air-liquid phases while the receding angle is recorded while the volume is removed.⁵⁹ The data from both methods is then processed according to Equation 1.10 resulting in the apparent contact angle hysteresis value.

1.2 Liquid repellence in nature

There are several examples of liquid repelling surfaces in nature both in plants and animals. Such adaptations have aided many a species to survive in its habitat be it through removing waste from its surface, preventing soaking of wings or facilitate prey capture. Examples such as the Lotus leaf, Cicada insects or pigeons show great inspiration towards water repellence whilst Cicadellidae demonstrate oil repelling properties. Beyond “dry” coatings (use

trapped air to facilitate repelling of liquids), there are examples of complete wetted surfaces which utilise lubricants instead of air to promote droplet slip such as the Carnivorous *Nepenthes* pitcher plants.

1. *Lotus Leaf*

Frequently, the lotus leaf is used as an example of superhydrophobic surface from nature.^{26,60,61} The micro-nano hierarchical structures along with waxy layer render the surface superhydrophobic and self-cleaning with the droplet showing low hysteresis meaning it easily rolls-off the surface as illustrated in Figure 1.6.²⁶

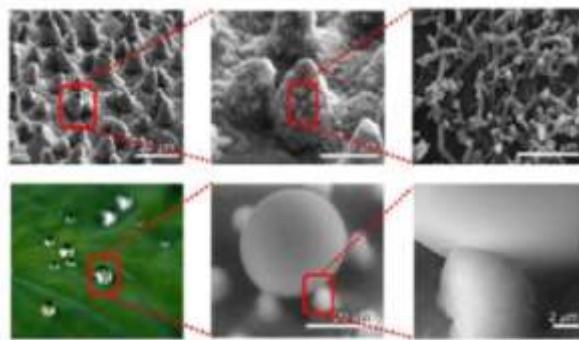


Figure 1.6 Morphological analysis of the lotus leaf and microscopic analysis of water droplet on the surface of the leaf.²⁶

From the SEM analysis of the surface, micro pillars can be observed with epicuticular wax nanostructures increasing the roughness of the surface. This allows for enhanced trapping of air within the solid, which reduces the solid surface contact fraction between the solid and liquid phase.²⁶ Furthermore, the epicuticular wax reduces the surface energy of the surface due to the presence of non-polar hydrocarbon chains which limits the adhesion of water droplet to the surface.²⁶

Lotus leaf structures can be seen in Figure 1.6 to show flexibility under the droplet. This property allows for a surface to be better suited for drop impact as the non-rigid nature of such structures preserves the air trapped within the gaps whilst absorbing (through flexing) the force of an impact further protecting the structures from damage.²⁶ This property has proven to be of great interest to synthetic applications and has resulted in the application of polymers and viscous oils in achieving liquid repellence.

Beyond the lotus leaf, several species of animals and insects also display hydrophobic properties,⁶² with examples in birds such as pigeons and insects from the cicada family.^{61,63}

2. Cicada insect family

The superhydrophobic phenomena in the cicada is achieved due to nanopillar structures on the wings of the insects (Figure 1.7) like that of the lotus leaf. The pillars have been extensively studied as varieties in height, spacing and diameter of these structures have been shown to affect the state of water repellence as either Wenzel or Cassie-Baxter.⁶¹ Additionally, the nanopillars have been shown to have bactericide properties on Gram-negative bacteria whilst Gram-positive remained unaffected. This showed promise in applying superhydrophobic surfaces to anti-bacterial systems without the need for bactericides.⁶¹

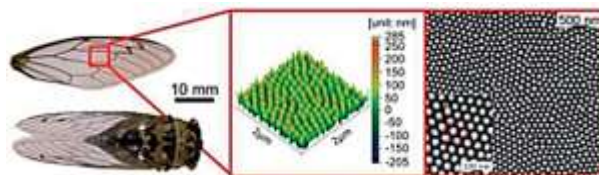


Figure 1.7 Cicada insect wing structure analysis.²⁷

Additional factor to consider from the cicada wings is transparency. Due to the nanoscale of the structures attributed to superhydrophobic behaviour, the light scattered is minimal which explains the high optical transparency and low scattering of these structures.⁶¹ Applying this to artificial coatings would give rise to optically transparent coatings whereas as indicated in prior chapters, roughness benefits superhydrophobicity but the higher the roughness the lower the transparency due to increases in light scattering. However, from the cicada wing example, if the roughness remains in the nanoscale below that of the wavelength of visible light, scattering is minimised, and transparency is achieved.

3. Pigeon Wings

In contrast to the insect wings, birds superhydrophobicity is primarily resulting from high critical pressures and number of barriers which prevent water penetration into the feather structures and retain the Cassie-Baxter state.⁶³ Unlike the insect wings or the lotus leaf, bird feathers exhibit pseudo hierarchical structures where the roughness is of varied diameters whilst the height or scale remain the same.⁶³ The difference between true and pseudo hierarchical structures is illustrated in Figure 1.8.

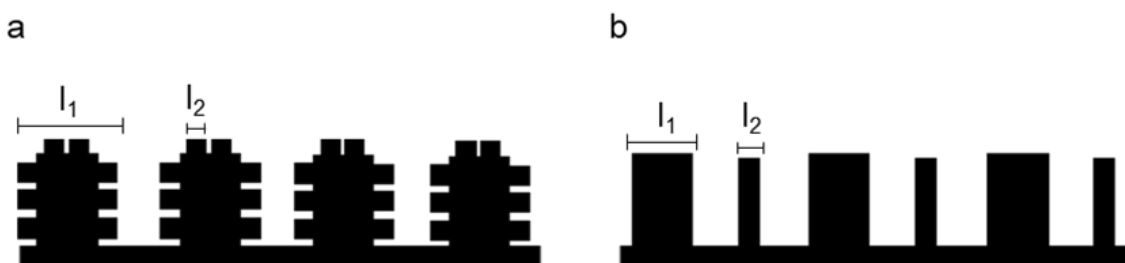


Figure 1.8 Illustration of (a) True hierarchical and (b) pseudo hierarchical structures. (l_1 and l_2 represent the hierarchical difference in length)

Pseudo hierarchical surface is achieved through the barbs and barbules of the feather where the air is trapped by the barbules to facilitate water repellence. Despite the hydrophilic nature of the material (keratin) the feather is made of, the high density of the barbules causes increase in capillary pressure causing stabilization of the Cassie-Baxter state hence the water droplet is easily repelled from the surface of the feather.⁶³

Additionally, it is worth noting that the pseudo hierarchical structure of the feather increases the energetic barrier between the surface and the liquid to 65.7 nJ/mm^2 , which is much higher compared to that of true hierarchical structures of artificial fluorinated superhydrophobic surfaces.⁶³ Furthermore, the feather can withstand much higher pressures than artificial coatings, of about two orders of magnitude, which is equivalent to dynamic pressure of a falling rain drop.

Beyond superhydrophobicity, nature exhibits other wetting behaviour such as superoleophobicity and slippery liquid infused porous surfaces (SLIPS).^{61,64} These behaviours have strong applications within industry from water-oil separation for oil spill clean-up to anti-biofouling.

4. Collembola

There has been extensive research into the collembola or springtails to understand their adaptation to survive in soil environments. Numerous studies show the structure of more than 40 species of this insect with porous honeycomb-like structures.⁶⁴ Figure 1.9 shows an example of one the species exhibiting superoleophobic behaviour.

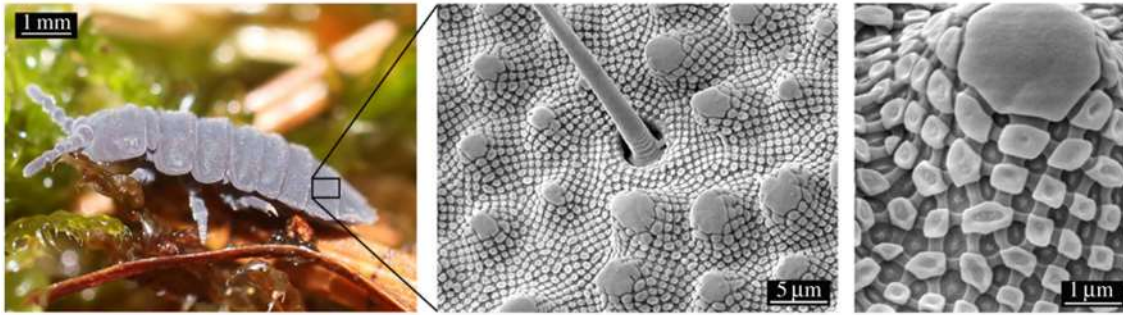


Figure 1.9 SEM images of *T. bielensis*. showing papillose structures covered by a rhombic comb-like nano tubercles mesh.⁶⁴

These structures along with the chemical composition of the outer layer consisting of hydrocarbon acids and esters, steroids and terpenes shows great promise to the manufacture of fluorine-free superoleophobic coatings.^{61,64}

Many examples of superhydrophobic surfaces in nature,^{26,61,62} influence the design of artificial coatings. Achievements as self-cleaning and true hierarchical structure from lotus leaf with a surface energy reducing layer has strongly influenced the choices made in the development of fluorinated coatings whilst the nanoscale roughness of the cicada insects has demonstrated that transparency can be achieved if roughness is retained below the wavelength of light to minimise scattering. Birds feather have shown that variation of structures at the same scale can be utilised to achieve water repellence with pseudo hierarchical topologies when utilised to enhance capillary pressures through high density of the material which further benefits drop impact resistance.

1.3 Reducing surface energy and the hazards of fluorinated silanes

With manufacture of liquid repelling surfaces being of interest for decades, many have seen successful incorporations into industry. The vast majority of research focuses on the use of silanes to reduce the surface energy of the coatings. Silanes are a group of inorganic compounds primarily consisting of silicon and hydrogen. The benefits of such materials includes the ease of functionalisation of surfaces due to readily reactive alcohol groups on the compound whilst the uncreative functional group can be tailored to desired surface reducing properties. Typical process of silanization (bonding the silane to the surface) of the coating surface has been illustrated in Figure 1.10.

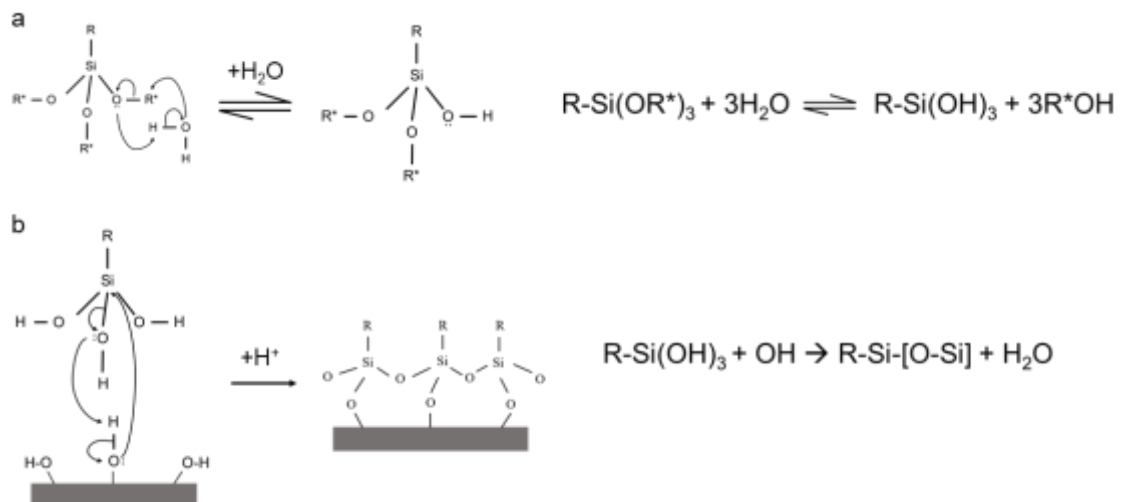


Figure 1.10 Silanization process forming a layer of functional groups between the liquid and the solid where the r-group represents any functionality of the selected silane.^{65,66}

It can be noted that due to a blanket like behaviour of such materials as illustrated by Figure 1.10, the functional groups (R) orientate away from the solid surface creating a low surface energy layer separating the solid and the liquid.⁶⁶

Current progress for the design of liquid repellent materials has been focused on the use of highly fluorinated compounds such as Polyfluorooctyl trialkoxysilanes (POTS). Their abundant use in design is highly attributed to the extremely low surface energies displayed by such material which is otherwise not achievable.

Introduction of the fluorine groups onto the surface reduces the adhesion potential of a liquid to the surface. The R-group shown in Figure 1.10 is often a long alkyl chain where the hydrogens have been replaced by fluorine with the most used being perfluorodecyltrichlorosilane (FDTS or PFTS). This substitution of the hydrogens with the fluorine alters the behaviour of the compound, which was extensively studied by Dalvi and Rossky,⁶⁷ it was discovered that despite the higher polarity of the C-F bond over the C-H bond, the strong tendency of water to minimize changes to the hydrogen network within the droplet, it is essentially obstinate to the electrostatic nature of these fluorinated compounds. This means that the free energy of hydration of resulting surfaces is influenced more by the Lennard-Jones interactions (larger molecular cross-section area) and less by the electrostatic forces.

This implies that the assembly of fluorinated silanes, as depicted in Figure 1.10, is less dense than that of the C-H bonded analogue. Despite lower polarity of these groups, there is still a greater number of molecules which increases the

van der Waal's potential of the surface interactions with the water droplet which results in lower contact angles achieved by the fluorine-free silanized surfaces. However, when considering the capabilities of the fluorinated compounds to repel oils the electrostatic interactions play a key role as these work to further limit the interactions the surface is able to make with the liquid, which is not limited by the use of hydrogenated silanes. For these surfaces, silanes with polar groups such as the amino terminated silanes can be adopted which suggests a reason why the fluorinated approach is favoured in the design of liquid repelling surfaces- one silane can be used to tackle a number of interactions over the need to use different silanes to achieve the same outcome. The popularity of POTS can be clearly seen in current research with surface design still highly relying on fluorine groups to fabricate liquid repelling surfaces. Works by Pan et al.⁶⁸, Pang et al.⁶⁹ and Liu et al.⁷⁰ clearly demonstrate the effectiveness of fluorinated silanes but do not consider their environmental and health hazards. Table 1.3 illustrates commonly used fluorinated silanes and their surface tension.

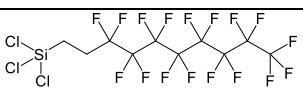
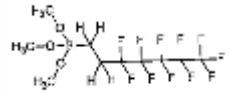
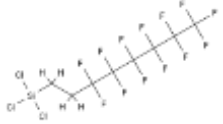
Silane	Structure	Surface tension (mN/m)
Perfluorodecyl-trichloro		17.3
Nonafluorohexyl-trimethoxy		17.4
Trichloro(1h,1h,2h,2h-perfluorooctyl)		17.8

Table 1.3 Fluorinated silanes used in surface modification ordered based on surface tension.

In recent years, there have been many studies conducted on the environmental and health impacts of fluorinated compounds including silanes, which has sparked the debate on the reduction in the use of such reactants beyond the associated dangers of their synthesis.^{71,72} Work by Nørgaard et al.⁷² especially focuses on the toxicology of the perfluorinated silanes on the pulmonary systems. Their findings confirmed that combining fluorinated silanes with organic solvents has detrimental effects on the airways through initial irritation but with further damage done by decreased tidal volume which did not return to baseline after recovery period. This indicates the hazard of combining the silanes with organic solvents as decreased tidal volume (total lung air capacity) may lead to pulmonary edema and further tissue damage.⁷² They noted that water based spray coatings did not have this effect.⁷²

Another report by Blum and Soehl has summarised the health impacts of using highly fluorinated compounds such as silanes.⁷³ The report supports the research conducted by Nørgaard and demonstrates the extent of toxicity and environmental impact of fluorinated compounds.^{72,73} The Green Science Policy Institute which presented the report, focuses highly on the environmental hazards of such compounds with many publications referring to toxic effects on both humans and animals.⁷⁴

Further hazards involved in the use of highly fluorinated silanes is the degradation of such materials into proposed perfluorinated carboxylic acids (PFCAs) which carry a known bioaccumulation resulting in build-up of toxic levels.⁷⁵⁻⁷⁷ Amongst the perfluorinated compounds, long-chain perfluorinated chemicals are of growing concern with examples such as perfluorooctanic acid

(PFOA), an eight-carbon carboxylic acid, which has been shown to have toxicity to humans and environmental persistent properties leading worlds health and environmental agencies to target such materials through limiting use and manufacture.⁷⁶⁻⁷⁸

Following the concerns of environmental and health impacts surface treatments have, there have been several developments in achieving liquid repellence without the use of fluorinated silanes. Some examples of alternative materials can be seen in Table 1.4 along with their structures and surface tension.

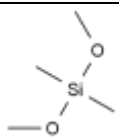
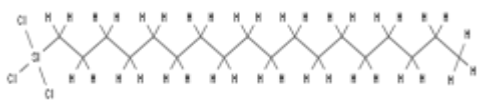
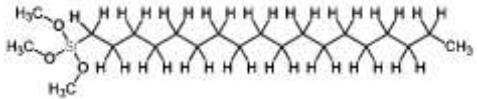
Silane functionality name	Structure	Surface tension (mN/m)
Dimethyldimethoxy		16.9
Trichloro(octadecyl)		29.6
Trimethoxy(octadecyl)		27.6

Table 1.4 Alternative to fluorinated silanes used in research with structures and surface tensions.

Good evaluation of how effective a silane will be in terms of surface modification, other than the potential interactions and their strengths which can be calculated based on the structures, is surface tension/energy of the compound. Due to silanes being liquids, it is more typical to refer to surface

tension rather than surface energy despite both describing the same dimensional quantity. Comparison between various silanes of similar functional group (-R) length can be seen in Table 1.3 which highlight functionality and surface tension.

As shown previously in the Young's equation (Equation 1.2) the surface tension is directly related to contact angle at the point of equilibrium between the three phases. This can be also represented by Equation 1.11:

$$\gamma_{LS} - \gamma_{SA} = -\gamma_{LA} \cos \theta$$

Equation 1.11 The relationship between surface tension and contact angle at equilibrium.

As the surface tension between the liquid-solid and solid-air are difficult to measure directly, the difference between the two ($\gamma_{LS} - \gamma_{SA}$) can be calculated based on liquid-air surface tension and the contact angle at equilibrium.

The general difficulty with using non-fluorinated silanes to reduce surface energy of the solid surface is due to previously discussed properties including higher surface energy and loss of electrostatic forces to repel liquids, especially oils. When comparing alternative silanes of similar chain length, the surface tensions increase between 5 to 10 mN/m. This reduction is a leading factor in the delay to applying such alternatives to surface modification however successful attempts have been made to develop coatings with them.

1.4 Surface fabrication methods

Over the decades of development of liquid repelling surfaces, there has been several techniques developed and optimized for this purpose,^{6,79} with a selection briefly outlined in Table 1.5.

The primary focus of this project is the design of superhydrophobic surfaces through nanocomposite approach, hence a key focus on methods in this section is on deposition methods.

Aerosol-assisted chemical vapor deposition (AACVD) (Figure 1.11) is a scalable technology with low cost and simple operation, which can be operated at an ambient pressure.⁸⁰⁻⁸³ Building upon chemical vapour deposition (CVD) it allows for the preparation of precursors to be deposited as a ready mix.^{83,84}

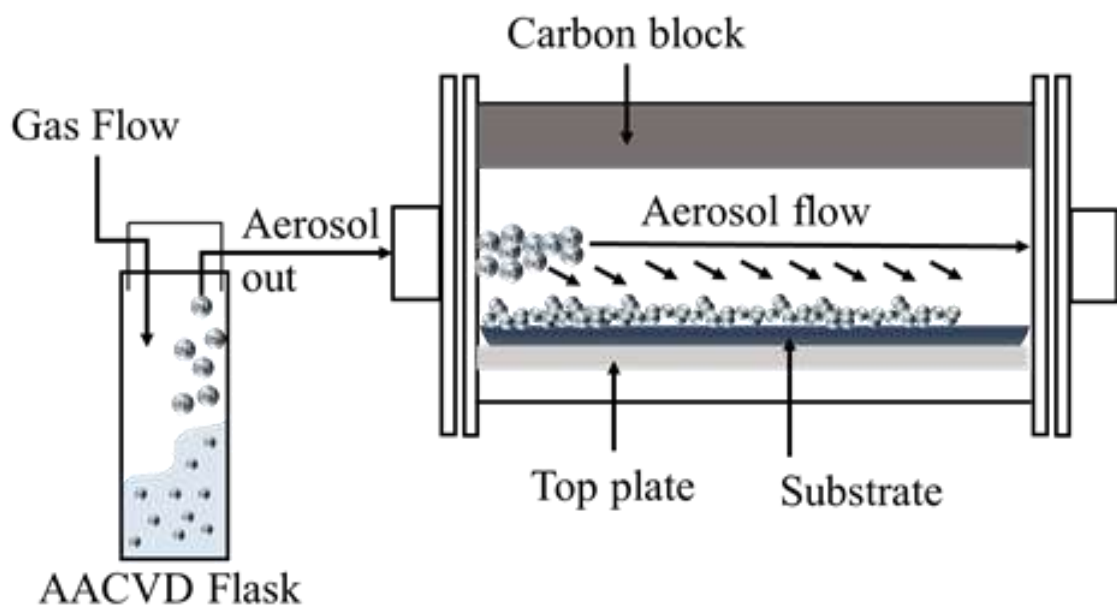


Figure 1.11 Schematic illustrations of our AACVD coating procedure using a nanocomposite.

Method	Advantages	Disadvantages	Ref
<i>Aerosol-assisted chemical vapor deposition (AACVD)</i>	Deposits ready nanocomposite with adhesive. Can be operated at an ambient pressure Thickness control by flow rate and deposition time	Gas flow and heating required Scalability limited to container size Uniformity directed by dispersion and flow rate	80–86
<i>Dip coating</i>	Thickness control with dipping rate Highly adaptable to substrate and composites Highly scalable	Limited control over agglomeration No control of sub-micron features	87–89
<i>Spin coating</i>	Thickness are highly controllable with spin rate Results in highly transparent coatings Uniform coverage of the substrate	Relies on centrifugal forces Limited scalability No control of sub-micron features	6,90–94
<i>Spray coating</i>	Cost effective scalability Fast technique over large areas Can be done under room temperature and ambient pressure	Limited control over agglomeration Limited to no control of sub-micron features	2,95–97

Table 1.5 Examples of methods used for fabrication of superhydrophobic coatings with key advantages, disadvantages and examples of coatings in literature. The list also indicates in bold the three methods used in this project to fabricate the coatings.

Further to this, there has been developments into utilising this technique with nanocomposites, hence eliminating the requirement for fully dissolved or volatile components as is required in CVD, where particles can be suspended and deposited onto substrates with an adhesive component.

Dip Coating is a relatively straightforward approach to surface modification. It relies on submerging the substrate in the coating media which is then deposited onto the substrate when the sample is removed as indicated in Figure 1.12.⁹⁸ The control of coating thickness and homogeneity is therefore highly dependent on coating media composition and substrate withdrawal rate.⁹⁸

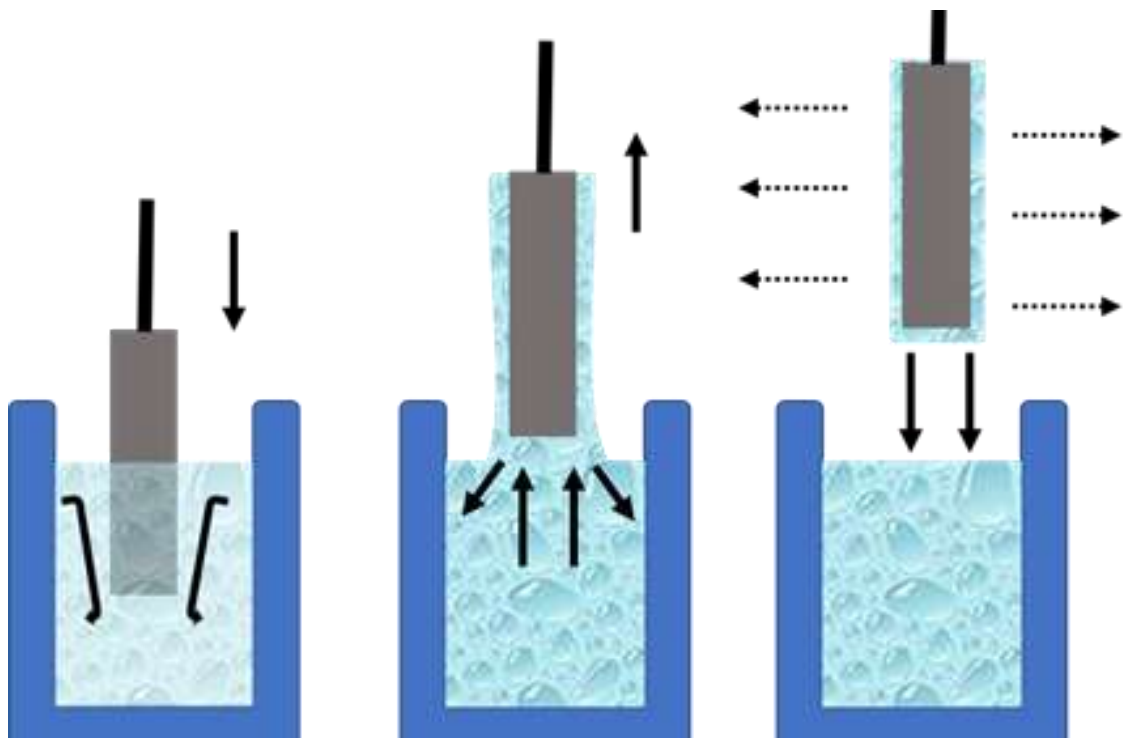


Figure 1.12 Schematic of dip coating process showing immersion (left); withdrawal (middle) and drying (right).⁹⁸

There have been several superhydrophobic coatings developed this way through either the precursor route (roughness is created upon curing treatment)⁸⁷ or the nanocomposite approach (readymade particles mixed with

polymer).⁸⁹ The high scalability and coating control often permit the design of highly transparent coatings whilst the use of sol-gel approach permits for thermally stable coatings.

Spin coating has been widely used to modify surfaces by deposition of thin films of low surface energy to achieve superhydrophobicity.^{91–94} The method relies on centrifugal forces to spread the liquid forming a thin film around textured surfaces or in the case of nanocomposites to form a uniform coverage of the substrate as depicted in Figure 1.13. This method often results in highly transparent coatings as agglomeration and clumping of the particles, as well as coating thickness, is highly controllable depending on spin rate.

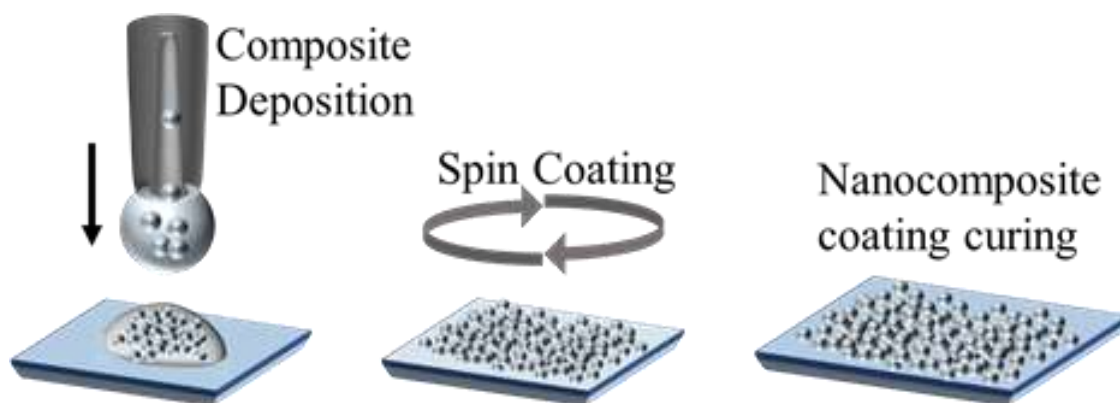


Figure 1.13 Schematic illustrations of Spin coating procedure.

Spray coating (Figure 1.14) for liquid repelling surfaces was first based on the use of sol-gels such as shown by Mahadik et al.⁹⁷ which focused on hydrolysed hydrophobic silica source (silanes) for transparent superhydrophobic coating. Sol-gel process requires heat to produce particles, which was achieved here through spray coating onto hot substrate. Furthermore, due to this method being a largely scalable manufacturing technique for surface design,

Neelakantan et al.⁹⁶ used it in the development of an omniphobic Zinc Oxide: PDMS nanocomposite coating.

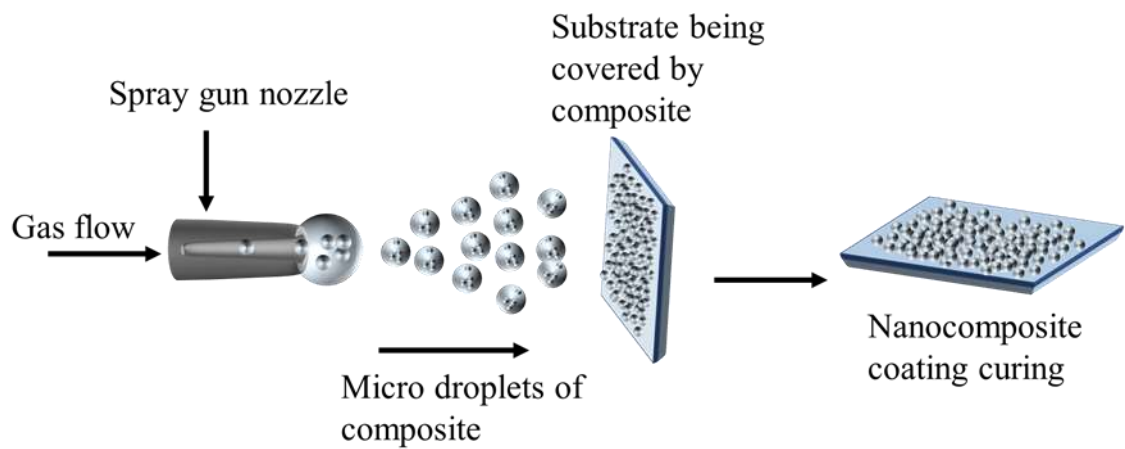


Figure 1.14 Schematic illustrations of Spray coating procedure.

This approach utilized *ex situ* synthesised particles in combination with the polymer resulting in a heterogeneously rough surface. The contact angle and hysteresis were tailored depending on the type of silane utilised in the composite synthesis.⁹⁶ This method is a fast and useful technique that produces high contact angles whilst controlling flow rate and distance can be used to produce good transparency within the coating.

There have been further developments in coating fabrications with methods such as: chemical vapor deposition (CVD),^{99–103} etching,^{3,104–112} or templating showing great results with a various precursors or morphology control.^{113–116} Each however has its limitations, predominantly scalability of the methods can be an issue. With CVD there is the additional restriction of relying on dissolved or volatile monomers, etching is limited by substances that can be utilised whilst templating often requires harsh post fabrication treatments and a master template. In contrast, a number of works have demonstrated that AACVD, spin

coating and spray coating can be utilized with *ex situ* prepared composites for direct deposition on substrates.^{8,96,117,118}

1.6 Design and application of superhydrophobic coatings

To fabricate superhydrophobic materials, fluorinated silanes or other fluorine based materials have been used and are widely reported in literature.^{68,70,119,120}

The two previously conversed silanization approaches include the use of fluorinated and non-fluorinated silanes, which will be discussed in this section.

Fluorinated superhydrophobic coatings (Figure 1.15) have been shown to achieve high water contact angles often exceeding 160° and exhibit high droplet mobility with low sliding angles and hysteresis.^{69,85,121–124} The low surface tensions achieved with the use of fluorinated silanes increases the applicability of the coatings in the real world as facile and scalable methods can be used to tailor the design of the materials towards specific functions such as producing highly transparent coatings using AACVD,⁸⁶ or highly durable surfaces using spray coating.¹²⁵ When focusing on nanocomposite fabrication, the use of fluorine groups permits to: 1. Reduce particle concentration- this favors transparency optimization;⁸⁵ 2. Addition of extra adhesive layers that are typically hydrophilic- this promotes durability of the coating; 3. Increase particle concentration or size- this works beneficially to improve impact resistance.⁶⁹ Fluorinated groups remain favored for liquid repelling surfaces due to potential electrostatic interactions which reduce surface-liquid phase contact.⁶⁷ In recent years there have been many studies conducted on the environmental and

health impacts of fluorinated compounds including silanes,^{71–78} which has pioneered focus onto non-fluorinated counterparts.^{1,5,126–128}

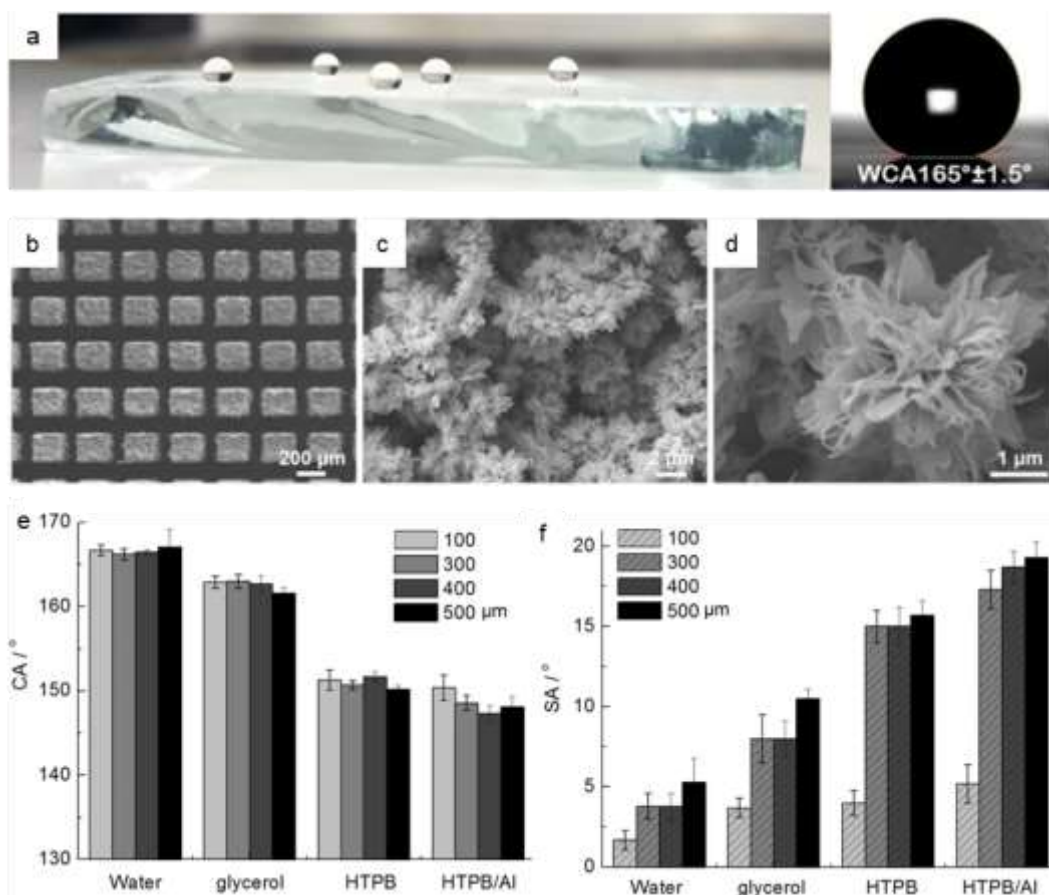


Figure 1.15 (a) Image of droplets on a superhydrophobic coating with contact angle measured.⁸⁵ (b-c) SEM images of Cu/CuO@PFDTCS micropillar arrays.¹²² (e-f) contact angle and sliding angle of different liquids on Cu/CuO@PFDTCS micropillar arrays.¹²²

Several successful attempts at replacing fluorinated silanes have been reported in the literature, as exemplified in Figure 1.17.^{89,118,126,129–131} Progression into alternatives focused on utilising hydrocarbon silanes where the halogen group is replaced with less hazardous functionalities such as long chain hydrocarbons,

alcohols, amines and acids have all shown results in this.^{132–135} Coatings, however, are limited by the surface tension of the silanes resulting in fabrication methods being limited by application target. It can be often found one or two complimentary applications of coatings developed such as self-cleaning and transparency or self-cleaning and durability, but it is much harder to achieve a combination of functionalities without the use of fluorine groups. However, it is key to show that these coatings still achieve contact angles in the region of 160° with low hysteresis below 10° .^{133,136–139}

Current interest is moving towards alternatives to silane for surface energy reduction.^{128,136–138} Based on how the functionalities performed in fabrications of superhydrophobic coatings, organic and bioinspired materials such as carboxylic acids and amides have been applied.^{128,136} These materials have fewer hazards and are readily available from nature hence minimising both environmental and health hazards even further.

Fluorinated silanes can be easily substituted with long chain hydrocarbon groups, such as trimethoxy(octadecyl)silane (TMODS),^{118,129,130} as these inhibit liquid-solid interactions, however, they are limited by the lack of electrostatic interactions and limited ability to repel oils due to higher surface tensions.^{140,141} All organic bioavailable materials show great promise in both superhydrophobic behaviour as well as further reducing impact on environment fabrication of these coatings.

Superhydrophobic surfaces over recent years have been developed with a vast array of applications in a range of areas, including self-cleaning surfaces,¹ reduction of drag,² anti-icing,^{3,4} self-healing,⁵ and various other areas.^{6,142–144}

1.6.1 Anti-Icing

Icing causes a vast amount of issues in cold climates as well as aviation industry. In the latter, ice build-up can cause damage to plane wing structure, increase drag which yields in higher fuel consumption whilst in cooler climates it can interfere with day to day items such as locks and affect renewable power sources such as wind turbines. Superhydrophobic coatings do not completely stop ice formation, however due to reducing contact between water droplets and the surface, delay the process.^{145–147} Icing will still occur however when temperatures are low enough for extended periods and atmospheric humidity is high enough.

1.6.2 Self-Cleaning

Superhydrophobic coatings with low sliding angles provide great application to smart windows and in solar energy.^{85,87,96,106,142} Dirt particles often cause a reduction to efficiency to photovoltaic cells which require vast quantities of water to clean. This also results in damage to the surface from particles causing scratches. Providing additional barrier between dirt and the coated material along with water mobility allows for more efficient maintenance.

1.6.3 Anti-corrosion

Corrosion heavily impacts a number of industries such as aviation, shipping, automobiles and pipping; often leading to large economic loss.^{148,149} Most commonly known form of corrosion is the rusting of iron containing metals, where in the presence of water and oxygen iron turns to rust. Due to the abundance of oxygen in air, it is therefore easier to reduce or eliminate the contact between the metal and water. To this purpose several coatings have

been developed with such intent with high durability to environment and water flow.^{150–155}

1.6.4 Drag Reduction

Due to the low contact fraction between water and the surface of superhydrophobic coating, there is high mobility for water to travel which permits the surfaces to be used for drag reduction.^{154,156,157} This application has use in water transport such as in pipes or by the shipping industry to reduce energy consumption per mile travelled.^{158,159}

1.6.5 Bactericide

Infection rate from medical devices has increased significantly worldwide, which often results in extra cost from revision surgeries, severe health complications such as sepsis and potential loss of life.¹⁶⁰ This is even more important during times of the pandemic such as the Covid-19. Several superhydrophobic coatings have been successfully fabricated by applying the low water adhesion with anti-bacterial composite components such as zinc oxide, silver and gold to address this growing issue.^{161–163} Further applications of such coating have been studied towards anti-biofouling of naval vessels.¹⁶⁴

1.6.6 Oil-water separation

Superhydrophobic surfaces are easily wet by oils, this makes them ideal for separation of oils from water. This feature is of high importance to combat and minimise the impact oil spills have on the environment.¹⁶⁵ Coating materials such as mesh, sponges or membranes, allows for the oil to be recycled by it passing through the material while the water is stopped.^{166,166–168} Not only does this benefit the environment but can further reduce the cost of lost oil.

1.7 Design and application of Superoleophobic surfaces

Hierarchical structures (micro and nano) and low surface tension modification define superhydrophobic coatings. However, these often end up being wetted by “oils” which have much lower surface tension when compared to water. Superoleophobic surfaces (Figure 1.16) hence have the capability to repel “oils” and other hydrocarbon solvents (like hexane) expressing contact angles greater than 150° ,^{125,169–171} however due to the varied nature of liquids that can be defined as oils- often having low surface tensions (the higher this is the easier to repel the liquid- it becomes difficult to exactly define the extent to which a surface is oleophobic). Often hexane- surface tension of 27 mN/m – is used to test this property. Additionally, it is key to point out that most superoleophobic coatings also are superhydrophobic thus they are often referred to superomniphobic or superamphiphobic based on the high contact angle to both water and hydrocarbons.^{172–176}

Fabrication techniques are like those described for superhydrophobic coatings; however, it has been demonstrated that etching and templating techniques yield best results. This is because they facilitate the design of re-entrant or double re-entrant topologies which has been reported to express high oil repelling properties.^{47,177,178} Additionally, fluorinated materials are often used for the design of superoleophobic coatings due to extremely low surface tensions of these materials as discussed in previous sections. However, there is a growing interest in development of these surfaces utilizing greener approaches similarly to superhydrophobic coatings.^{172,175}

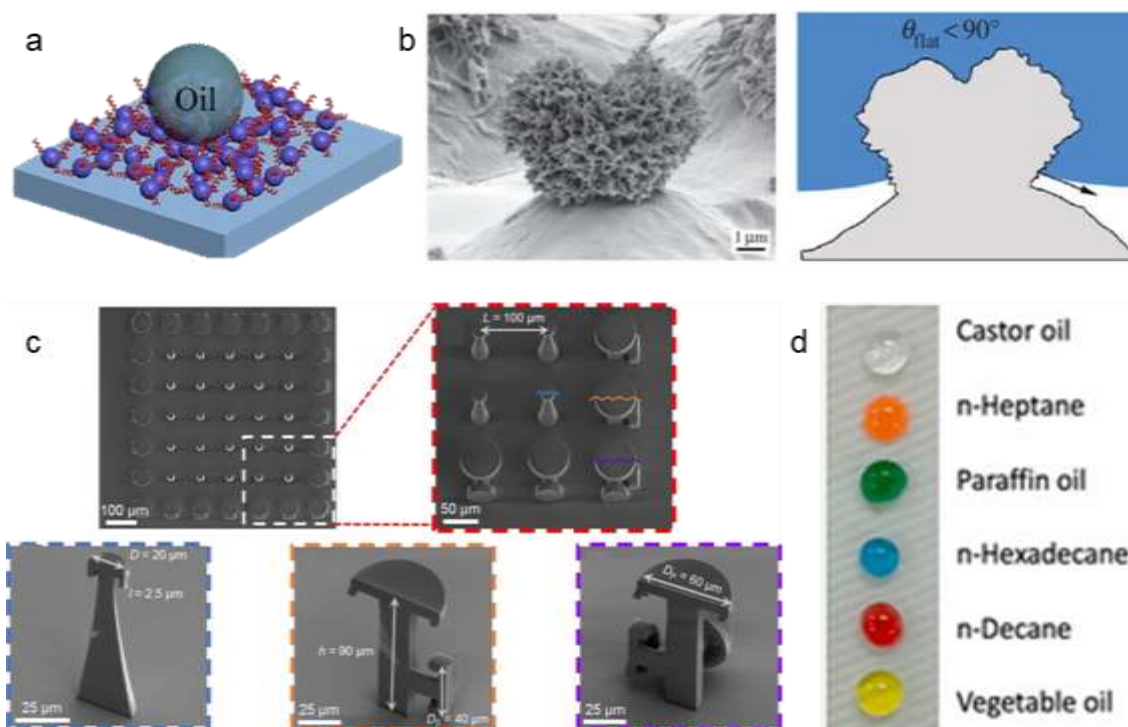


Figure 1.16 (a) Schematic representation of spray coated superoleophobic coating.¹²⁵ (b) SEM image of re-entrant geometry with schematic hypothesized liquid interaction of PC–nanoparticle composite surface.¹⁷⁸ (c) SEM images of arrays of 3D printed doubly re-entrant pillars with various magnifications.¹⁷⁹ (d) Example of various oils repelled by superoleophobic coatings.¹⁷⁴

Superoleophobic coatings perform similar functionality to that of superhydrophobic coatings and as such have been applied to anti-icing, anti-corrosion, bactericide and drag reduction.^{176,180,181} Furthermore, due to their capabilities to repel both water and oils, superoleophobic surfaces have superior self-cleaning properties in setting such as when oil is the dirt which would completely wet superhydrophobic materials. However, due to the same property, there is no application in oil/water separation as both liquids are repelled. To overcome this, research into combining hydrophilicity has led to the development of superhydrophilic-superoleophobic materials.^{182–186} Unlike

standard liquid repelling surfaces, these exhibit preference to wetting with water while continuously repelling oils. This way the mechanism is the reverse of that of oil/water separating superhydrophobic materials.

1.8 Summary

This introduction chapter focuses on a number of key background literature crucial for the design of this thesis. The mechanism, factors affecting synthesis and fabrication techniques of superhydrophobic and superoleophobic surfaces have been introduced. Despite the intended purpose of these two type of materials, they share similarities as in (1) both were designed to repel liquids; and (2) their functionality is highly dependant on the micro/nano scale morphology. However, both of these surfaces exhibit limited multi-functionality while retaining durability and remaining environmentally friendly. This thesis will demonstrate strategies taken in the development of more robust, multi-functional and fluorine-free surfaces.

The flow diagram in Figure 1.17, describes the key milestones of the research pathway taken during the project in order to achieve the desired aims.

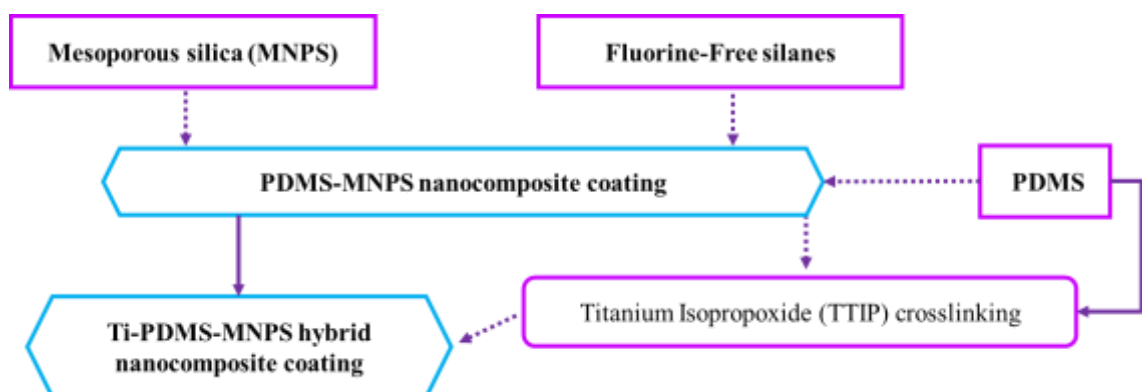


Figure 1.17 Flow diagram illustrating the key concepts for achieving the desired product.

The thesis aims to achieve fluorine-free superhydrophobic coatings with high optical transparency and mechanical durability through the incorporation of porous particles within a polymeric network. The chapters in the thesis outline the work taken in the development of the particles, polymer network and the combination of the two towards achieving the main aim.

In the next chapter (Chapter 2), synthesis and functionalisation of both amorphous and mesoporous silica nanoparticles is discussed. The sol-gel, surfactant templated synthesis allowed for the design of highly porous particles with size of $100 \text{ nm} \pm 20 \text{ nm}$ rapidly and with high control of outcome. The porosity was introduced to help increase transparency of the later fabricated coatings whilst the functionalisation with a silane resulted in better dispersions. Amorphous particles were fabricated following the same method with exclusion of the surfactant template to better understand the pore effect on the resulting coating. The design of a functional polymer utilising various crosslinkers is presented in Chapter 3.

In Chapter 3, hybrid polydimethylsiloxane (hybrid-PDMS) films were developed using titanium isopropoxide as a crosslinker for polymerization. The design followed the aim for enhancing adhesion of the coating to the glass substrate as well as stabilising the polymer in photo active setting. The use of metal oxide precursor for the sol-gel like process was selected with the aim of increasing hydroxy functional groups that would be readily available for bonding with glass directly.

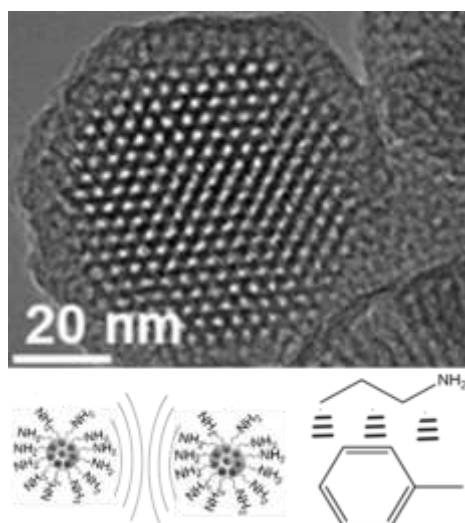
In Chapter 4, three coating methods have been utilised in conjunction with the particles from Chapter 2 and hybrid-PDMS from chapter 3. The resulting

coatings not only inherited the additional functionality achieved by the hybrid films, they achieved high contact angles of 169° with low hysteresis (below 10°) and high transparency- greater than 80% compared to air. Furthermore, AACVD samples also exhibit high durability and adhesion whilst all coatings showed great droplet mobility for self-cleaning applications. Due to the hybrid-PDMS synthesis requiring isopropanol as solvent, the resulting superhydrophobic coatings were alcohol-based.

This thesis achieves robust superhydrophobic surfaces utilising facile and low cost fabrication methods, hopefully one day these techniques will benefit day-to-day life and industry.

Chapter 2

Fabrication of APTES functionalised silica nanoparticles with high control over pore size and shape



2.1 Introduction

The discovery of structured silica nanoparticles such as the ordered mesopores (such as MCM-41, ASM-10 or SBA-15) since the nineties,¹⁸⁷ with porous silica morphology control sub 10 nm has increased in research attention as shown in Figure 2.1. With further developments in understanding that the reaction conditions as well as additives have on the resulting structure, a large variety of particles have arisen.

Whilst the Stöber reaction and sol-gel process are still the main synthetic route approaches with many examples and reviews,^{9,17,195,187–194} many modifications to these have shown the rise of various particle structures including the use of surfactants and templates to dictate the porosity and inner structure;^{9,17,188,189} organic solvents for morphology modification;⁹ solvent-free approaches to create 3D structures and reduce waste;¹⁹¹ additional treatments resulting in

dendritic particles^{10–13} and varying particle size combination which resulted in raspberry structured particles.¹⁴ Their applications have also grown within material fabrication with examples of superhydrophobic surfaces,^{85,114,115} drug delivery,^{11,192} sensors^{196–199} and catalysis.^{200–203} Hence the understanding of the various synthetic routes, the effects of different conditions and additives is important to further the technological developments.

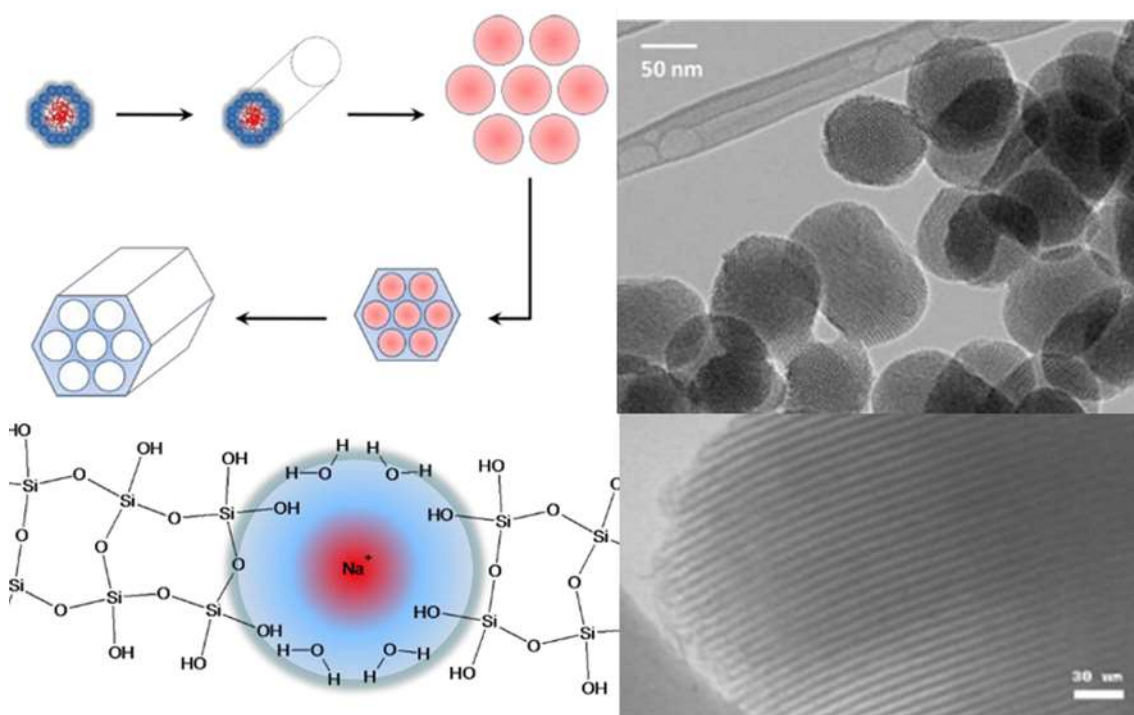


Figure 2.1 Examples of mesoporous silica particles and their key fabrication steps.

This chapter introduces various approaches to mesoporous silica particles (MNPs) synthesis and functionalization found in literature. Further explanation on the effects of surfactants and reaction conditions are examined followed by discussion on the approaches to grafting functional groups onto the particles. The chapter then focuses on the methods used in the thesis to fabricate 3-aminopropyltriethoxysilane mesoporous silica nanoparticles (APTES-MSNPs)

functional particles with tested pore diameter of 3 nm and particle size 100 nm as thoroughly characterized through TEM and solid-state NMR whilst the functionalisation was further confirmed through ATR-FTIR and TGA.

2.1.1 Synthesis of silica nanoparticles with controlled morphology

The synthesis of silica particles using tetraethyl orthosilicate (TEOS) was first reported by W, Stöber in 1968.²⁰⁴ Since then, the reliance on the hydrolysis of TEOS has been widely applied in the field of particle synthesis.^{17,192,205–209} The reason behind this is ease of fabrication of this precursor as well as the well-established reaction pathway within both basic and acid conditions.

However, TEOS is not the only source of silica that can be utilized for synthesis with materials such as sodium silica solution,^{210–214} rice husk,^{210,215} and clays²¹⁶ all finding their applications. The predominant drive for this is the environmental impact of fabrication of TEOS as well as the drive to recycle typically considered waste materials, which has inspired many researches to find new and alternative precursors.

For the controlled synthesis of the mesopores, surfactants often played a key role. Depending on their interactions with the reaction solvent, various micelle structures have been achieved due to the preferred surfactant “head” and “tail” arrangements as exemplified in Figure 2.2.

Over the years, several types of surfactants have been utilised in the synthesis process such as cetyltrimonium bromide (CTAB) or cetyltrimonium chloride (CTAC) as cationic surfactants,^{9,17,190,215,217,218} sodium dodecyl sulphate (SDS) as

anionic surfactant²¹⁹ and polyoxyethylene(12) nonylphenol ether (PN12) as nonionic surfactant.²²⁰ Most commonly cationic surfactants are used due to the polarity of the solvent in synthesis (water/ethanol) as these often form spherical or hexagonal micelle arrangements and are greatly influenced by nonpolar solvent additions.

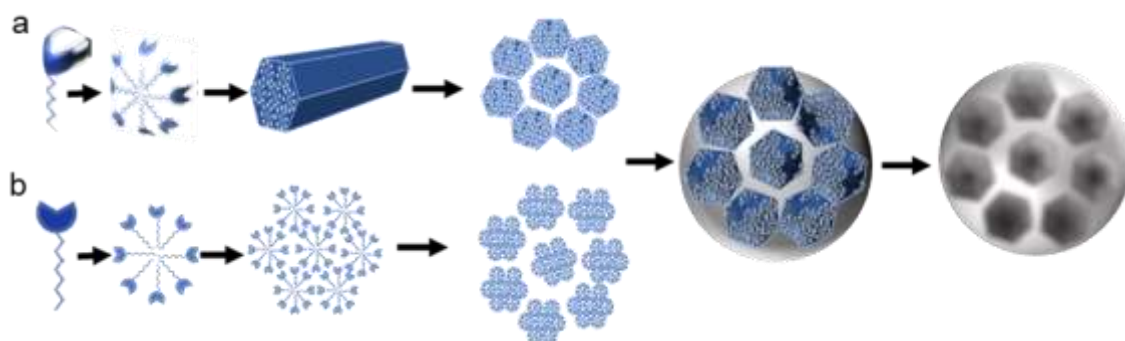


Figure 2.2 Schematic representation of spherical mesoporous silica synthesis using a cationic surfactant for example CTAB (a) 3D and (b) 2D.

The use of cationic surfactants has been well established in literature where the pore diameter for materials such as CTAB have been shown to be reliably in the region of 3 nm.^{9,17,190,221–223} This reliability can be attributed to the formation of hydrodynamically stable micelle in polar solvents such as water or ethanol as the molecules arrange to minimise Gibbs free energy and reduce the interaction between the non-polar tails and polar solvent. These two affinities cause the individual molecules to arrange in a way that minimises the contact of the long hydrocarbon chains of surfactants with polar solvents while exposing the polar heads on the molecules resulting in predictability of the micelle such as hexagonal shaped for CTAB.

Studies have shown that modifying the polarity of the solvent or using a non-polar solvent affects the size or shape of the micelles.^{9,217} Introduction of various polarities can result in modification to micelle arrangements depending on which part (tail or head) of the surfactant molecule has hydrophobic and hydrophilic affinities. This has been extensively studied in oil-in-water emulsion synthesis of particles where a surfactant can be used to encapsulate oil droplets and allow permeability to silica source and polymer monomers into the droplet or build around it.^{17,190}

Anionic surfactants work in a similar manner to cationic ones and have been successfully established as a method for pore templating.^{224–227} Similarly, the formation of the micelles is directed by surfactant-solvent interactions where the molecules arrange according to hydrophobic/hydrophilic interactions of the “head and tail” nature of surfactant structure. The benefit of anionic surfactants is that these permit for lower toxicity of the template material compared to cationic surfactants with examples being sodium dodecyl sulphate (SDS)²²⁵ often found in shampoos or amino acid polymers,²²⁶ the latter of which have been studied by Chandra and Tyagi to be low in toxicity and highly biodegradable.²²⁸

Nonionic surfactants have allowed for the use of non-polar solvents for the fabrication of porous silica particles.^{220,229} Often, the materials used for this type of template are block-copolymers such as poly(ethylene glycol)-block-poly(propylene glycol)-block-poly(ethylene glycol) (Pluronic P123) or (poly(ethylene oxide)₁₀₆-poly(propyleneoxide)₇₀-poly(ethylene oxide)₁₀₆ (PEO₁₀₆PPO₇₀-PEO₁₀₆) (Pluronic F127).^{230–232} The high tendency to form an ordered mesophase makes the use of pluronic advantageous compared to

other templates. These surfactants not only function as structure-directing agents but also promote the synthesis of ordered mesoporous silica in acidic hydrophilic media above the isoelectric point of silica which results in a slower but more controllable rate of condensation of the silica species compared to synthesis at pH greater than 6.²³²

Mixing of surfactants as co-templating method has also been shown to allow for the fabrication of new and more intricately structures particles. Combinations of nonionic with cationic and anionic with cationic have resulted in a great number of new structures such as dendritic particles.^{206,210,223,233–236} Combining organic acids with cationic surfactants has also been of growing interest in particle synthesis.^{237,238} The combination of the cationic surfactant and carboxylic acid allowed for the formation of specific orientation and location grafting of the acid around the pores which has great applications in targeted drug delivery.^{237,238} Further to this they demonstrated greater control of drug delivery over conventional not loaded drug and showed how varying the acid chirality affects the drug release rate.

Hard-templating and surfactant-free approaches have been developed over the years to achieve a greener synthesis by reducing waste or provide greater control of final structure. Surfactant-free synthesis has been reported using organic templates,^{239,240} inorganic templates^{191,241} and etching.^{205,242} These alternatives often require additional treatments to remove the templates but provide a wider range of particle morphologies such as hollow particles or simplify the process of fabricating controlled pores like in the case of etching.

2.1.2 Functionalisation of silica nanoparticles

Functionalizing the silica particles with silanes such as APTES groups works in two ways:^{221,227} 1) the grafting reduces the surface energy of the particles and 2) adds steric hinderance between particles. Both result in better particle dispersions when applied to coatings, as depicted in Figure 2.3.

The use of silane functionalisation of particles has been demonstrated by many in literature ¹⁵⁻¹⁷ and has been reviewed elsewhere.²⁴³ However, the key points have to be highlighted here to better understand why this extra step is so beneficial especially when applying particles to nanocomposites, especially for coating fabrication.

Due to the polar nature of the synthesis solvent for silica particles, they often agglomerate and have poor dispersibility in nonpolar media. To counter that, functionalising the particles with hydrophilic and/or bulky hydrocarbon groups has been used to great success.^{244,245} The stearic hindrance and decreased polarity of the particle surface promotes particle separation whilst the addition of hydrocarbon chains removes the silanol group from the surface (which can undergo hydrogen bonding with water and alcohols) and replaces this with potential van der Waal's interactions.

Further to particle – particle and particle – solvent interactions, the additional functionality can enhance the applicability or use of particles. There have been, due to the readily available surface of the particle for functionalization, uses for silica particle in many fields ranging from biomedicine^{243,246} to surface modifications²⁴⁴ and oil-water separation²⁴⁵ or purification systems.¹⁶

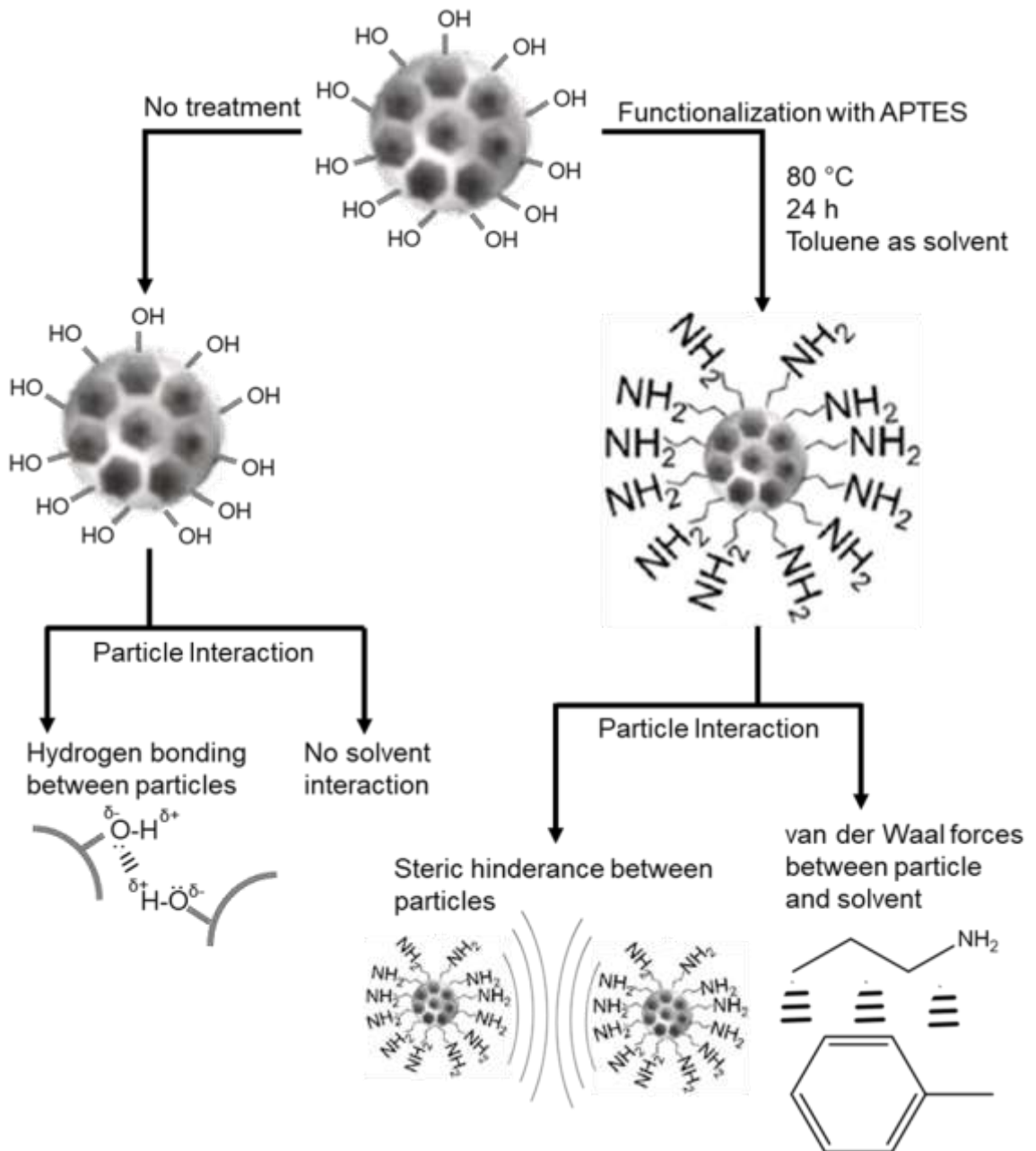


Figure 2.3 Visualization of the effect functionalization of the silica particle has on dispersion in solvent.

2.2 Chapter outlook

This chapter outlines the synthesis approach for mesoporous silica particles and their further functionalisation for application in coating fabrication. The selected method outlined in this chapter yields highly porous particles with

uniform size of 3 nm with high control of particle size of 120 nm \pm 5 nm. The previously reported method, was chosen for the ease of fabrication and high scalability of the process up to 500 mL batch synthesis used in this work. The method was further adapted to include acidic alcohol washing to eliminate the need for calcination at high temperatures (around 600 °C) to remove the template, relying on increased polarity of the extracting solvent compared to the water media used in synthesis.

Post fabrication functionalisation of the silica particles was achieved using (3-aminopropyl)triethoxysilane (APTES) to reduce the hydrophilic nature of the particles through the introduction of hydrocarbon chains at the surface of the particle. The modification also benefited the dispersion and stability of the nanocomposite of coatings discussed in Chapter 4 with detailed evaluation of the implication of APTES functionality depending on coating method. Success of the process was confirmed using FTIR and TGA analysis with calculated 25 % of particle mass corresponding to the functional group of the grafted silane.

2.3 Experimental

2.3.1 Materials

Tetraethyl orthosilicate (TEOS) (98%, Merck) was obtained as the source of silica for the fabrication of silica nanoparticles where sodium hydroxide (NaOH) (\geq 98%, Merck) was used as catalyst and control of the condensation process by creating a basic environment for the synthesis. Hexadecyltrimethylammonium bromide (CTAB) (\geq 98%, Merck) was purchased to be used as the pore directing agent – resulting in a soft template within the particle structure for which ethanol

(EtOH) (95%, Merck) and Hydrochloric acid (37 %, Merck) was used to remove it. (3-aminopropyl)triethoxysilane (APTES) ($\geq 98\%$, Merck) was used for functionalisation of the fabricated silica particles in toluene ($\geq 99.5\%$, Merck) as the nonpolar solvent for the process. The purchased reagents were used without prior modification or purification. Distilled water was used throughout the experiment during the synthesis of the particles.

2.3.2 Particle synthesis and functionalisation with APTES

To obtain mesoporous 120 nm silica particles (MSNs), a modified approach of the Han et al method was undertaken.⁹ The modifications to the method included the omission of the dodecanol and the upscaling of the method was done successfully as depicted in Figure 2.4. Further novelty to the method was the incorporation of the CTAB removal through the use of acidic alcohol as well as the incorporation of the functionalisation of the silica particles.

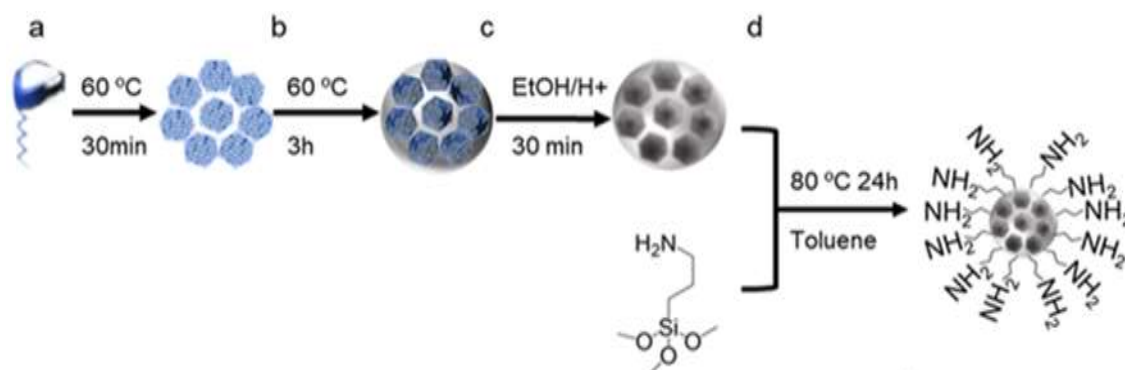


Figure 2.4 Schematic representation of spherical mesoporous silica synthesis and APTES functionalisation (a-b) Micelle formation and arrangement (c) Particle formation (d) Particle functionalization.

In brief, 0.3 g of sodium hydroxide was dissolved in 500 mL of distilled water under fast magnetic stirring of ~1000 rpm. The basic solution was heated to 80 °C and 1 g of CTAB was added and slowly stirred until fully dissolved at a rate of 350 rpm. It took ~30 minutes for the surfactant to dissolve. Subsequently, 7.5 mL of TEOS was added dropwise over a 2 minutes period and the reaction was kept under increased speed of magnetic stirring (1000 rpm) for a further 3 hours. Upon completion of the reaction, the suspension was left to cool to room temperature and the particles were collected via centrifugation at 10000 rpm for 15 minutes. The particles were washed with ethanol and re-dispersed at 60°C acidic alcohol (1 mL HCl in 100 mL ethanol) and stirred at room temperature for 30 minutes to remove the surfactant template from the mesopores. The sample was then once more collected and washed in ethanol before drying in an oven overnight at 80 °C. The particles without pores were synthesized following the same method described for the porous silica, however, the CTAB template was not used in the synthesis which resulted in the omission of the wash in acidic ethanol.

Functionalization of particles was achieved with APTES to enhance the dispersion through introduction of steric and functional hindrance. Reported elsewhere,¹⁵ 1 g of ASNPs was dispersed in 50 mL of toluene followed by the addition of 3 mL of APTES. The suspension was heated to 80 °C and stirred for 24 hrs. The resulting particles were centrifuged (10,000 rpm, 15 min) and washed with ethanol then dried at 80 °C overnight.

2.3.3 Characterization

Attenuated total reflectance Fourier-transform infrared spectroscopy (ATR-FTIR) measurements were taken using MIRacle™ single reflection horizontal ATR accessory with a ZnSe single reflection crystal plate. The analysis was done in the range of 400 to 4000 cm^{-1} and data obtained was plotted in Origin software. ^{29}Si Solid State Nuclear Magnetic Resonance (^{29}Si ssNMR) experiments were carried out on Bruker Avance 300 spectrometer with 7.05 T wide-bore magnet at ambient probe temperature. High-resolution solid-state ^{29}Si were recorded at 59.6 MHz using a standard Bruker 4 mm double-resonance magic-angle spinning (MAS) probe. Solid materials were packed into zirconia rotors of 4 mm external diameter and spun at the MAS frequency of 8 kHz with stability better than 3 Hz. High-resolution solid-state ^{29}Si NMR spectra were recorded using MAS and high-power proton decoupling. Typical acquisition conditions for ^{29}Si MAS experiments were: ^{29}Si 30° pulse duration = 1.8 μs ; recycle delay = 30 s; acquisition time = 43 ms. ^{29}Si chemical shifts are given relative to tetramethylsilane (TMS). Tris(trimethylsilyl)silane (TTMSS) was used for the chemical shift calibration, with the ^{29}Si chemical shifts of -9.84 ppm and -135.4 ppm relative to TMS. Thermogravimetric Analysis (TGA) was utilised to quantify the concentration of APTES groups grafted onto the surface of silica particles. Particle size distribution of nanoparticles was determined in suspension using Dynamic Light Scattering (DLS) Malvern Zetasizer Nano (ZEN3600). These sizes utilised the phenomenon of dynamic light scattering (also called quasi elastic light scattering [QELS]) and Photon Correlation Spectroscopy [PCS]) using a measurement angle of 173° . The instrument was

calibrated using a known size standard (NanosphereTM 3200A 199±6 nm). Samples were prepared by sonication and measurements were performed in clear plastic cuvettes with a light path length of 1 cm. Surface morphology of the samples was observed using Scanning Electron Microscopy (SEM). Images were obtained using JEOL JSM-IT100. To prevent charging, samples were gold-sputtered with SC7620 mini sputter coater. The SEM images for morphologies of AACVD superhydrophobic coatings were generated under the JSM-7600F Field Emission SEM, JEOL, Japan. Vacuum sputtering samples with very thin gold film in order to improve the electrical conductivity of surface. Further characterisation of the nanostructures was conducted using Transmission Electron Microscopy (TEM) JOEL JSM-2100. For the particle analysis, the sample was dispersed in methanol to promote mono-dispersion for clear images. The hybrid-PDMS films were analysed without prior modification due to the transparency obtained with the sample allowing direct analysis of the metal oxide species.

2.4 Results and Discussion

2.4.1 Chemical composition

Attenuated total reflectance Fourier-transform infrared spectroscopy (ATR-FTIR) characterization, shown in Figure 2.5a, was used to confirm successful washing and functionalization of the particles whilst nuclear magnetic resonance (NMR) in Figure 2.5b confirms the porosity of the particles due to presence of various environments. Thermogravimetric analysis (TGA), shown in

Figure 2.5c, was used to further confirm functionality as well as quantify the extent of the grafting.

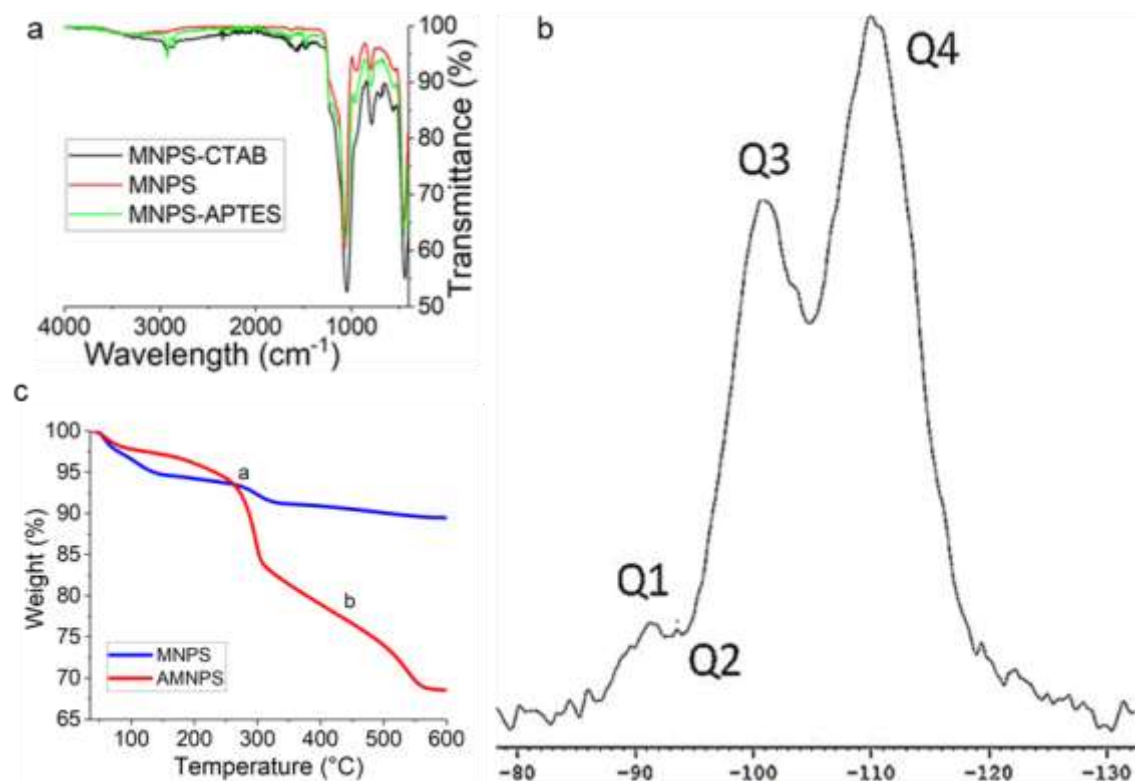


Figure 2.5 Chemical analysis of the particles (a) ATR-FTIR; (b) ²⁹Si-ssNMR and (c) TGA of both mesoporous and APTES functionalized silica (the a indicates area of loss of moisture and b indicates area of loss of amino functionality from APTES).

From the obtained ATR-FTIR spectra, the particles were confirmed to have fingerprint peaks for silica. Upon further study, red shifts in the spectra were observed, from 1086 to 1052 cm⁻¹ (shift of 34 cm⁻¹) for transverse-optical mode of the Si-O-Si lattice and from 811 to 793 cm⁻¹ (shift of 18 cm⁻¹) for Si-O-Si symmetric stretching vibration band. This indicates the formation of silica with a more open network (Si-O-Si bond) suggesting the presence of porosity in the sample.

The functionalization with APTES was confirmed via ATR-FTIR, as shown in Figure 2.5a, with the presence of C-H stretch at 2900 cm^{-1} , as well as two small peaks 3240 cm^{-1} and 3360 cm^{-1} representing N-H stretch. Further peaks at 1610 cm^{-1} and 1300 cm^{-1} corresponding to C=N and C-N bonding can also be observed. The emergence of a peak $\sim 720\text{ cm}^{-1}$, corresponding to SiOC interactions, can also be seen in the spectra.

Silica environments present in the mesoporous silica particles were evaluated using ^{29}Si -ssNMR, as shown in Figure 2.5b. Four distinct environments were observed, indicating that there are four different ways of oxygen binding to silicon, labelled as Q1 to Q4 in Figure 2.5b with Table 2.1 defining these terms represent around the analysed silicon atom.

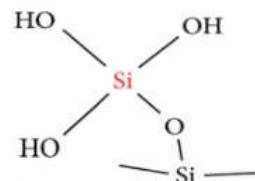
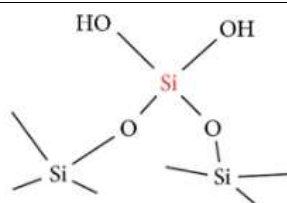
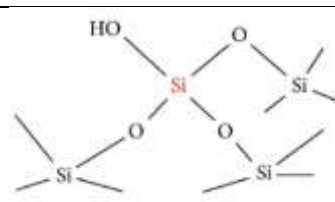
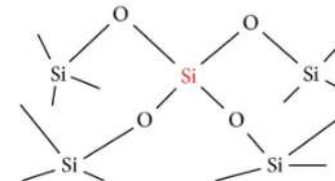
Environment label	Environment around the analysed Si atom
Q1	
Q2	
Q3	
Q4	

Table 2.1 Description of the Q1 - Q4 environments as indicated in Figure 2.5b.

Introduction of mesopores into the material causes the number of binding oxygen atoms to a silicon to change depending on the location of the binding in relation to the pore. Surface silica exists as quadruple bonded silicon to four oxygen atoms, as shown at -110 ppm (Q4 in Figure 2.5b) which is associated to any silica complex, for example the same peak can be seen when analysing sand²⁴⁷ or non-porous particles. The further peaks observed at -101 ppm, -93 ppm, and -91 ppm are expected for mesoporous silica.²⁴⁸

Thermogravimetric analysis, shown in Figure 2.5c, compares the pre-functionalized and post-functionalization particles. The graph has been split into two distinct regions (a and b) with each demonstrating different loss of mass. In zone a, the particles lose moisture that had adhered from the atmosphere as well as during synthesis. This accounts for about 5% loss in weight for both particles and the loss from moisture stops around 275 °C. Beyond this is zone b which is representative to the loss of the functional group of the silane grafted onto the particles. For the APTES functionalized mesoporous particles, the weight loss was about 25% whilst in the non functionalized particles we see a drop of 5% was observed despite no APTES being used in the synthesis. The loss in the MNPs can be attributed to CTAB used in the fabrication which was not fully removed during the cleaning step with the acidic ethanol prior to analysis.

To calculate the concentration of the APTES grafted onto the silica nanoparticles, TGA was utilised where the weight (%) difference was utilised to calculate the weight (%) of APTES groups from Figure 2.5c. Converting the weight change (%) into mass lost allowed for the calculation in APTES functional group. From zone b in Figure 2.5c, the weight (%) change for AMNPs

was 25% which using the mass of sample and molecular weight of the aminopropyl group of APTES means that 33.26 μmol have been grafted onto 96.52 μmol of particles.

2.4.2 Particle morphology

Scanning electron microscopy (SEM) in Figure 2.6a-b were used to confirm particle size and silicon environments whilst transmission electron microscopy (TEM) in Figure 2.6c was used to determine pore size. Synthesized non-porous silica particles have been imaged in Figure 2.6d displaying particle size.

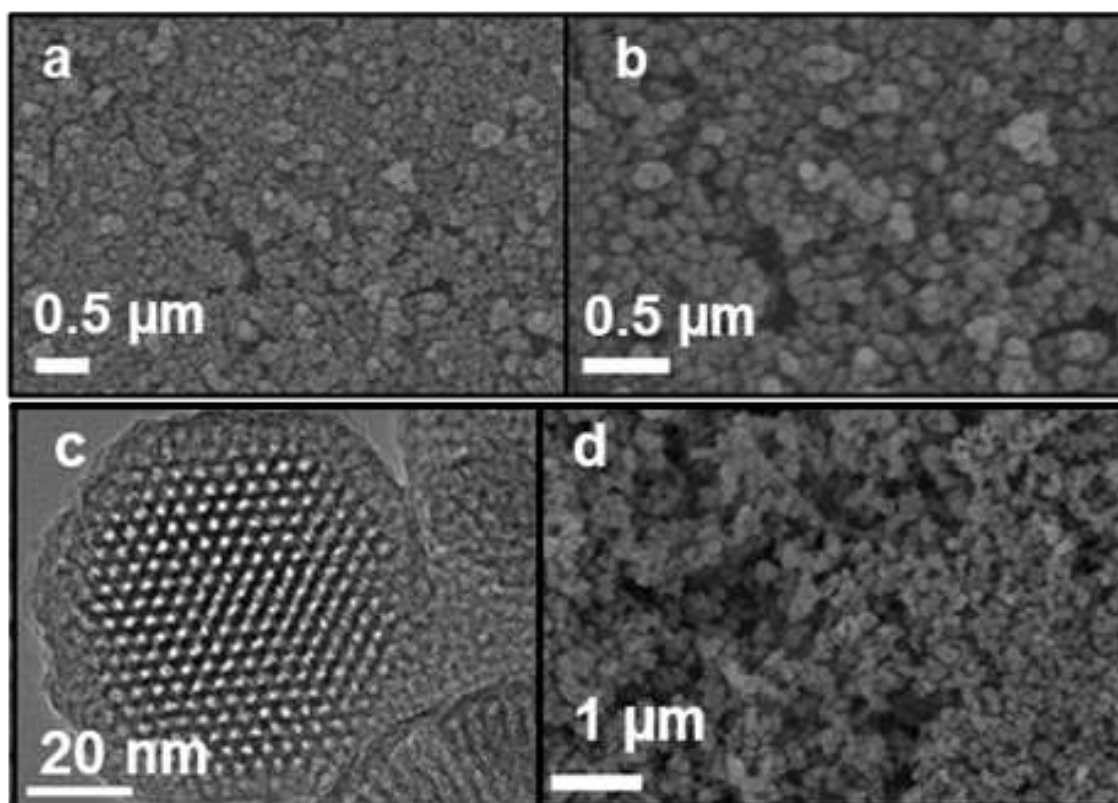


Figure 2.6 Morphology analysis of the (a-b) SEM of mesoporous silica (c) TEM of mesoporous silica and (d) SEM of amorphous silica.

Particle size was confirmed using SEM (Figure 2.6a, Figure 2.6b and Figure 2.6d) with an average of 120 ± 5 nm. This corresponded well to a size of 90-140 nm measured using dynamic light scattering (DLS) with highest intensity peak

seen at 118 nm. Furthermore, the particles can be seen to be spherical shaped, which was reported by Han *et al.*,⁹ indicating successful synthesis of the silica nanoparticles. From Figure 2.6c, it is observed that the mesopores of the particle had an average size of 3 nm. This along with the NMR confirms the porous structures of the particles.

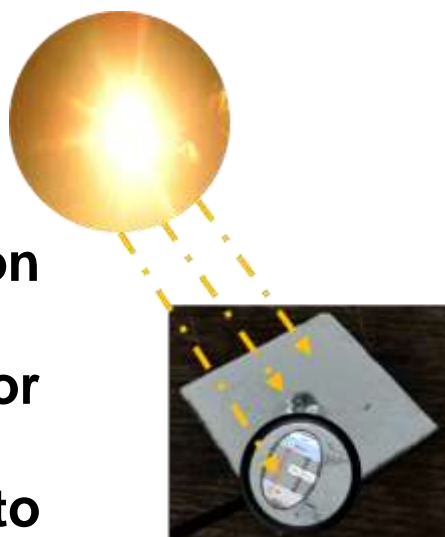
2.5 Conclusion

Successful synthesis of mesoporous silica nanoparticles has been demonstrated and characterized through solid-state NMR, FT-IR, SEM and TEM imaging. The modifications to the method reported by Han *et al.*⁹ allowed for the upscaling of the process to the tested x10 in volumes of reagents, resulting in a highly reliable method for the synthesis of porous silica with known porosity and easily controlled particle sizes.

The functionalization of the particles was confirmed through FTIR characterization and TGA analysis as often done to assess successful functionalization of particles with a silane.²⁴³ The additional step in the particle fabrication greatly impacts their applicability to the further formulation of composite coatings described within chapter 4. FTIR peaks at 2900 cm^{-1} and two small peaks 3240 cm^{-1} and 3360 cm^{-1} representing N-H stretching vibrations demonstrate successful grafting of the APTES functionality to the particles. TGA analysis confirmed 33.36 μmol of the silane was grafted onto 96.52 μmol of silica particles, demonstrating the success of the functionalization method and help to explain the extent that the APTES aided in the dispersion of the particles in less polar solvents used for nanocomposite coatings as discussed further in chapter 4.^{221,227}

Chapter 3

Titanium dioxide hybridization of polydimethylsiloxane for applications in photo responsive superhydrophobic coatings



3.1 Introduction

Polydimethylsiloxane (PDMS) has often been used as the polymer of choice for superhydrophobic coatings^{94,249–251} because of its hydrophobic nature as well as transparency when cured even at large thicknesses due to the homogenous nature of the polymer. PDMS has been extensively studied and reviewed elsewhere,^{252,253} however it is key to highlight that it has been utilized in a vast array of applications such as medical,²⁵⁴ membranes and sponges,²⁵⁵ microfluidics^{22–25} and coatings.^{3,94,96,197,249–251,256–258} Due to its versatility, it is often the polymer of choice in liquid repelling surfaces.^{131,169,259,260} PDMS is a transparent polymer in the visible region with a refractive index reported as 1.41 and when cured, at lower than the manufacture recommended polymer to bridging agent ratio, is flexible which would enhance drop impact resistance. Research into PDMS-particle interactions has allowed for vast surface

development that is also utilised in this project.¹⁹⁷ However, due to the nature of the polymer, it does not bind to glass which reduces mechanical robustness of the coating. To address this concern, an *in situ* sol-gel approach to bridge PDMS monomers with metal oxides was adopted in this work.^{7,143,261}

3.1.1 Titanium hybridization of PDMS for additional functionalities

Superhydrophobic coatings is an area where functionalising polymeric network will have deep impact. Through the composite approach to coating fabrication, polymer matrix plays a crucial role in both chemical and physical properties. Achieving durability and maintaining functionality of coatings with low surface energies is often challenging especially in photocatalysis as the process tends to be destructive to the material.

However, recently a focus on fabrication of hybrid-PDMS has been noted especially for composites in the nano scale to achieve their desired properties. Over recent years, there has been a high drive for nanocomposites that retain the benefits of the matrix material (such as PDMS) whilst introducing additional functionality such as antibacterial or anti-fouling properties, photocatalytic behaviour, or enhanced liquid repellence.^{262–264}

To meet the demand, hybrid materials comprising of organic and inorganic precursors have been developed with predominant focus on incorporation of pre-synthesized particles into the polymer by some means of mixing (stirring, sonication etc.). However, this method has its restrictions based in particle fundamentals such as agglomeration of nanoparticles or is limited by

compatibility to matrix properties such as refractive index or bond stability. This is especially exemplified in coatings or optical applications of PDMS, where additional functionalities such as superhydrophobic roughness or photocatalysis often reduce transparency of the nanocomposite or resulting surfaces due to the concentration of particles required. This is supported by literature as higher concentration of particles means there is a greater chance of light being scattered by a particle due to reduced homogeneity of the composite.²⁶⁵

Approaches to introduce inorganic components within the PDMS network have been successfully attempted by several researchers using hydroxy terminated PDMS (PDMS-OH) at various viscosities.^{7,258,266,267} The goal illustrated in Figure 3.1, where the nanoparticles of the metal oxide have been reported in sizes of 4 nm and fully incorporated into polymer network.

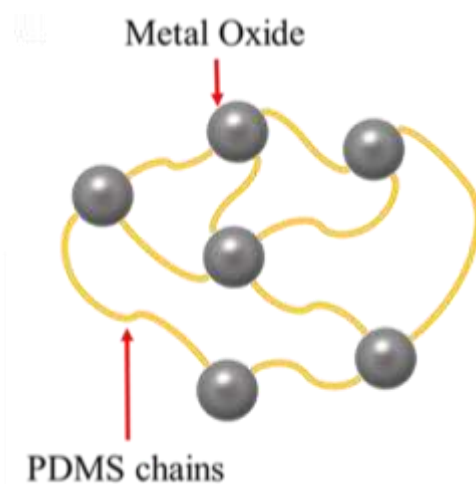


Figure 3.1 Theorised polymer network resulting hybrid network.

The effect of titanium isopropoxide (TTIP) as a source of titanium to crosslink PDMS-OH was conducted by Dalod et al,⁷ where different viscosities ranging from 25 to 750 cst of PDMS-OH were evaluated. The evaluation of the resulting films at various metal concentrations showed the increase in refractive index of

the polymer as well as a decrease in contact angle with increasing concentrations. Morphology analysis has demonstrated particle size/ pocket size of the metal oxide as small as 4 nm, which was homogeneously dispersed within the network resulting in minimal decreases in transparency and low scattering of light.⁷ The crosslinking was conducted in the alcohol of the metal alkoxide resulting in ideal dispersion of the metal source whilst utilizing hydroxylated PDMS allows the use of polar solvents. The compatibility between the polymer and solvent with the metal alkoxide allows for homogeneous dispersion allowing for site specific condensation of the metal oxide pockets within the network at the hydroxy end of the polymer monomers.^{7,258,266,267}

This differs to the crosslinking of the commercial Sylgard 184 network where the platinum catalyst promotes the formation of bonds between the silicone groups resulting in a silicon-oxygen backbone where the silicon and oxygen alternate.²⁶⁸ This results in the elastic properties of PDMS due to the lower torsional potential, longer bond length and increased bond angle between the Si-O compared to that of a C-C bond.²⁶⁹ Furthermore, due to the use of the platinum catalyst, the resulting material retains its optical transparency due to the lack of volatiles being produced unlike during peroxide curing.²⁷⁰ The process occurs at room temperature but is temperature dependant – increased temperatures can facilitate the crosslinking.

3.1.2 Titanium photocatalysts and its place in liquid repelling coatings

The use of titanium dioxide has been thoroughly studied as an additive in coatings and paints for its high photoactivity. Numerous examples can be found

of titanium finding its way into self-cleaning superhydrophobic coatings,^{271–273} oil-water separating¹¹⁷ and other depollution materials.^{274–276} This is often achieved through a combination of water repelling polymer,^{273,277} fluorinated^{117,278} or more recently non-fluorinated silanes^{143,279} for surface energy reduction and other dopant particles to enhance roughness. However, it is necessary to understand the role titania itself plays within these coatings and how it affects wetting on such surfaces.

Titanium dioxide exists in a number of crystal structures: anatase, rutile, and brookite; however only two anatase and rutile exhibit photoactive behaviour. The mechanism behind the interaction between titanium dioxide and photons of light have been extensively studied in literature and as such will only be briefly summarised here based on the diagram depicted in Figure 3.2.

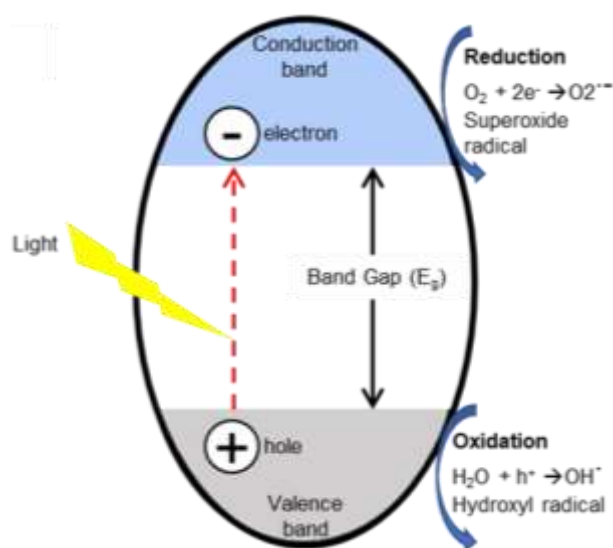


Figure 3.2 Heterogeneous photocatalytic mechanism with TiO₂ as a semiconductor.

In brief, photon of light with energy equivalent or greater than the band gap energy excites valent electrons in the valence band to the conduction band

creating a positive hole.^{280,281} This results in activation of redox potential where an oxidation reaction takes place at the valence band between the positive hole and water forming hydroxyl radical whilst the extra electron in the conduction band reacts with oxygen in the air forming superoxide radicals.^{282,283} These radicals formed from the redox system then are used in depollution reactions such as oil degradation through further radical reactions. Typically, the particles require illumination with ultra-violet light^{280,282,283} to attain enough energy for this process to take place however, dopants and other modifications can result in photoactivity in the visible region.^{284,285}

Focusing on examples of titania based superhydrophobic surfaces, these have found a number of applications in self-cleaning,^{271–273} water purification,^{274–276} anti-icing,^{286,287} and others,^{271,288} as summarised in Figure 3.3.

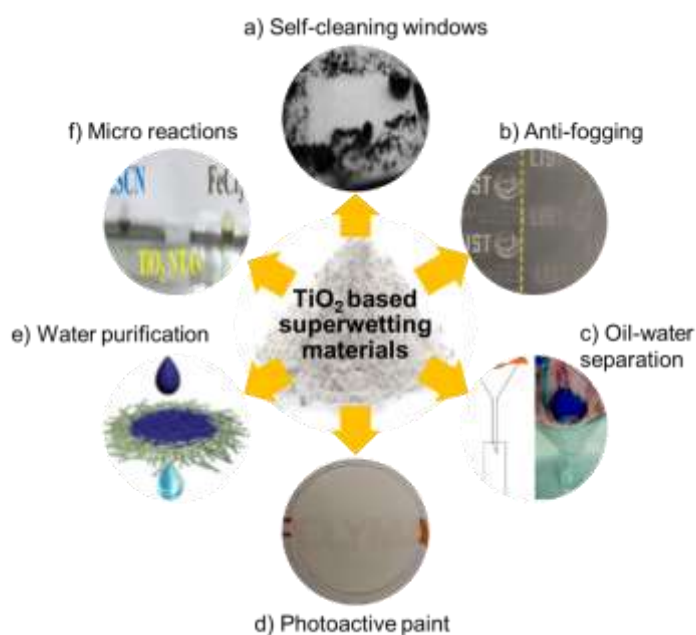


Figure 3.3 Applications of titanium dioxide in superwetting materials (a) Self-cleaning windows²⁷² (b) anti-fogging surfaces²⁷³ (c) oil-water separation mesh¹¹⁷ (d) photocatalytic paints²⁸⁹ (e) Water purification membranes²⁷⁶ (f) Micro-reaction arrays²⁷⁷

This is due to two major properties exhibited by the particles within the coating:

1. photocatalysis and 2. switching from superhydrophobicity to superhydrophilicity upon radiation with UV light.²⁷² As such many different examples of fabrication methods^{117,273,276,277} and particle design²⁹⁰ have been adopted to optimise the surfaces towards target applications.

With the vast array of applications reviewed in literature,^{291,292} this section will focus primarily of photoactive coatings derived with titanium dioxide particles that exhibit superhydrophobic behaviour especially in Cassie-Baxter regime. Key aspects noted in the literature find the transition of the materials between hydrophobicity and hydrophilicity upon irradiation with UV light²⁷² where due to the hydroxy and superoxide radicals forming at the surface. Another finding is the degradation of the polymer^{293,294} used in the composite as the radicals formed do not have selective degradation towards pollutants but all organic components they come into contact with. This is also why the titanium dioxide materials have such high application fields.^{291,292}

3.2 Chapter Outlook

This chapter focuses on the fabrication of photo responsive and superhydrophobic fluorine-free coatings with enhanced resistance to UV exposure through the introduction of titanium species into the polymeric network compared to Syglard 184. This was done due to a number of key factors. Firstly, both Syglard 184 and PDMS-OH result in a transparent polymer in the visible region of light when cured at high thickness allowing for both to be tailored in a composite towards transparent coatings. Secondly both variations of the PDMS have similar interaction with non-polar solvents regardless of the

curing agent providing opportunity to be used with the functionalised particles described in Chapter 2. However, one key difference is the presence of a readily available hydroxy group in PDMS-OH which is not present in the Sylgard 184. This is expected to influence the ability to crosslink the polymer with titanium isopropoxide but also is expected to affect the size of the metal oxide pockets formed within the polymer chains as discussed in Figure 3.1.

The samples prepared using Sylgard 184 and PDMS-OH were fully evaluated in terms of wetting, chemical composition and morphology. Finally, a selection of samples was placed under UV light for prolonged exposure to determine the impact of the titanium species in the polymer network on the stability of the coating with anatase as additive in the composite.

This work evaluates the fabrication of the titanium PDMS hybrid polymer network for coating applications and the effect of concentration of the titania crosslinker on the wetting, transparency and morphology of the resulting films. To that extent several analysis were done such as contact angle measurements to determine the extent of hydrophobicity of the films and the trend increasing Ti presence within the coating has on wetting behaviour. From literature discussed in the introduction, titanium dioxide is by nature hydrophilic due to the potential to form hydrogen bonds, as such it has been hypothesised to cause a decrease in the advancing contact angle with increasing crosslinker concentration. Furthermore, due to the white nature of titanium oxide pigments, it has been also theorised that the increase in concentration will reduce the transparency of the films, however, due to the titanium pockets being reported to be in the nano region the decrease is expected to be small.

Next, the chapter looks at the application of the hybrid polymer as a photo responsive coating where the polymer was combined with fumed silica and anatase. First, to reduce further environmental impact of the fabrication process, carboxylic acids were tested as replacements for silanes for the reduction of surface energy. To that extent, three acids with increasing hydrocarbon chain lengths were selected as it has been demonstrated in literature (discussed in Chapter 1) that longer hydrocarbon chains increase van der Waals interactions and reduce potential for hydrogen bonding between the modified surface and water increasing the contact angle between the two phases and promoting droplet mobility meaning the coatings tend to exhibit Cassie-Baxter wetting over Wenzel. Secondly, anatase concentrations were tested to determine the minimal concentration of anatase needed for the roughness to reach superhydrophobicity.

Finally, UV stability of the formed materials were tested using acid degradation approach and long term UV exposure in a light box. The effect of titanium concentration in the hybrid was tested and compared to a sample of Sylgard 184 with no titanium in the crosslinker as evaluated for long term stability to UV exposure to determine the optimal coating for application as a photocatalytic and superhydrophobic surface.

3.3 Experimental

3.3.1 Materials

Hydroxy-terminated polydimethylsiloxane (PDMS-OH) (750 cst, Merck) was obtained as the polymer component of the films and coatings produced in this

chapter where titanium isopropoxide (TTIP) ($\geq 98\%$, Acros Organics) was utilised as the crosslinking agent in anhydrous isopropanol (IPA) (99.5%, Merck) as solvent. For additional functionality and to facilitate the reduction of contact angle between water droplets and the surface of the coatings, three types of carboxylic acids: palmitic acid (PA) ($\geq 99\%$, Merck), stearic acid (SA) (97%, Acros Organics), lauric acid (LA) ($\geq 98\%$, Merck) were used due to their low environmental impact and varying lengths of the hydrocarbon tails. Anatase (325 mesh, $\geq 99\%$, Merck) and fumed silica (OX50, Aerosil) were used in the coatings as additives for the fabrication of hierarchical roughness within the coatings as well as to explore potential environmental durability of the coatings in exposure to UV light.

3.3.2 Metal Oxide Crosslinking

Hybrid-PDMS material was fabricated following a similar method described by Dalod *et. al.* with specific molar ratios described in Table 3.1. In brief, 3 mL of hydroxylated polydimethylsiloxane (PDMS-OH) was dispersed in 8 mL of isopropanol (IPA) with 5 minutes sonication in sonic bath followed by stirring and heating to 70 °C. In a separate vial, the desired molar equivalent of titanium isopropoxide was dispersed in 4 mL of IPA through 5 min sonication in sonic bath at room temperature. The crosslinker solution was then added to the dispersed PDMS-OH at 70 °C and mixed via vigorous stirring for 30 min at the higher temperature. The resulting sols were sealed to ensure minimal solvent evaporation during reaction. Polymeric films were spin-coated onto glass slides at 3000 rpm for 60 seconds with 300 rpm acceleration.

Sample	MO/PDMS	MO (wt%)	MO (vol%)	M/Si (mol.
---------------	----------------	-----------------	------------------	-------------------

<i>name</i>	<i>(mol. ratio)</i>			<i>ratio</i>
A0	10 : 1	3.99	1.0	0.04
B0	20 : 1	7.99	2.0	0.07
C0	30 : 1	11.98	3.1	0.11
D0	60 : 1	23.96	6.1	0.22
E0	120 : 1	47.92	12.3	0.44

Table 3.1 Calculated metal oxide content and metal/Si atomic ratios of the hybrid-PDMS based on complete reaction.

3.3.3 Liquid repelling coatings

Superhydrophobic coatings were prepared using anatase and fumed silica particles for roughness and carboxylic acid for reduction of surface energy. The specific conditions have been outlined in tables 3.2, 3.3, and 3.4. Each of the coatings were prepared using 4 mL of the polymeric solution prepared above.

<i>Coating name</i>	<i>PDMS used</i>	<i>TTIP : PDMS</i>
A	PDMS-OH	10 : 1
B	PDMS-OH	20 : 1
C	PDMS-OH	30 : 1
D	PDMS-OH	60 : 1
E	PDMS-OH	120 : 1
F	Sylgard 184	10 : 1
G	Sylgard 184	120 : 1
H	Sylgard 184	n/a

Table 3.2 Superhydrophobic coating composition. Each coating was fabricated using 0.4 g anatase, 0.1 g OX50 and 0.665 g stearic acid.

The coatings were prepared by mixing the components outlined in Tables 3.2, 3.3, and 3.4, followed by vigorous mixing for 15 minutes at 750 rpm and sonication for 5 minutes prior to coating. The method did not require extensive mixing to achieve a good dispersion due to polar nature of the solvent used and the non-functionalized particles. Following this, 1 mL of the composite was pipetted onto glass substrate without prior treatment (in the case of samples **F – H** 1 g of coating paste was evenly spread out on the substrates) and excess allowed to run-off the surface. The samples were cured in an oven at 60 °C for minimum of 12 hours.

To evaluate which carboxylic acid would be ideal for functionalisation, three different hydrocarbon chains were selected. The variation in chain length was hypothesised to show different extent of hydrophobic behaviour as the longer the hydrocarbon chain the stronger van der Waals forces meaning the surface would exhibit stronger hydrophobic properties. Coating formulation has been outlined in Table 3.3. The amount of acid added was kept the same in terms of the amount of mols used at 2.3×10^{-3} mol.

Coating name	Carboxylic Acid used	Mass of acid (g)	PDMS used	TTIP : PDMS
A1	Lauric acid	0.465	PDMS-OH	10 : 1
A2	Palmitic acid	0.595	PDMS-OH	10 : 1
A3	Stearic acid	0.665	PDMS-OH	10 : 1

Table 3.3 Superhydrophobic coating composition. Each coating was fabricated using 0.4 g anatase, 0.1 g OX50.

Further study of particle concentration was done to establish the optimal concentration of anatase in the coating to achieve the highest contact angle

while observing the lowest concentration to achieve superhydrophobicity. Table 3.4 outlines the mass of anatase used.

Coating name	Mass of anatase (g)	PDMS used	TTIP : PDMS
A4	0.3	PDMS-OH	10 : 1
A5	0.2	PDMS-OH	10 : 1
A6	0.1	PDMS-OH	10 : 1

Table 3.4 Superhydrophobic coating composition. Each coating was fabricated using 0.1 g OX50 and 0.665 g stearic acid.

3.3.5 Characterization

Attenuated total reflectance Fourier-transform infrared spectroscopy (ATR-FTIR) measurements were taken using MIRacle™ single reflection horizontal ATR accessory with a ZnSe single reflection crystal plate. The analysis was done in the range of 400 to 4000 cm^{-1} and data obtained was plotted in Origin software. X-ray photoelectron spectroscopy (XPS) was performed by Thermo theta probe spectrometer under the base pressure of 5×10^{-10} mbar using the monochromatic Al K- α photoelectron spectrometer with photon energy 1486.6 eV. Surface morphology of the samples was observed using SEM. Images were obtained using JEOL JSM-IT100. To prevent charging, samples were gold-sputtered with SC7620 mini sputter coater. The SEM images for morphologies of the coatings were generated under the JSM-7600F Field Emission SEM, JEOL, Japan. Vacuum sputtering samples with very thin gold film in order to improve the electrical conductivity of surface.

3.3.6 Functionality

For quantitative analysis of coating wettability, dynamic contact angle measurements of advancing and receding contact angles were recorded. Distilled water droplets were generated using a needle connected to a syringe pump. The pump was run in infusion and withdrawal modes to create advancing and receding contact angles, which were recorded using a Navitar zoom lens connected to a CMOS camera. The recordings were digitized into still images and images were taken to measure the advancing and receding contact angles using a MATLAB based image processing script developed in house.⁶⁹ Environmental stability was evaluated using a UV-C chamber where the samples were stored under constant UV irradiation for 21 days. The damage to the coatings was evaluated based on contact angle measurements and FTIR analysis on a set number of day intervals of exposure (day 1, 3, 7, 14 and 21).

3.4 Results and Discussion

3.4.1 Polymeric network

Following the example of Dalod *et. al.* the synthesis of the inorganic hybrid polymer was achieved by mixing TTIP with PDMS-OH in anhydrous alcohol. The resulting polymer suspensions were then spin coated onto glass substrates and analysed, as seen in Figure 3.4 in terms of wetting and transparency. Following this the samples were analysed in terms of chemical composition as shown in Figure 3.5, in order to better understand the noted behaviour through titanium content through XPS focusing on the titanium 2p peaks and ATR-FTIR.

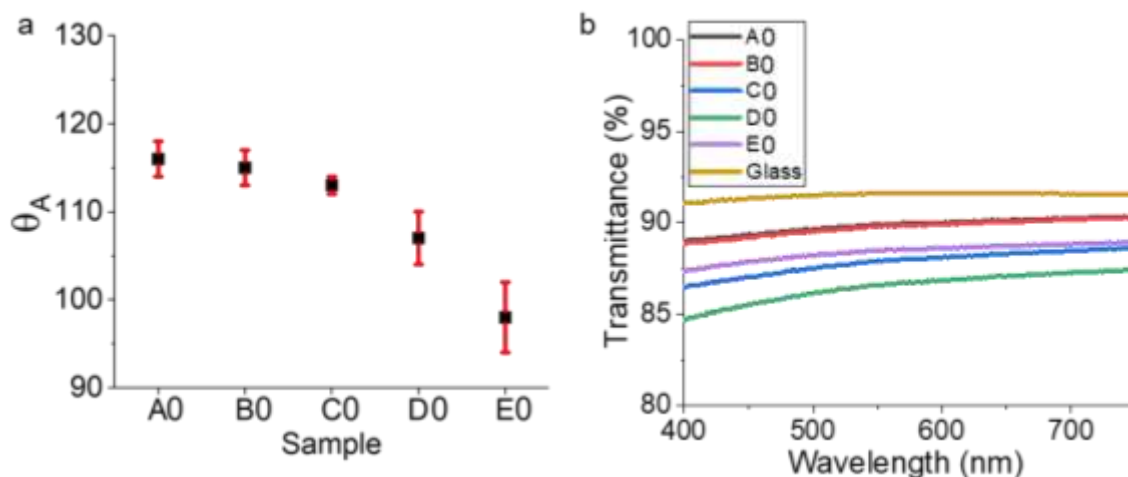


Figure 3.4 Analysis of hybrid polymeric networks by (a) Contact Angle Measurements (b) Transparency measurements done using UV-Vis

When evaluating the effect of concentration on the contact angle, Figure 3.4a, a trend can be seen where with increasing concentration there is a decrease in contact angle. This is supported by literature where similar trends have been shown.⁷ This is the result of increasing metal oxide groups within the polymer network which results in increased sites for water droplets to form hydrogen bonds. The error bars represent the variation of the contact angle measurements across the sample in 5 areas with three droplet analysis of the angle in the software per image taken. This allowed for the measurements to be representative of the sample analysed and factored in the nonuniform nature of the roughness of the surface. A similar trend can also be observed in terms of transparency of the coating, Figure 3.4b, where the increased titanium concentration reduces the optical transparency of the coating. Furthermore, a curvature can be noted at the lower wavelengths of light (below 500 nm) which is indicative of the titanium refraction of light as well as absorbance towards the UV region.

The increased titanium species can be attributed as the cause of the behaviour seen in the contact angle and transparency as seen by the chemical composition analysis, shown in Figure 3.5a-b, by the Titanium 2p peak comparison in the XPS data and the FTIR measurements.

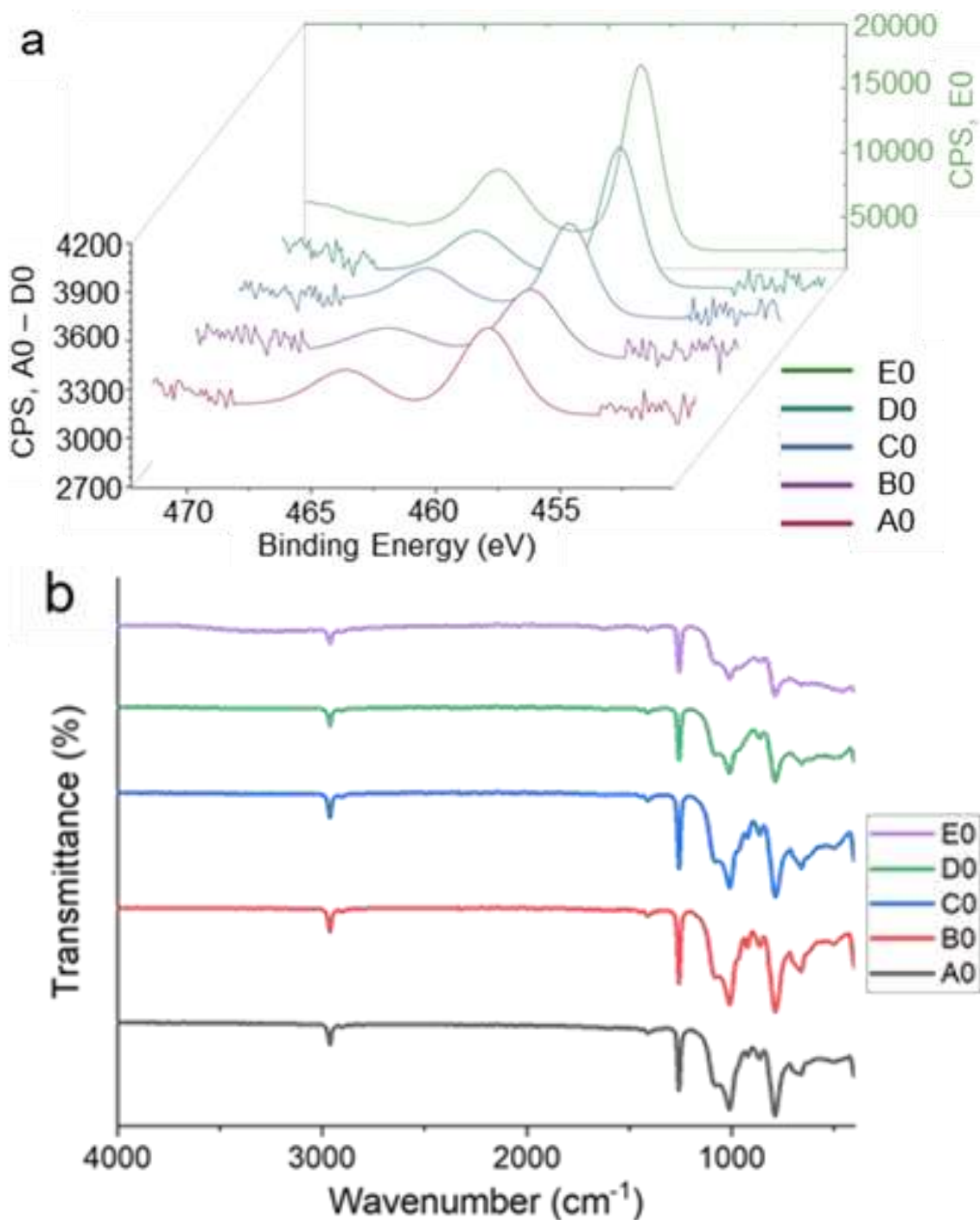


Figure 3.5 Chemical analysis of the polymer films by (a) XPS Ti2p spectra of samples A0 – E0 and (b) ATR-FTIR analysis.

Comparing the polymers formed by variation of the crosslinker concentration, XPS analysis of the titanium 2p peaks, as shown in Figure 3.5a, directly supports the increase in titanium based on crosslinking condition with polymer **E0** demonstrating the most pronounced peaks. From FTIR analysis seen in **Error! Reference source not found.b**, Key peaks at $\sim 420\text{ cm}^{-1}$ and 790 cm^{-1} correspond to Ti–O in amorphous titanium oxide which is expected from the hybrid crosslinking. The distinctive lack of O–H peaks above 3000 cm^{-1} indicate complete crosslinking of the hydroxy terminated PDMS even at the lowest 10 : 1 ratio of titanium to polymer (sample **A0**). This suggests that the further increases in concentration of the crosslinker work to enhance the pocket sizes of the titanium within the polymeric network instead of further crosslinking the polymer. This is further supported by the broadening of the peak at 420 cm^{-1} in the FTIR and the enhancing of the Ti 2p peak in XPS analysis. Other peaks such as the peak $\sim 1000\text{ cm}^{-1}$ are indicative of the PDMS used in the fabrication of the hybrid polymers.

Overall, successful crosslinking of PDMS–OH has been demonstrated through the composition analysis of the materials whilst the wetting behaviour and transparency measurements are indicative of what has been reported by Dalod *et. al.*⁷ showing high transparency and maintaining hydrophobicity, keeping in nature of the PDMS polymer.

3.4.2 Characterisation of coatings

A series of coatings were fabricated following the method detailed in section 3.4.1 and outlined by the schematic in **Figure 3.6**.

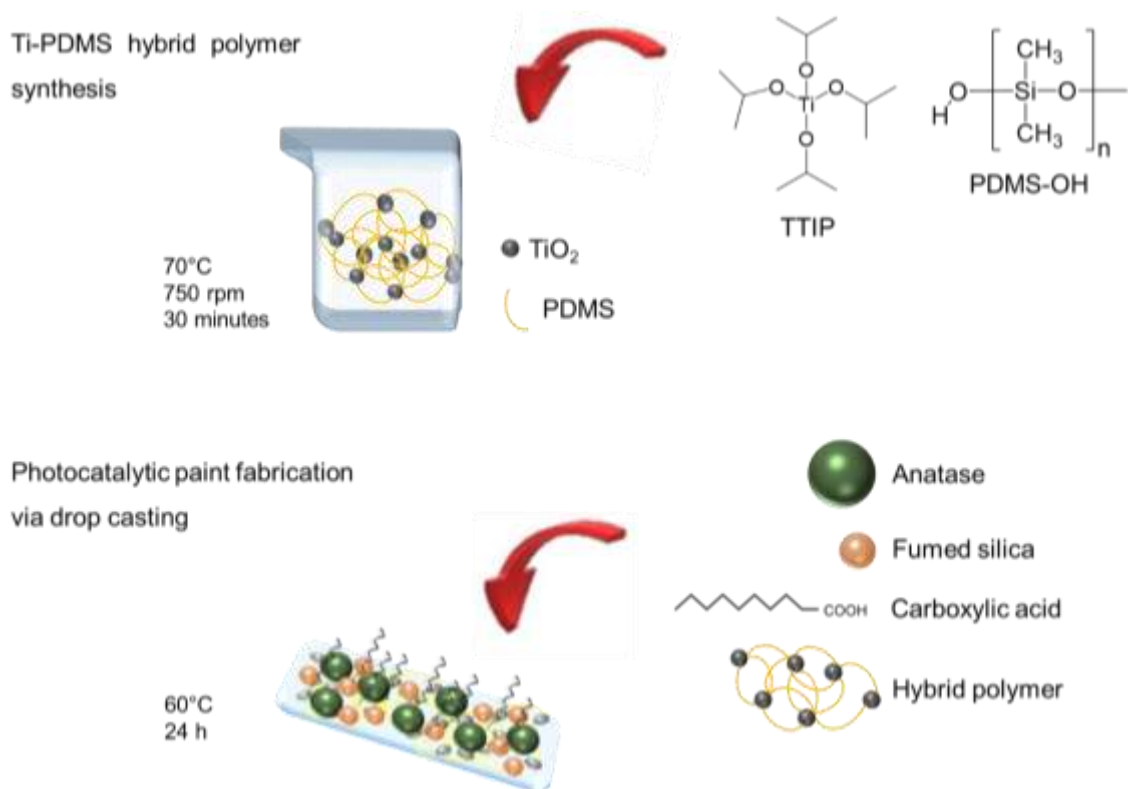


Figure 3.6 Schematic describing the fabrication of the photocatalytic coatings **A** – **E**. The first step was to fabricate the Ti-PDMS hybrid polymer network to which the particles and carboxylic acid was added.

In brief, a polymer suspension in propanol was made by reacting 3 mL of PDMS-OH with a set concentration of titanium isopropoxide with ratios outlined in Table 3.1. For series **A** – **E**, the following was mixed with a 4 mL aliquot of the homogenised polymer dispersion: 0.4 g anatase, 0.1 g OX50 and 0.665 g stearic acid. This allowed for the evaluation of the titanium concentration directly onto coating properties first prior to evaluating other factors. The wetting behaviour, chemical composition and morphology of two of the coatings are presented in **Figure 3.7**.

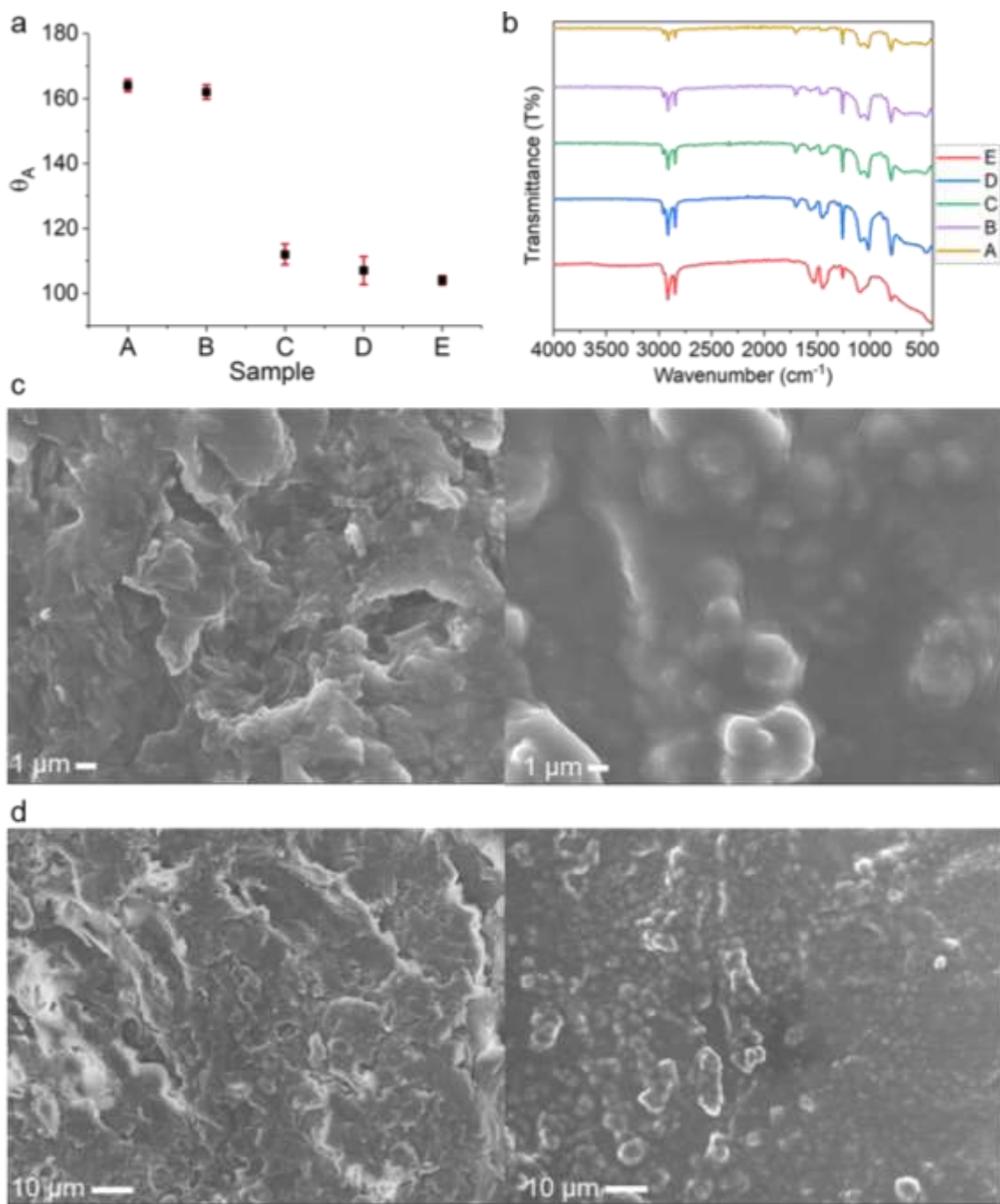


Figure 3.7 Characterisation of samples **A - E** (a) Contact angle measurements (b) ATR-FTIR chemical analysis (c) and (d) SEM images of samples **A** and **E** at two different magnifications.

The first distinct trend noted in the wetting behaviour measured using advancing contact angle (θ_A), as seen in **Figure 3.7a**, showed superhydrophobic

behaviour reaching θ_A of 163° and 162° respectively for samples **A** and **B**. This follows the trend seen in analysis of the polymers themselves, as seen in Figure 3.4a. The trend of decreasing θ_A follows through to samples **C** – **E** which remain hydrophobic but below 120° despite the particle loading and carboxylic acid for reduction of surface energy remaining the same.

This suggests the presence of a critical concentration of titanium isopropoxide that can be added to the polymer network before it hinders the hydrophobic nature of the polymer. As seen through literature, titanium dioxide species are hydrophilic in nature even reaching superhydrophilicity when irradiated with external UV light.⁸ This is due to the hydroxy bonds the valent electrons around the oxygen atoms in the structure can form with water molecules.²⁷¹ The data suggests that at the higher concentrations of the metal oxide crosslinker, larger and more frequent clusters form within the polymer network (Figure 3.4c) and as such provide more sites for hydrogen bonding between the surface and the water causing a hindrance to reach superhydrophobicity (Figure 3.4a and **Figure 3.7a**).

The additional roughness along with carboxylic acid functionalisation and the hydrophobic nature of PDMS prevent the coatings becoming hydrophilic as there remains limited contact between the solid and liquid phase and the carboxylic acid continues to reduce surface energy. Furthermore, in terms of wettability, even through the use of a simple coating method of direct application, the error between data points is low – keeping within $\pm 5^\circ$ of the five point average. This indicates that the overall chemistry of the coatings is homogenous.

ATR-FTIR measurements, Figure 3.7b, of the coatings were taken to better understand the overall chemistry of the material made. To simplify the data, key regions will be focused on within the frame of analysis: Ti-O peaks corresponding to the titanium oxide species; Si-Si and Si-O peaks corresponding to the polymer (PDMS) and the silica particles used; and C regions for the carboxylic acid and the polymer – with key note on the carboxylic acid group peak.

Based on the results obtained for the polymer analysis in Figure 3.5b, the distinctive titanium peaks can be noted within the coatings themselves. For the titania species, it is crucial to separate out the anatase peaks seen from the particles used in the coating and the peaks that can be attributed to the polymer network. As such, the peak at $\sim 420\text{ cm}^{-1}$ corresponds to Ti-O in amorphous titanium oxide and the peak at 790 cm^{-1} can be attributed to the polymer network. Peaks at 550 cm^{-1} , 1640 cm^{-1} and 3400 cm^{-1} (last least pronounced to polymer coating) correspond to the anatase particles used. It is notable that the peaks in the fingerprint region become more distinguished when looking at data from sample **E** to sample **A** which can be attributed to the change in crosslinker concentration. In sample **E** the dominant peak is for the amorphous titanium oxide species whilst in other samples the anatase peaks and the other titanium species peaks can be seen. The same trend of broadening of peaks can be seen in the polymer data in **Error! Reference source not found.b**.

Further regions of Si-Si, Si-O and Si-C can be then assigned from the spectra in Figure 3.7b. The presence of the hydrocarbon C-H bond can be seen in the FTIR spectra with peaks around 2900 cm^{-1} , which are attributed to the

carboxylic acid used to reduce surface energy of the coatings and to also promote dispersion as an added function. Acid functionality can be also noted through the peaks in the region between 1600 cm^{-1} and 1000 cm^{-1} , notably peaks at $\sim 1250\text{ cm}^{-1}$ present for $-\text{COOH}$ bond for carboxylic acid. However, a key peak at $\sim 1750\text{ cm}^{-1}$ for $\text{C}=\text{O}$ bond was not seen within the analysis, suggesting the acid bonded to polymer network which would indicate the hydrocarbon chains arranged towards the surface of the coating as expected due to their hydrophobic nature in polar media, a trend also noted with surfactants (Chapter 2). Finally, the remaining peaks around 790 cm^{-1} and 1050 cm^{-1} can be noted for silica particles whilst other peaks seen for Si-C bonds among others can be attributed to the PDMS polymer.

As roughness plays another key role in understanding the wetting behaviour of the coatings produced, SEM images (Figure 3.7c-d) of two coatings with lowest and highest titanium crosslinker concentrations were taken at two magnifications to understand the nano and micro scale behaviour of the coatings. From the images, Sample **A** demonstrates two key differences to Sample **E** that work to explain such a drastic difference in contact angle measurements noted in Figure 3.7a, that is the extent of roughness and the way particles are expressed at the surface.

First, the roughness in **A** seems more complex and uniform, thus trapping more air within the structures and reducing the solid-liquid phase interactions whilst uniformity of the roughness would result in the wetting behaviour to be consistent throughout the surface. Furthermore, the anatase particles are not as directly exposed as they seem in **E**, thus the hydrophilic nature of anatase was suppressed in Sample **A**. The images of the coatings along with the ATR-FTIR

analysis help to explain the reasons behind the wetting noted from the prepared samples. Furthermore, similar trends have been noted in polymer film analysis suggesting the titanium hybridization affects a number of functions when applied to coating setting beyond just physical properties.

As such, it was crucial to understand the interaction of the polymer with various carboxylic acids at the same concentration (samples **A1 – A3**) and how anatase concentration affects the wetting (**A3 – A6**). These coatings were prepared the same way as sample **A** with the changes outlined previously. The samples were analysed as seen in Figure 3.8.

Focusing primarily on the variation in carboxylic acid functionality as expressed by samples **A1 – A3**, clear differences can be noted in the water contact angle seen in Figure 3.8a and chemical composition as seen in Figure 3.8b and c. The biggest differences can be noted between sample **A1** which was functionalised with lauric acid and samples **A2** (palmitic acid) and **A3** (stearic acid). This is due to changes in the hydrocarbon chain length responsible for the introduction of van der Waal's hinderance used to reduce surface energy of the coatings hence reducing the contact between the liquid and solid phases. This is reflected by lower contact angles and reduced count (cps) of the carbon peaks within the XPS data.

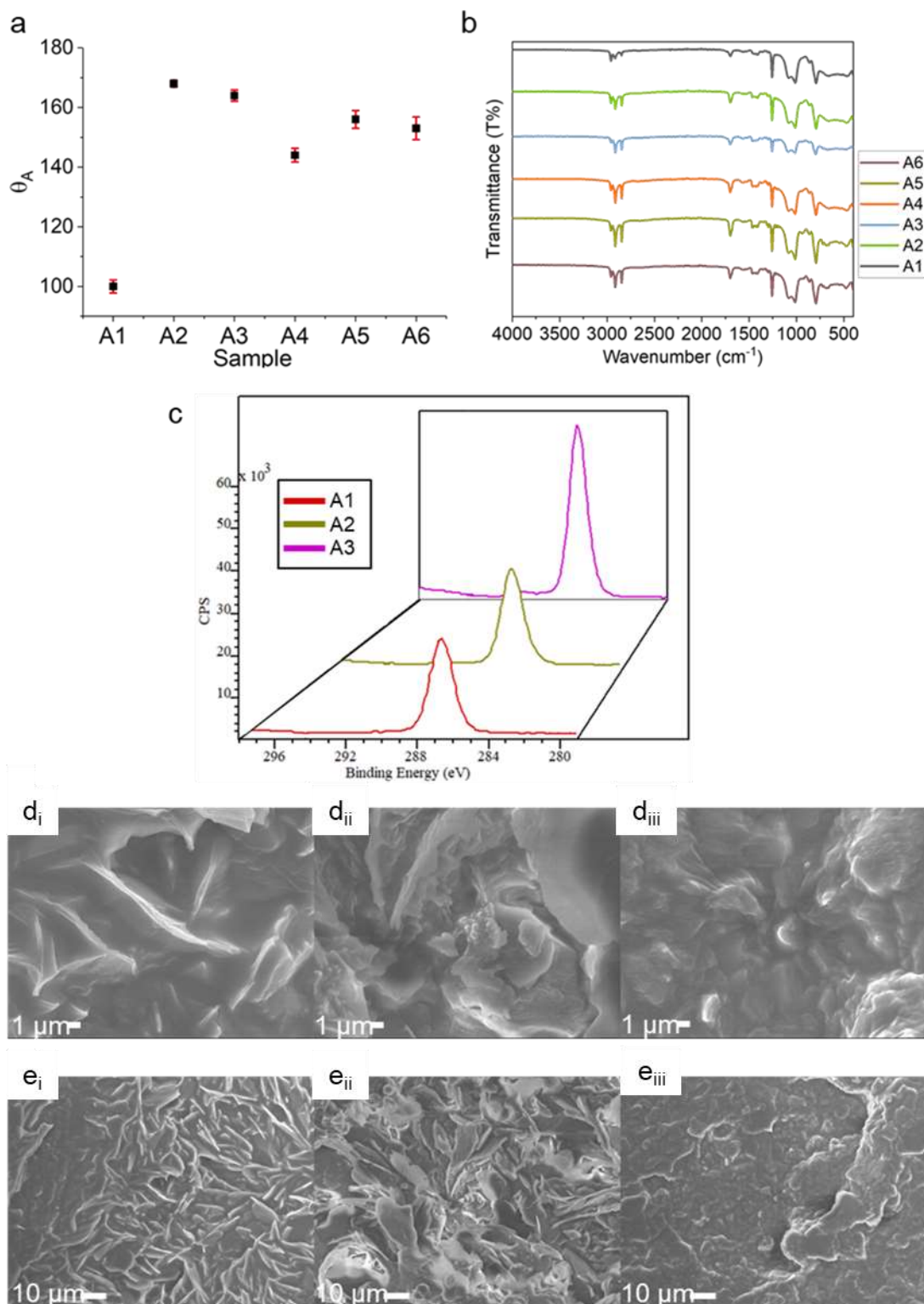


Figure 3.8 Characterisation of samples **A1 – A6** (a) Contact angle measurements (b) ATR-FTIR chemical analysis (c) Carbon XPS elemental analysis of samples **A1 – A3** (d_{i-iii}) and (e_{i-iii}) SEM images of samples **A4 – A6** at two different magnifications respectively.

Considering the wetting behaviour in Figure 3.8a, there was a large increase in water contact angle between the twelve carbon chain of the lauric acid (sample **A1**) at $99.5^\circ \pm 2.2^\circ$ and the sixteen carbon chain lengths of the palmitic acid (sample **A2**) reaching $168.4^\circ \pm 1.1^\circ$ and the eighteen length of the stearic acid (sample **A3**) reaching $164.4^\circ \pm 1.9^\circ$ respectively. This leads to the conclusion that when combined with the roughness (kept constant through control of the other parameters such as particle loading), the surface energy was not thoroughly reduced by the lauric acid.

Furthermore, the effect of the chain was expressed due to the molar concentrations used in the fabrication were kept at 2.3×10^{-3} mol as such the direct impact of increasing chain length was observed. This was also confirmed through composition analysis of the coatings as seen in the FTIR (Figure 3.8b) peaks at around 2900 cm^{-1} (C-H peak) and the carbon XPS counts (Figure 3.8c) increasing with increased chain length on the acid.

Examining the impact of particle concentration on the wetting behaviour of the coatings, Figure 3.8a, two key findings can be noted: 1. The overall trend follows that the reduction of particle concentration reduces contact angle and 2. A loss of superhydrophobicity can be noted in sample **A4** with 0.3 g of anatase. The first finding follows known coating behaviour as the roughness was reduced due to lower particle concentration, it was expected to see a reduction in contact angle and an increase in the error due to higher irregularities in the surface roughness. The second finding is harder to define the cause of such a drop in wetting behaviour followed by a rise when the particle loading was further reduced.

To better understand the findings from contact angle measurements, SEM imaging was done, as seen in Figure 3.8d-e at two magnifications for samples **A4** – **A6**. SEM image for **A3** can be noted in Figure 3.7c-d due to the nature of the composition of coating **A** and **A3** being identical. From the images, sample **A4** can be noted to have a different morphology arrangement compared to the other samples. Especially when looking at the larger microstructures seen in the 10 μm scale images. This would explain the loss of superhydrophobic properties due to the coating presenting a smoother surfaces meaning less air being trapped within the surface morphology thus increasing contact between the liquid and solid phases.

The study of the variation to the composition of the titanium crosslinked hydroxy terminated PDMS confirmed sample **A** (also referred to as sample **A3** in Figure 3.8) as the optimal coating due to high contact angle resulting from the stearic acid functionalisation and the morphology obtained as seen by the SEM images.

To evaluate the crosslinking in further applications, titanium crosslinking was conducted in non-polar system in samples **F** and **G** with Sylgard 184 as the source of PDMS and compared to standard crosslinking process for this polymer in sample **H** as shown in Figure 3.9. The samples were evaluated based on the wetting behaviour (Figure 3.9a), chemical composition by FTIR analysis (Figure 3.9b) and morphology through SEM imaging in Figure 3.9c-d.

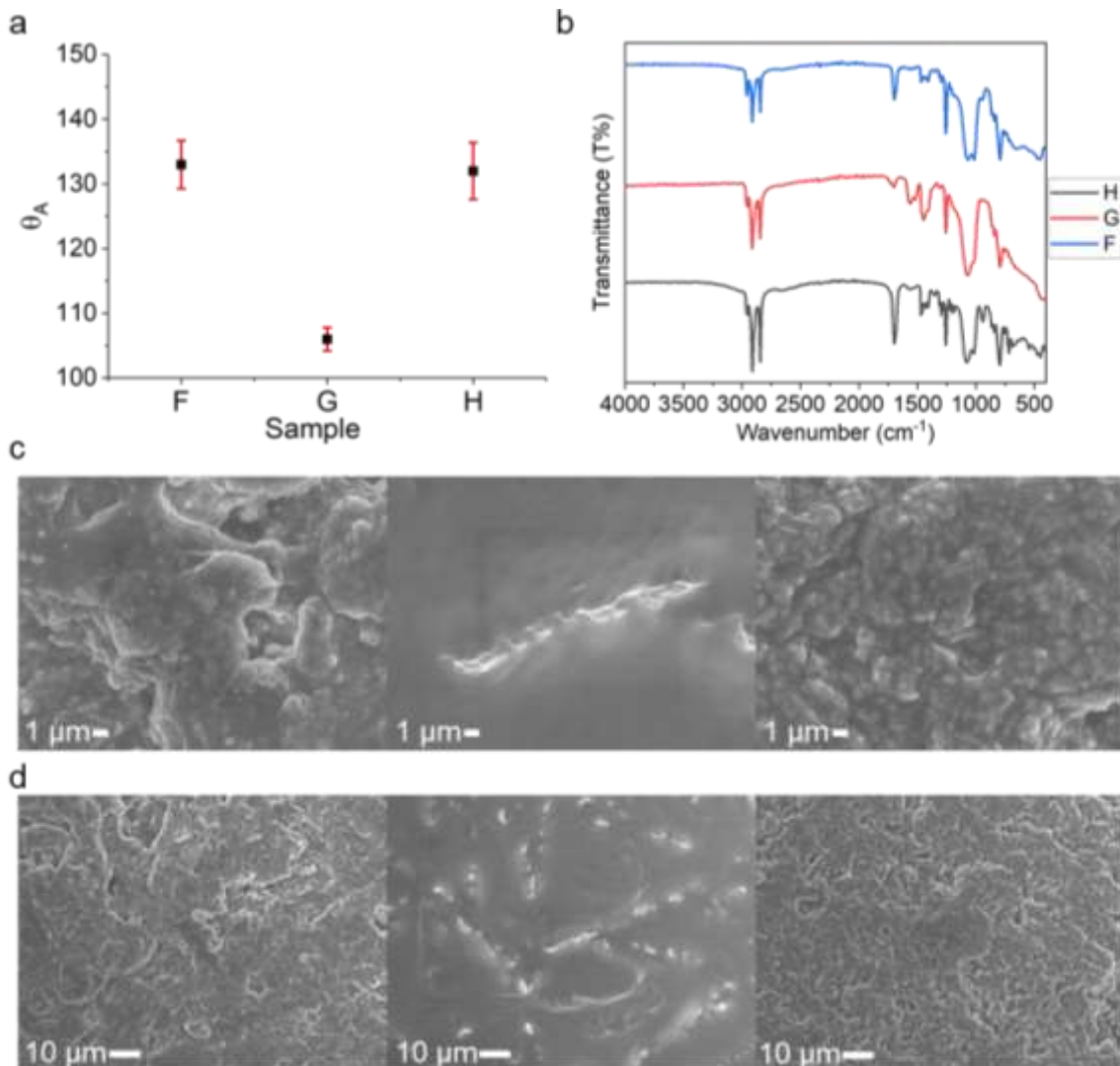


Figure 3.9 Characterisation of samples **F** – **H** (a) Contact angle measurements (b) ATR-FTIR chemical analysis (c) and (d) SEM images of samples at two different magnifications.

Despite none of the coatings crosslinked with titanium reaching superhydrophobicity in this study (Figure 3.9a) a number of key findings have been found to better understand the process and improve future work discussed later in Chapter 4 of this thesis. Firstly, the θ_A of sample **F** (10 : 1 ratio between titanium and PDMS) and sample **H** are both within the same region of 132°. This indicates that the crosslinking at this concentration results in a polymer

with similar properties in terms of wetting, indicating that the hybrid approach can be applied for similar uses. Furthermore, similar trend to the one noted in Figure 3.7a between samples **A** and **E** can be seen in Figure 3.9a between samples **F** and **G**, where the increased titanium concentration results in a drop in wetting behaviour. This means that the hypothesis presented by the evaluation of the data holds true and the increased concentration causes an increase in hydroxy sites that cause an increase in hydrophilic sites within the polymer network.

This is further supported by the morphology analysis seen in Figure 3.9c-d where the morphology between samples **F** and **H** seems similar in roughness at both the nano and micro scales whilst the roughness of sample **G** can be seen to be smoother. When considering the data obtained in Figure 3.7c-d, the increased concentration of the titanium species reduces the flexibility of the PDMS causing the roughness obtained by the particles to be suppressed as the polymer is less likely to envelop around the particles but instead pushes them below the surface.

Overall, the characterisation of the coatings, through variation of surface reducing agents, particle concentration and polymer type indicate the hybridization of the PDMS polymer with titanium species can form superhydrophobic coatings in hydrophilic media whilst resulting in similar properties to standard crosslinking when done under organic conditions. This allows for the hybrid polymer to find applications within both systems with higher preference towards water based fabrication, which in turn would facilitate the use of particles typically requiring prior functionalization to achieve good dispersion and superhydrophobicity.

3.4.3 UV stability study

To understand the impact of the titanium crosslinking on the stability of the coatings, samples **A**, **C**, **E** and **H** were placed in a UV-A chamber for 21 days. The samples were analysed using FTIR to track changes to the chemical composition caused by degradation from the anatase. Impact on the wetting properties of the coatings was measured using contact angle measurements at the same intervals to assess the stability and to see if transition between superhydrophobicity and superhydrophilicity can be noted in the hybrids. The data was plotted and presented in **Figure 3.10** with an image of the coating before and after the exposure experiment, as seen in **Figure 3.10f**.

From the FTIR chemical analysis seen in **Figure 3.10a-d** (key found in **Figure 3.10e**) there is little to no differences for most of the samples between day 1 and day 21 of the experiment. There is a steady decrease in the intensity of the peaks at $\sim 2900\text{ cm}^{-1}$ for the C-H bond which corresponds to the hydrocarbon chains of the carboxylic acid used to functionalise the coatings. This indicates that the acid functionality was being degraded by the anatase during the 21 days of exposure to the UV light. The weakest change can be noted for sample **A** which indicates the small amount of the titanium used for crosslinking of the PDMS was actually stabilising the coating, thus the stability of sample **A** is seen as high. Further changes to a number of the coatings can be seen with visual discolouration of the coating as seen in **Figure 3.10f_i** for before irradiation and **Figure 3.10f_{ii}** after exposure to UV for 21 days. This yellowing of the coating is common with anatase based materials as the polymer is degrading which can

be also noted in the fingerprint region of the FTIR data for most samples through the loss of distinctive peaks.

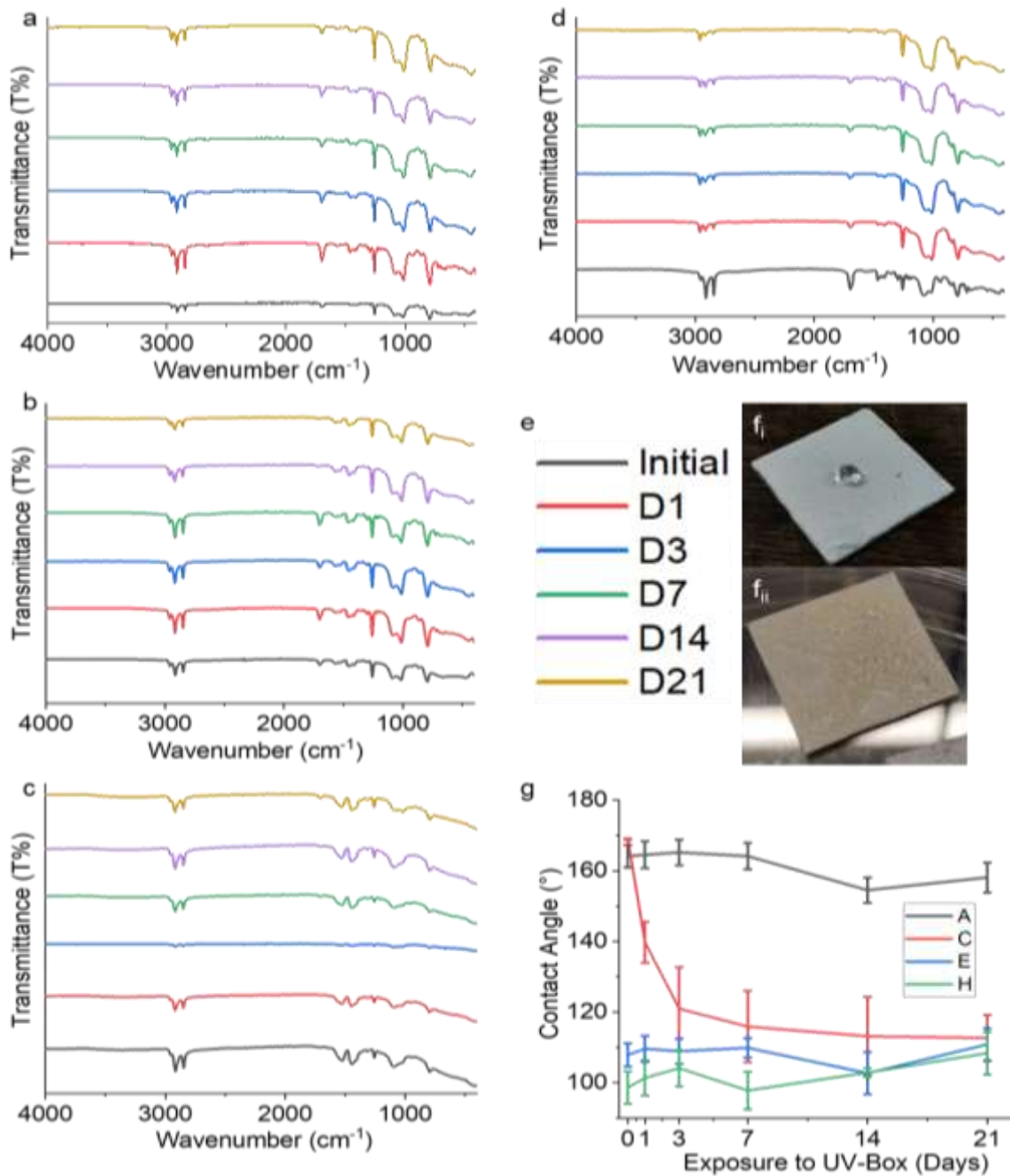


Figure 3.10 UV exposure study on the effect of titanium crosslinker on the stability of the coating over duration of 21 days as analysed by (a-d) ATR-FTIR for each sample in order **A**, **C**, **E**, and **H** respectively (e) key for FTIR graphs (f) Image of the coating before and after exposure and (g) Contact angle measurements.

Over the duration of the experiment, only sample **C** demonstrated a drastic change in wetting behaviour whilst the other samples remained stable. When considering samples **E** and **H**, **Figure 3.10g**, the wetting behaviour of the two samples followed the same trend of a small increase to the measured contact angle up to $\sim 115^\circ$. In contrast sample **C** decreases from $\sim 168^\circ$ to $\sim 115^\circ$ completely losing superhydrophobic behaviour after day 1. However, sample **A** remained superhydrophobic throughout the duration of the experiment. This confirms the findings from the chemical analysis on the UV stability of the coatings.

3.4 Conclusion

Successful fabrication of titanium-PDMS hybrids was demonstrated with increasing metal oxide concentration following a modified process discussed by Dalod et al.⁷ The effect of the increase was studied using contact angle measurements and UV transmittance showing the resulting polymers exhibit similar properties to that Sylgard 184 in terms of contact angle remaining hydrophobic and transparency in the visible region above 85% compared to glass at 90%.¹⁹⁷ However, the higher concentrations of the hybrid do become more brittle meaning the polymer loses its elastic properties as noted within the work of Dalod et al.,⁷ who discussed similar effects at the higher range of the concentrations of TTIP used in his research. The chemical analysis confirmed that increasing titanium crosslinker causes an increase in metal oxide pocket size as the lower concentration was shown to fully crosslink the hydroxy terminated PDMS due to the lack of a hydroxy (O-H) peaks above 3000cm^{-1} .

Applying the hybrid polymer into a coating has also been demonstrated to follow similar trends in terms of wettability to that of the polymers with decreasing contact angle upon increase in metal oxide crosslinker. Further variations in composition such as particle concentration and surface energy reducing agent have both been studied. Varying the acid used to functionalise the coatings has been shown to greatly impact wettability with lauric acid showing contact angle below superhydrophobicity regime due to the short hydrocarbon chains. The effect of the hydrocarbon chains has been shown to result in low surface energy materials but often required branching of the acid group to achieve this.²⁹⁵ Here we show that the increased hydrocarbon chain length achieves the same result. Particle loading concentration has been shown to minimally affect the wetting of the coatings.

Further comparison to non-polar solvent crosslinking of Sylgard 184 was conducted to compare the behaviour of the alcohol crosslinked polymers as well as evaluate the applicability of the technique to other solvent systems. The analysis revealed that the resulting coatings failed to reach superhydrophobic behaviour however the titanium crosslinking at 10 : 1 ratio yielded a material with similar properties compared to that of the standard Sylgard 184 crosslinking with platinum catalyst. This results in an application of the polymer for the purpose of liquid repelling with additional functionality of the titania group within the polymeric chain as introduced by Dalod et al.⁷

Ultra-violet stability study was done to assess the impact of the titanium crosslinker on the wetting and chemical composition of the anatase based composite coatings after prolonged exposure to UV light. The data demonstrated high stability of sample **A** which contained the lowest amount of

titanium in the polymer network. Coating **C** degraded the most in terms of wettability, losing superwetting behaviour after one day of irradiation. Yellowing of the samples **C**, **E** and **H** was seen at the end of the experiment which is indicative of the polymer being degraded by the anatase as confirmed by FTIR analysis with the loss of peak definition and intensity. This study showed that the prepared coating has potential of high durability to the environment though further testing of the sample to other factors such as icing and weather cycles is needed to confirm this.

Chapter 4

Assessing coating

methods for non-polar

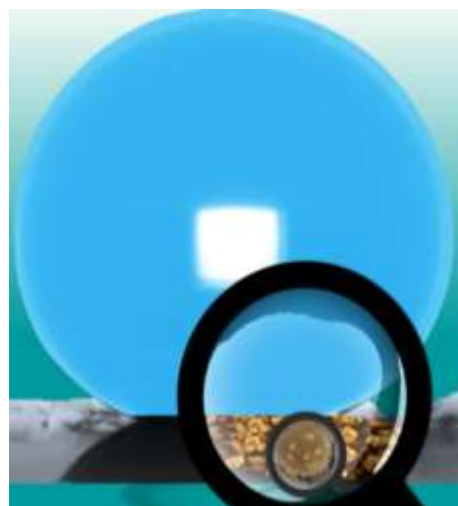
solvent based scalable

fabrication of transparent

and fluorine-free

superhydrophobic

nanocomposite coatings



4.1 Introduction

In recent decades, superhydrophobic surfaces have found many applications including self-cleaning surfaces,¹ reduction of drag,² anti-icing,^{3,4} self-healing⁵ and various other areas.⁶ This has been the main drive towards optimising and facilitating their fabrication through the use of a wide array of polymers,^{1,94,105,249–251} particles^{96,296} and coating methods.^{8,85,111} However, often the crucial component of these surfaces is the attainment of low surface energy through functionalising the material with either silanes (fluorinated or non-fluorinated) or organic molecules such as carboxylic acids. These functionalities

facilitate liquid repulsion, for example water contact angle needs to be $>150^\circ$ where the droplet can pin on the surface in Wenzel state³⁰ or roll off the surface in Cassie-Baxter state³¹ depending on the desired applications. For self-cleaning, liquid mobility and drag reduction applications require Cassie-Baxter with non-uniform roughness.

The droplet on Cassie-Baxter surfaces is mobile due to contact angle hysteresis previously discussed in Chapter 1.⁴⁶ The physical basis of contact angle hysteresis (θ_Δ) is still unclear, however studies indicate that the phenomenon occurs due to non-ideal properties of real surfaces resulting in several metastable states or thermodynamically stable contact angles.^{8,42,57}

The choices of functionalizing material has been thoroughly discussed in Chapter 1, however it is crucial to remember that fluorinated silanes have a stronger ability to cause surfaces to become superhydrophobic. This is because stable fluorinated groups decrease the van der Waal's potential more than other hydrocarbon functionalities with the resulting electrostatic interactions limiting contact between the solid and liquid phases.⁶⁷ This often results in higher transparency of the coating material as lower roughness and particle loading is required to achieve similar results. But the major drawback of utilizing fluorinated groups is the environmental impact of production and use of such materials which is leading the ban on their use.^{71-73,76,77} This has led use of alternative materials for reducing the surface energy in order to reach contact angles $>150^\circ$.^{1,5,126,128} Fluorinated silanes are often successfully substituted for long chain hydrocarbon groups,^{118,130} as these inhibit water-solid interactions through only van der Waal's potential created by the hydrocarbon chain interactions.

Structured and porous silica has been shown by literature to a great extent with success in transparency, durability and self-cleaning.^{85,297,306,298–305} However, their application within deposition systems has been limited due to difficulty of achieving homogenous dispersions in polymeric solutions. This is predominantly the result of particle synthesis being conducted in hydrophilic media whilst a vast array of polymers have better solubility or a greater extent of swelling in organic solvents. For that reason, many publications choose to utilize a sol-gel route where precursors are mixed with the polymer and then deposited onto substrates where particle growth occurs creating the required surface roughness.^{85,92,307,308} However, this approach greatly limits the capability to tailor particle morphology and functionality which *ex situ* approaches provide. For example, using mesoporous particles permit the polymer to fill them which have been shown to benefit the homogeneity of the coating composite resulting in higher transparency, whilst the added roughness to the particle provides hierarchal structures that result in greater contact angles at lower concentrations.^{8,309}

Polydimethylsiloxane (PDMS) has been extensively studied for the use in superhydrophobic coatings^{94,249–251} because of its hydrophobic nature as well as transparency when cured even at large thicknesses. The homogenous nature of the polymer and ease of use make it a good choice for scaling and facilitating the production process. However, due to the minimal interacting sites, the polymer has poor adhesive properties to glass, often requiring additional treatment of glass with plasma or chemical activation to increase hydroxylation which can be either costly; temporary or hazardous to health with the example of Piranha solution treatment.

To address this concern, an *in situ* sol-gel approach to bridge PDMS monomers with metal oxides was adopted in this work.^{7,261} Metal alkoxides, such as titanium tetra(isopropoxide) [Ti(OⁱPr)₄] (TTIP), can be used to form titanium oxide linkages within the polymer network without impacting on its stability due to the low concentration within the system.¹⁴³ Furthermore, the adhesion between the hybrid polymer and glass substrate is enhanced due to the hydrolysis reaction between the transition metal (titanium) and free oxide species on the glass forming irreversible Ti-O-Si bonding.⁸

4.1.1 Formulating stable nanocomposites for non-polar solvent coatings

Polar solvents such as water or alcohols (ethanol/ isopropanol) have unique properties for wet-chemistry synthesis of nanoparticles such as silica (SiO₂),^{187,204,211,214,310} titania (TiO₂)^{311,312} or zinc oxide (ZnO).^{313–315} Due to the alkoxide nature of the precursors for these, they often prove difficult to fabricate in nonpolar (organic) environments. Additionally, using polar preparation techniques have capability to utilize structure determining template molecules such as surfactants resulting in various particle morphologies such as nanospheres,^{192,208,316} hollow spheres,²³³ nanorods^{192,208,223,238} and many others with possibilities to achieve these with noble metals as well as transition metals.^{187,237,317} This can be achieved due to high control over kinetics of growth of the particles, solubility of the templates and thermodynamics of the reaction routes. Reaction routes such as sol-gel or Stöber method require water or alcohol for the condensation of the metal alkoxide such as tetraethyl orthosilicate (TEOS) into silica nanospheres.^{187,204,205,230,318}

Due to continuous developments in the synthesis of hydrophilic particles, a vast array of applications for these have been demonstrated in diverse fields such as sensors, catalysts, optics, coatings and biomedicine.^{192,199,212,230,234,318–321} However, many of these applications benefit from dispersion of the particles in organic solvents especially in the fields of polymeric coatings, organic catalysts and optoelectronics.^{62,96,194,296,317,322} This produces the necessity for formulating stable dispersions of the hydrophilic nanoparticles originally synthesized in polar media in nonpolar solvents which often requires surface modification or suitable introduction of depletants so that these particles can homogeneously mix within aprotic or nonpolar solvents.

Nanocomposites typically consist of nanoparticle and polymer suspensions in compatible solvents allowing for a facile surface modification. The formation and use of such materials has been thoroughly reviewed elsewhere.^{6,296} However, the key factors that impact nanocomposite formulations are stability, miscibility and homogeneity. These are crucial in fabricating coatings with uniform roughness whilst expressing desired properties. Of the many approaches of achieving stable colloidal dispersions, transferring the phase of the hydrophilic nanoparticles to hydrophobic solvents has been achieved by surface modification. Ligand exchange is the most often utilized to accomplish this especially with noble metal particles,^{18–20} while silanization is frequently used with silica-based particles due to the ease of the reaction.^{13,17,197,221,230,235,320,323–325} These processes successfully modify the wetting behaviour of the particles without the need to change the composition of the colloid with further additives such as other particles or polymers that cause steric hinderance.²¹ To that extent many ligand exchange and silanization

processes have been developed with some more facile than other depending on the particle type or organofunctional alkoxysilane used.

There have been several reports of PDMS-silica nanocomposites used for fabrication of superhydrophobic coatings.^{169,297} This is because the polymer and particle work well together in terms of transparency due to the physical properties of the PDMS whilst the silica particles have easily accessible environments for further functionalisation and morphologies as discussed in Chapter 2. Furthermore, functionalised silica is easily dispersed in solvent diluted PDMS with good stability resulting in uniform coatings. Alternative formulations also have been reported such as by Yang et al.³²⁶ through suspending fluorinated graphene sheets in epoxy or Luo et al.²⁵⁷ using polyvinylidene fluoride (PVDF) particles in PDMS with KH-550 which is an amine terminated silane.

4.1.2 Understanding the principles of optical properties of particle roughened surface modifications

Optical properties of the polymer, particle and the solvent used in the fabrication of nanocomposite affect the resulting transparency of the coating. The key aspects dictating this are absorbance, transmittance and reflectance, however key measurements of the refractive index, light transmission and scattering enable to optimise nanocomposites for transparency in the selected optical window.^{300,327} Close match between the individual aspects of these properties between the constituents of the composite result in uniform expression of transparency throughout the coating. In nanocomposites several factors affect the optics of a material including particle size and morphology; polymers innate

properties and their match to the particle; as well as solvent properties that contribute in the dilution and dispersion of the composite.^{300,327} This section focuses on how each of the refractive index, light transmission and scattering is measured and how choosing the components of the nanocomposite was done for this project to target transparency in the visible light region.

The index of refraction is better defined as the ratio of the velocity of light in air compared to that in the examined media.³²⁸ The refractive index plays a key role in many applications such as thin-film coatings, fibre optics and many more.³²⁹ It is measured by a number of techniques with ellipsometry as an example. There is a dual aspect to the index as it consists of both the real (n) and imaginary (k) parts. With complex derivations from the Maxwell equations discussed elsewhere, as well as the Beer-Lambert laws and Fresnel equations, each technique used to measure the refractive index measures the amount of light that is absorbed, transmitted and reflected and software process the data obtained.³²⁸

Majority of polymers show refractive index in the range of 1.4 to 1.6 in the visible region with material such as polydimethylsioxane (PDMS) having a refractive index of 1.41 to 1.42 in the wavelengths of 700 - 400 nm.^{329,330} This is why PDMS can be found used in manufacture of many photonic elements such as lenses and optical fibres to name a few.³³¹

Applications for liquid repelling surfaces such as smart windows, solar panel or package wrapping, often require the coated surface to remain translucent or even transparent.^{332,333} The key challenge in fabricating transparent superhydrophobic coatings is the conflicting requirements for transparency and

roughness of the material. Many coatings have been developed using a variety of materials and fabrication approaches^{300,327,332} which resulted in high transparency of the end material, however the common approach to achieve this was done using particle size below 100 nm in polar solvents whilst functionalisation was needed when nonpolar solvent was used to enhance stability and deminish the effect of agglomeration^{300,327}.

There are two types of scattering of light by a particle Rayleigh and Mie scattering, as illustrated in Figure 4.1.^{334,335} Both occur when a wave of light hits a particle which is then in turn scattered by it. Theoretical computation³³⁶ hypothesised that Mie scattering has exponential increase with increasing surface roughness, demonstrating significant reduction in optical transparency and is the dominant factor in coating design.

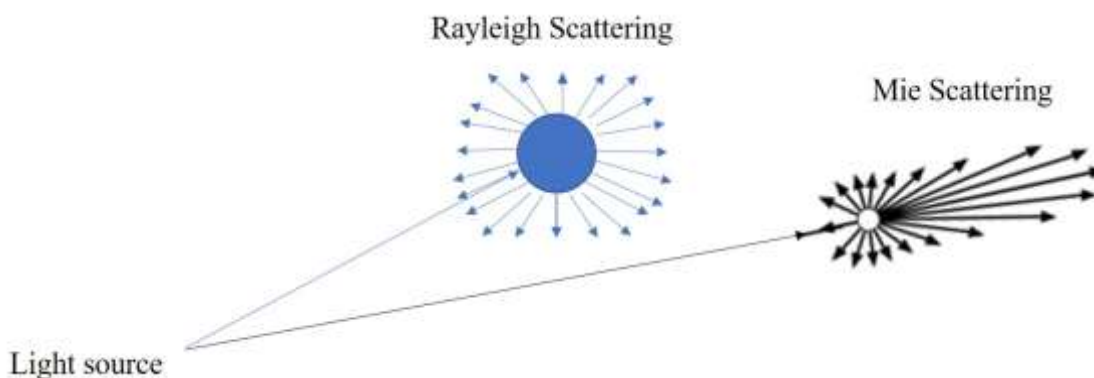


Figure 4.1 Visual representation of Rayleigh and Mie Scattering

In the case of Rayleigh scattering, it is caused by the electromagnetic wave of light interacts with a particle much smaller than the wavelength creating an oscillating dipole meaning electrons move back and forth. The resulting radiation at the same frequency as the incident radiation however different particles scatter with different efficiencies due to the electron availability and

bounding to the particle. For Mie scattering, the particle is larger than the wavelength of the irradiating light and is proportional to the square of particle diameter. Mie scattering is stronger than Rayleigh scattering which is why smaller particles that are better dispersed in the media result in lower scattering. Typically, particles below 100 nm are used for transparent coatings with indication that this can be extended to particles below 150 nm when monodispersed and refractive index are matched with the polymer.

Scattering can be measured through several techniques with Haze and clarity showing applicability in the design of transparent coating on glass. Haze measurements allow for a standardised evaluation of any coating based on the angle of scattering by the coating compared to untreated glass with set boundaries defining transparency based on scattering. The extent of scatter can be then converted alongside of light transmission to achieve a percentage clarity of the coating which evaluates both the extent of transparency close to the coating as well as at a distance.

4.2 Chapter outlook

In this chapter, three coating approaches were applied in fabrication of transparent fluorine-free superhydrophobic coatings. First, spray coating was used to assess optimal sonication times for the dispersion of particles using RX300 fumed silica in organic solvent with Sylgard 184 PDMS as polymer. Three sonication times were selected and evaluated using contact angle and photon transmission for functionality evaluation and atomic force microscopy (AFM) for morphology analysis. Once the optimal sonication time was selected, particle loading concentration, morphology and functionality study was

conducted using both the RX300 fumed silica and the particles synthesized in Chapter 2. Finally, crosslinking of PDMS with titanium dioxide applicability to coatings was assessed using RX300 as main particle for the spray coating method.

With the success obtained from spray coating, two further methods were evaluated in terms of fabricating durable and transparent superhydrophobic coatings. The work compared aerosol assisted chemical vapour deposition (AACVD) and spin coating as both demonstrate scalability whilst differing significantly from spray coating. The aerosol deposition was conducted on heated glass substrate which was theorised to better improve durability of the resulting coatings as the heat was expected to improve the initial reaction of the titanium species causing bond formation between the glass and the crosslinker forming Ti-O-Si bonds within both the polymer and with the substrate. The spin coating and the spray coating rely on curing the sample post application which delays the possible interactions between the metal and the glass which is theorised to limit the interaction sites hence not having a great impact on the durability of the final material.

Considering the spin coating and AACVD, the resulting coatings from both methods demonstrated a high degree of transparency whilst AACVD significantly reduced the particle loading concentrations (9 wt% compared to 41 wt% for spin coating) to achieve superhydrophobicity. Both methods relied on fluorine-free silanization, however AACVD samples exhibited nano-micro hierarchical roughness which was less homogeneously expressed by the spin coating approach.

Overall, this chapter presents a number of new findings. Firstly, the introduction of metal oxide crosslinking of PDMS for coating applications which in recent years has been gaining interest for the preparation of hybrid inorganic-organic polymer networks and has been demonstrated here to be feasible in nonpolar solvents. In this chapter, the metal oxide species has been proven to enhance durability of the superhydrophobic coatings where the conditions in AACVD demonstrated adhesion resistance of up to 15 tape test cycles and up to 25 sand paper abrasion cycles without highly impacting the transparency of the polymer. This work was the first report of such improvement in hybrid inorganic-organic superhydrophobic PDMS nanocomposite.

Second, the use of AACVD showed a large decrease in concentration of particles required for superhydrophobicity (down to 9 wt% to polymer compared to 41 wt% for spin coating or 23 wt% for spray coating) which is comparative to fluorinated examples of coatings prepared by the method. Third, the use of nanoparticles prepared *ex situ* discussed in Chapter 2, permits the tailoring of the particle roughness at the nanoscale through highly controllable synthesis routes and provides the opportunity to further functionalise the particles prior to coating to enhance utility within the nanocomposite.

Lastly, comparison of the fabrication methods further reveals the advantages and limitations in fabrication of the coatings. Using the same nanocomposite composition for AACVD and spin coating allows for direct comparison of the methods, clearly for both, indicating the benefits of one over the other.

4.3 Experimental

4.3.1 Materials

Sylgard 184 (PDMS) with curing agent (Dow, UK) was obtained as the polymer used for the fabrication of transparent superhydrophobic coatings described in this chapter. Titanium Isopropoxide (TTIP) ($\geq 98\%$, Merck) was obtained to be used as the inorganic crosslinking agent for alternative crosslinking of the Sylgard 184 (PDMS). Trimethoxy(octadecyl)silane (TMODS) ($\geq 98\%$, Merck) and acetic acid (AC) ($\geq 99.7\%$, Merck) were used to enhance the hydrophobic nature of the formulated coatings that were dispersed in toluene (Merck) as solvent. For the initial evaluation of the formulation, Aerosil[®] RX300 (Evonik, USA) was purchased due to the hydrophobic functionality of the fumed silica particles along with the small (reported around 7 nm) size of the particles.

4.3.2 Nanocomposite synthesis

A one-pot approach for the preparation of the polymer-nanocomposite was designed to simplify the coating step.^{7,96} The overall process has been outlined in Figure 4.2. In brief, the polymer of choice, either Sylgard 184 or the PDMS-OH was crosslinked with titanium isopropoxide or crosslinking agent provided by Dow as described in Chapter 3.3 in 20 mL toluene as solvent. To this a pre-determined concentration of the silica particles was added with 0.3 g acetic acid and 0.15 g TMODS followed by sonication for 60 minutes in cold water bath to minimise the effect of temperature increase from the process. The colloidal suspension was then left to stir at 750 rpm for 60 minutes at room temperature

to promote homogeneity of the coating. This coating was the utilized by all three application methods described next.

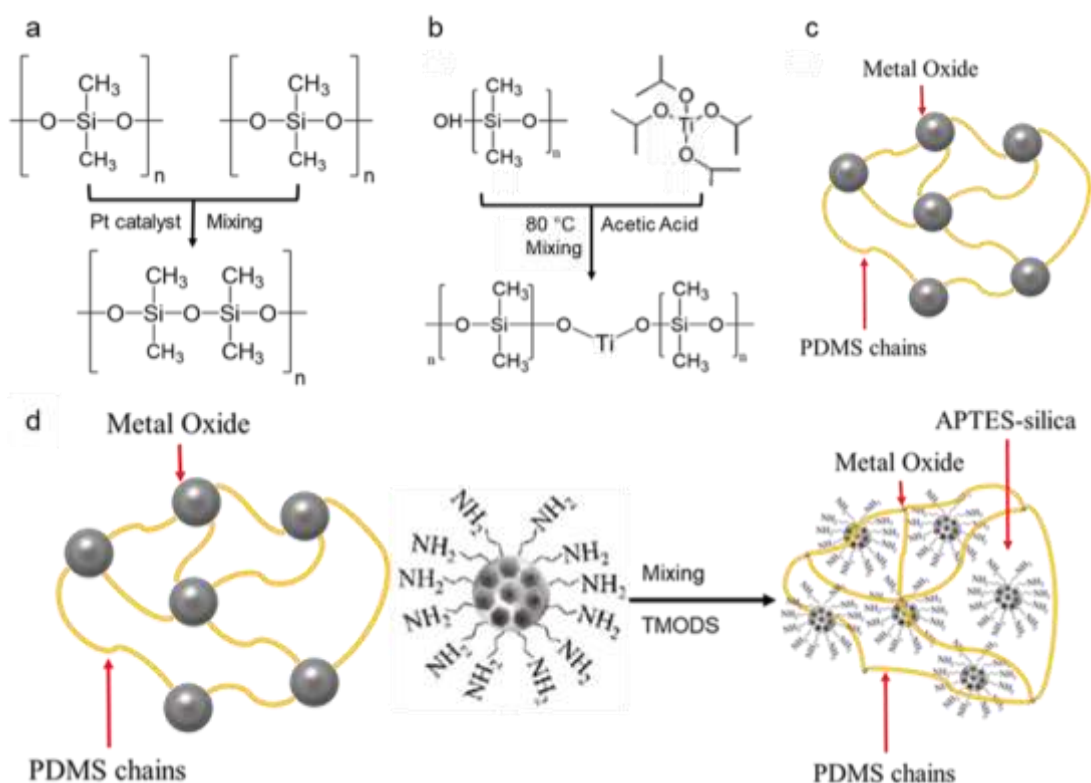


Figure 4.2 (a) Preparation of Sylgard 184 (b) Preparation of TiO-PDMS hybrid (c) diagram representation of the hybrid PDMS and (d) formation of the nanocomposite.

4.3.3 Spray Coating

The suspension was spray coated onto the selected substrate using a spray gun with a 0.5 mm nozzle, 3 barr nitrogen pressure and vertical spray-cone with the distance between the sample and spray gun being kept at 30 cm away. The substrate was coated with pre-determined number of spray passes typically followed by curing on a hot plate. The sample was left to cool and full characterisation of surface morphology and wettability followed.

4.3.4 Spin Coating

Glass substrates were spin coated using Laurell WS-650-23B spin coater with a 1 mL of suspension of the nanocomposite in toluene at 4500 rpm for 60 seconds where the addition was done once the substrate reached maximum speed using a single 1 mL pipette. This followed curing on a hot pate at 200 °C for 30 minutes. The sample was left to cool and full characterization of surface morphology and wettability followed.

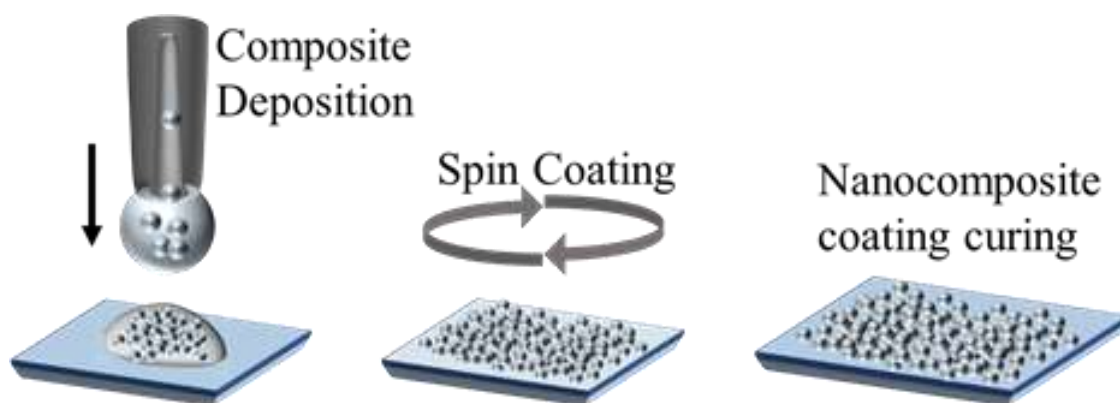


Figure 4.3 Schematic illustrations of our Spin coating procedure.

4.3.5 Aerosol Assisted Chemical Vapour Deposition (AACVD)

The APTES functionalised mesoporous silica and PDMS/Ti nanocomposite was also used for AACVD. The AACVD experiments involved depositions using a cold-walled horizontal-bed CVD reactor described previously.⁸⁰⁻⁸² For these depositions, the reactor was assembled such that the carbon heating block was positioned above a plate (145 mm x 45 mm x 4 mm) which supported the glass substrate 5 mm below and parallel to the carbon block. This resulted in a top-down heating configuration. This assembly was then enclosed within a quartz tube. Once the set reactor temperature (200, 300 or 400 °C) was reached, a PIFCO ultrasonic humidifier (power 1/4 25 W, frequency 1/4 40 kHz) was used

to form a precursor aerosol from 20 mL of composite, which was transported to the heated substrate using nitrogen carrier gas (1 L/min). Depositions were carried out for various durations (15-70 min) following which time the coated substrates were cooled under nitrogen and handled in air. The temperature, deposition time and particle concentration were varied to test the effect of these on surface morphology as well as optical transparency of the resulting material.

4.3.6 Curing

In these samples, curing (Figure 4.4) refers to the process of heating the deposited nanocomposite to promote the crosslinking of the silicone with the metal oxide (Figure 4.2) and to promote the bonding between metal oxide sites to the glass substrate. The initial heat treatment in spin coated samples works to form the bonds between the monomers and the metal oxide crosslinker resulting in the hybrid polymer network and also to promote the composite to adhere to the glass substrate through giving the reaction energy to form bonds between the metal oxide sites and glass substrates which in theory enhances adhesion of the coating to the glass.

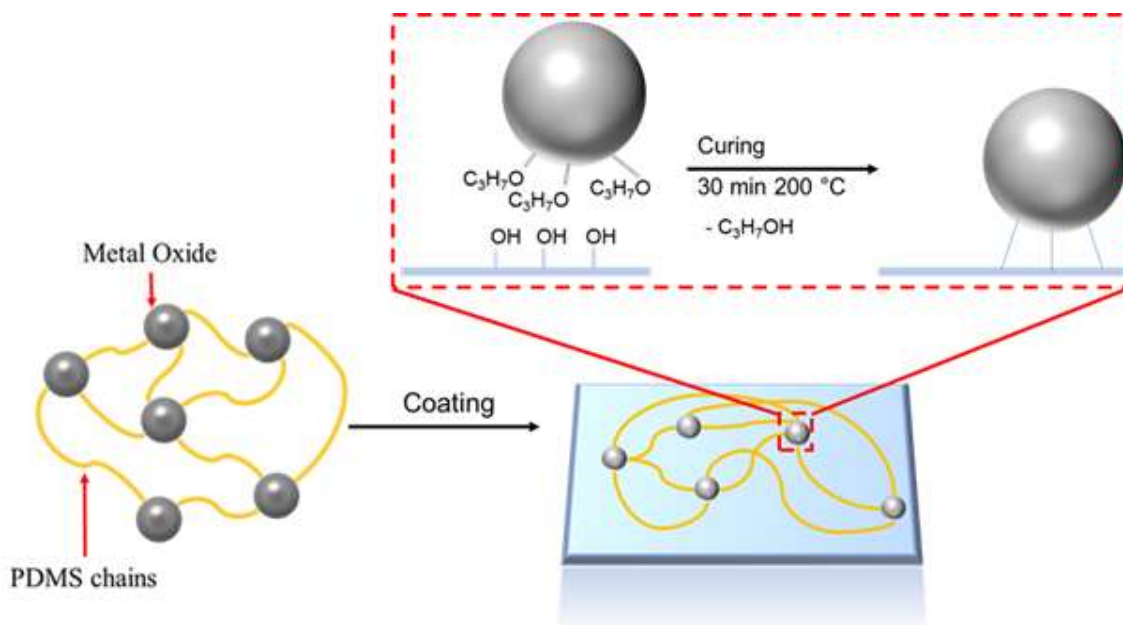


Figure 4.4 Curing process demonstrating the reaction between the metal oxide sites and glass substrate. Silica particles were not shown in this diagram for clarity.⁸

4.3.7 Characterization

ATR-FTIR measurements were taken using MIRacle™ single reflection horizontal ATR accessory with a ZnSe single reflection crystal plate. The analysis was done in the range of 400 to 4000 cm^{-1} and data obtained was plotted in Origin software. XPS was performed by Thermo theta probe spectrometer under the base pressure of 5×10^{-10} mbar using the monochromatic Al K- α photoelectron spectrometer with photon energy 1486.6 eV. Surface morphology of the samples was observed using SEM. Images were obtained using JEOL JSM-IT100. To prevent charging, samples were gold-sputtered with SC7620 mini sputter coater. The SEM images for morphologies of AACVD superhydrophobic coatings were generated under the JSM-7600F Field Emission SEM, JEOL, Japan. Vacuum sputtering samples

with very thin gold film in order to improve the electrical conductivity of surface. The element analysis and distribution were carried out using energy-dispersive X-ray (EDS) Oxford instrument, the United Kingdom. Vacuum sputtering samples with very thin carbon film. Images and phases of the coating surfaces were obtained by an Atomic Force Microscopy (AFM) Dimension Icon-PT from Bruker AXS in tapping mode.

4.3.8 Functionality and durability assessment

For quantitative analysis of coating wettability, dynamic contact angle measurements of advancing and receding contact angles were recorded. Distilled water droplets were generated using a needle connected to a syringe pump. The pump was run in infusion and withdrawal modes to create advancing and receding contact angles, which were recorded using a Navitar zoom lens connected to a CMOS camera. The recordings were digitized into still images and images were taken to measure the advancing and receding contact angles using a MATLAB based image processing script developed in house.⁶⁹ To evaluate the liquid meniscus stability, we performed free-falling drop impact tests on coated glass slides. Water droplets (~2.5 mm diameter), generated using a fine needle ($D = 0.25$ mm) fitted to a syringe pump (Cole-Parmer Single-syringe infusion pump), were dropped from varying heights (changing impact velocity) on horizontally positioned coated sample. The impact was captured using a high-speed camera (Phantom v411, 2014 vers). The captured images were analysed via MATLAB and impact speed was calculated by using the law of free fall. Ultraviolet-visible (UV-VIS) transmittance spectrum was recorded using two machines due to availability. The spin coated samples were recorded

using a Shimadzu UV-1800 spectrophotometer double beam instrument over a wavelength range of 400–800 nm whilst AACVD samples were recorded using a SHIMADZU UV-2600 spectrophotometer single beam instrument over a wavelength range of 200–800 nm.

The adhesion was tested using tape-peeling test standard described by testing procedures based on the method of ASTM D3359-09². The coated side of the sample had an elcometer 99 adhesive tape adhered with the use of a 200g (2.25 KPa calculated pressure) block rolled over it twice. A thin eraser was attached under the loading and then the tape was peeled off. The effects were evaluated using Contact angle measurements (θ_A and $\Delta\theta$). The durability of the coating was evaluated using linear abrasion cycles as reported elsewhere. In brief, the sample was placed on sandpaper (Standard glasspaper, Grit No. 240, G.C.P Silicon Carbide Waterproof Abrasive Paper Electro Coated from Sharpness) with a weight of 100 g and moved in a linear fashion longitudinally and transversely by 10 cm in each direction. This is what is defined as a cycle. The contact angle was taken and record after each cycle. Self-cleaning applications were evaluated by dirtying the coating with graphene. The dirty sample was placed at an angle to facilitate directional droplet rolling and a video was recoded showing the removal of dirt from the surface.

4.4 Results and Discussion

4.4.1 Spray Coating

Spray coating was utilized to evaluate a number of key formulation factors of the nanocomposite as coating material. First, the effect of sonication on the stability, morphology and transparency of the resulting coatings was tested

through a time study. The nanocomposite was sonicated for 10, 30 and 60 minutes respectively and the resulting coatings were evaluated using contact angle measurements, photon transmission and atomic force microscopy (AFM). The study was done using RX300 fumed silica particles (size ~7 nm).

The effect of sonication method as outline in Table 4.1 was evaluated utilizing RX300 particles where the set-up (sonic probe and a cold-water bath) was tested with increasing sonication time of 10 minutes, 30 minutes and 60 minutes. The water was replaced after each 10 minutes of sonication to aid in temperature control as higher temperature hinder dispersions and cause the solvent to evaporate at a faster rate.

Name	Conc. (wt%)	Spray Passes	Time (min)	θ_A (°)
Son10	33	10	10	153
Son30	33	10	30	150
Son60	33	10	60	152

Table 4.1 Experimental design of sonication effect on the quality of the superhydrophobic coatings.

Composite coating was formulated using Sylgard 184 with the provided crosslinker at 10:1 ratio in 20 mL of toluene to closely resemble the target composition of the final coatings. To the 1 g of the polymer 33 wt% of silica particle (RX300) was added compared to the wight of the polymer followed by the addition of 0.15 g of TMODS. The suspension was then sonicated as shown in Table 4.1. The effect of sonication time was evaluated using dynamic contact angle measurements, photon transmission and AFM as depicted in Figure 4.5. Concentration of particles was kept constant.

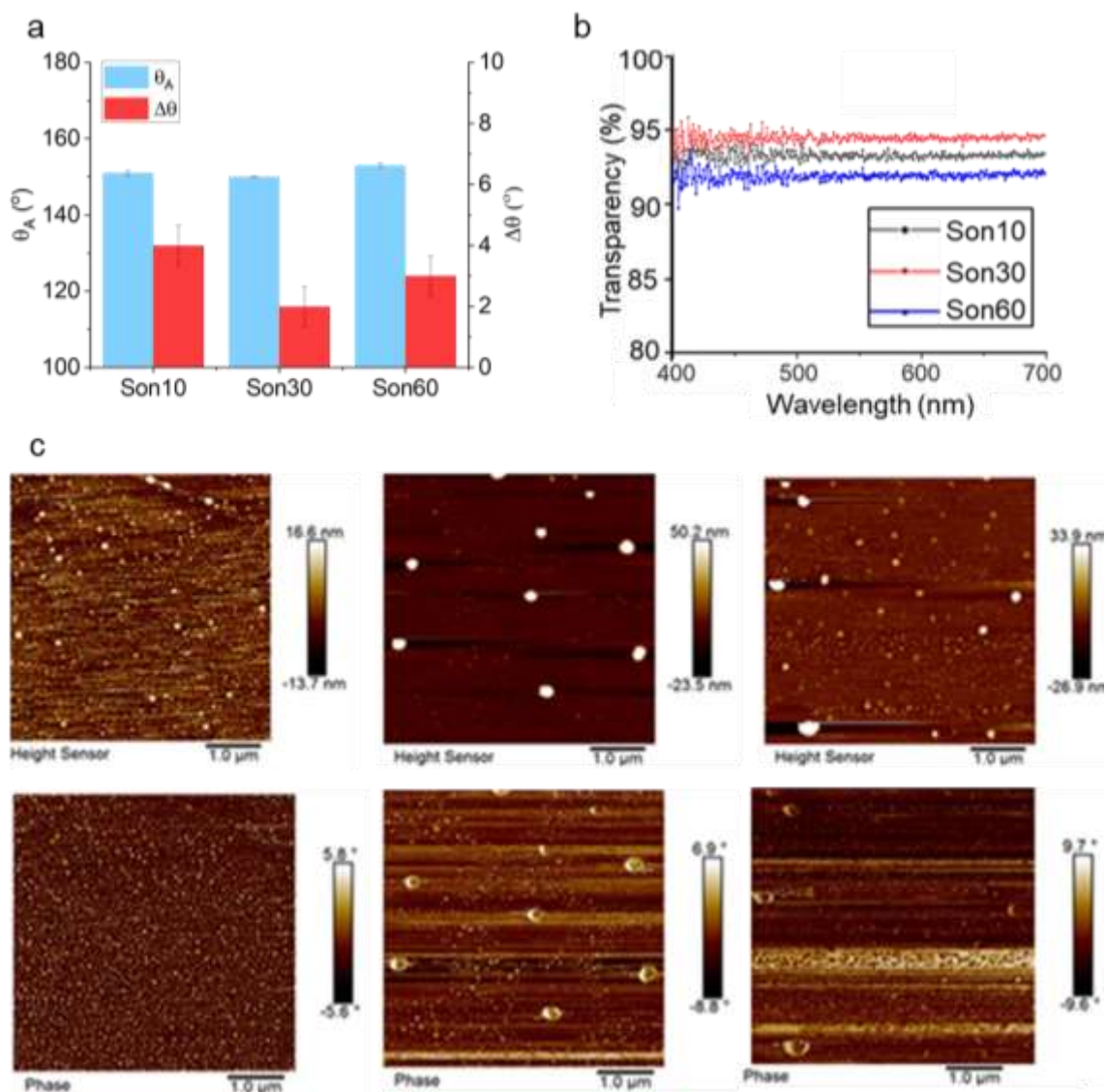


Figure 4.5 Sonication effect analysis using RX300 at constant concentration and spray passes. (a) contact angle (b) transparency and (c) AFM topologies.

From the data, there is minimal variance between the sonication times which resulted in choosing 60 minutes as it showed highest uniformity of the particle dispersion, high contact angle and low hysteresis. The optical transparency reduces at this sonication time, however it remains above 90% compared to glass. Overall, the sonication time allows for scaling of the process with minimal

effort within a cooling system resulting in high transparency, high contact angle and low hysteresis – ideal for transparency applications.

Second, the effect of mesoporosity, size and functionalisation of the silica particles through several assessments based on possible applications of transparent superhydrophobic coatings. This was done through fabrication of three composites using RX300 (fumed silica nanoparticles size ~7 nm); the synthesized mesoporous particles; and after functionalization of the particles with APTES. This work has also allowed for assessing how effective the non-fluorinated silane was and how well the current dispersion method affects coating properties. For clarity, only best performing coatings have been presented in the main body of text (Table 4.2) with the bulk of the study found in the appendix. The fabrication method has been described in Chapter 4.3.2.

Name	Concentration (wt%)	Spray Passes	Transparency (%)	Contact angle (°)
RX5B	33	10	89	150
RX6B	38	10	83	153
MP4B	23	10	90	159
MP5B	33	10	89	159
FMP6B	38	10	87	151
FMP7A	41	5	91	151

Table 4.2 Experimental design of superhydrophobic coatings for Spray coating method where RX = RX300, MP = mesoporous silica particles, FMP = functionalised mesoporous silica particles, number refers to concentrations and A/B indicates number of spray passes.

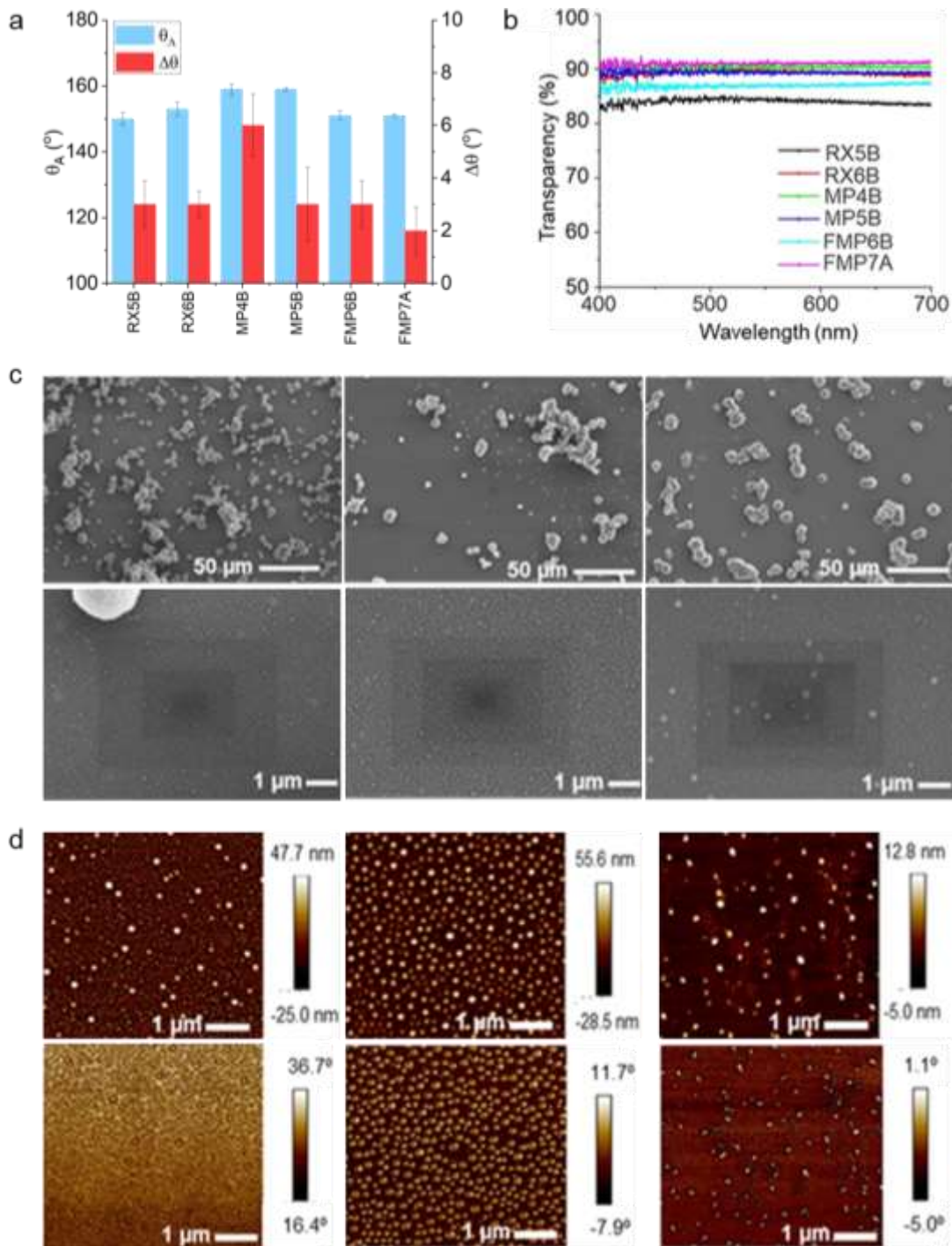


Figure 4.6 Wetting and Transparency analysis and morphology analysis of the selected spray coated samples. (a) Contact angle measurements (b) photon transmission data (c) SEM images of the optimal coatings (RX6B- left, MP5B- middle and FMP7A- right) (d) AFM morphology and phase analysis (RX6B- left, MP5B- middle and FMP7A- right).

With the fabrication process defined, the resulting coated samples as described in Table 4.2 were characterized and evaluated as demonstrated in Figure 4.6. The effect of particle loading concentration, morphology and functionalisation was evaluated against their effect on superhydrophobic behaviour.

From Figure 4.6a, the minimal concentration of particles required was very similar for all three types. It is crucial to understand that the fabricated particles are more than 10 times larger than those of RX300 indicating that porosity plays a crucial role in achieving roughness needed for Cassie-Baxter wetting. The functionalisation of particles shows a decrease in contact angle achieved; however, it also demonstrates a reduction in hysteresis (mobility of the droplet) at the optimal concentration compared to both RX300 and non-functionalised particles.

The crucial benefit of functionalisation can be seen in Figure 4.6b with the optimal coating (FMP7A) achieving highest transparency (above 90°) greater than the far smaller RX300 particles. This is further supported by the morphology analysis in Figure 4.6c-d where the coating shows highest degree of uniform structures both at the 50 µm and the 1 µm scale.

There is a larger presence of nonuniformly distributed micro-agglomerates which form spherical groups like that of a polymer drop. This could explain the extent of the drop seen as the contact angle reaches that of PDMS film which would also explain the higher charging noticed during SEM analysis. For the hypothesis of PDMS particle encapsulation, AFM (Figure 4.6d) was used to evaluate the phase difference and height of the nanostructures of the selected nanocomposites. The study has confirmed that at the nanoscale of the three

coatings vary in height and uniformity of the roughness. Further to this, the phase analysis demonstrated that more particles are present at the surface of the RX300 and MP series whilst functionalisation results in higher expression of the polymer at the surface. This in turn benefits transparency (Figure 4.6b) but is limiting the contact angle (Figure 4.6a).

Fabrication of fluorine-free superhydrophobic coatings with high optical transparency has been achieved utilizing a facile spray coating method. PDMS-silica nanoparticle composite coatings were spray coated onto untreated glass slides resulting in advancing contact angles above 150° and low hysteresis below 4° which indicates applicability in self-cleaning surfaces as the droplet does not pin to the surface allowing mobility which could be utilised to clean the surface of any dust or dirt.

Utilizing the established spray coating method, application study of using titanium source TTIP as crosslinking agent for Sylgard 184 (PDMS) has been evaluated using the RX300 series due to readily available particles towards achieving transparency whilst sacrificing photoactivity achieved in the previous chapter. The work aims to establish a superhydrophobic coating with high optical transparency with the introduction of titania groups within the polymer framework. Contact angle measurements and photon transmission were analysed followed by the adhesion of the optimal coatings using standard tape test.

The first parameter assessed for the hybrid material was the dynamic contact angle to evaluate the wettability of the coating. Results obtained were then

directly compared to the standard crosslinked coatings from the RX300 series. The direct comparison of the selected coatings can be seen in Figure 4.7a.

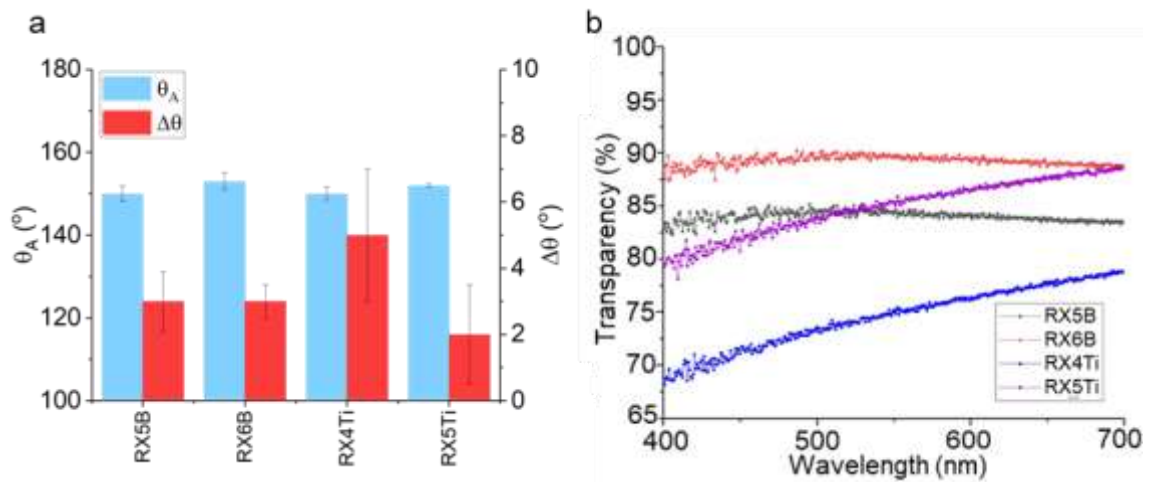


Figure 4.7 Comparison of the selected coatings for the standard and the hybrid RX300 series (a) Contact angle and (b) photon transmission.

Evaluation of the data indicates an enhancement in the contact angle of the coatings even at the lower particle wt% indicating the titanium pockets formed in the nonpolar media behave similarly to those in Chapter 3. As shown in Figure 4.7a, a reduction of 4 wt% in particle loading was required to achieve θ_A in excess of 150° however $\Delta\theta$ for the sample was higher than standard crosslinking reaching $4^\circ \pm 1^\circ$ which is an increase of 1.5° . This increase in hysteresis indicates that the surface of the material was less uniform than that of the RX300 series. When comparing the optimal coatings for the two composites, despite the hybrid not reaching as high θ_A ($152^\circ \pm 1.5^\circ$ compared to $155^\circ \pm 1.5^\circ$ for standard) the $\Delta\theta$ was much lower at $2^\circ \pm 1^\circ$ which indicates the droplet is more mobile on the surface which would be ideal for self-cleaning applications.

Further comparison between the hybrid and standard crosslinking was conducted using photon transmission measurements. This was done to evaluate the impact the titanium pockets have on the optical properties of the material which is another focus area of this research. For clarity of the data, again the selected coating can be seen in Figure 4.7b.

The curvature obtained from the analysis can be attributed to a number of factors. First, the extent of the curvature at the lower wavelengths can be partially accounted for due to absorbance of the titania at lower/ near UV wavelengths as this is the active zone of titanium pigments however this does not account for the extent of the curvature going beyond 500 nm. This suggests that scattering from the introduction of the titanium into the polymer occurs, indicating the crosslinking in nonpolar media is not as defined or controlled as described in the work by Dalod et al⁷ which could be associated to a number of reaction determining factors such as hydroxylation of the titanium precursor or miscibility with the solvent causing larger pockets of titanium to precipitate within the polymer network.

However, comparing the hybrid to the standard coating in Figure 4.7b especially focusing on the optimal coatings, both materials reach 89% of transparency compared to glass at the wavelength of 700 nm. To that extent it was decided to utilise this wavelength as a comparison point. This is because the scattering or absorbance was assumed to be the lowest which resulted in the highest transparency for all the coatings. To analyse potential applicability of the coatings, adhesion analysis was conducted through tape peel test. Contact angle measurements were recorded after one tape peel as seen in Figure 4.8.

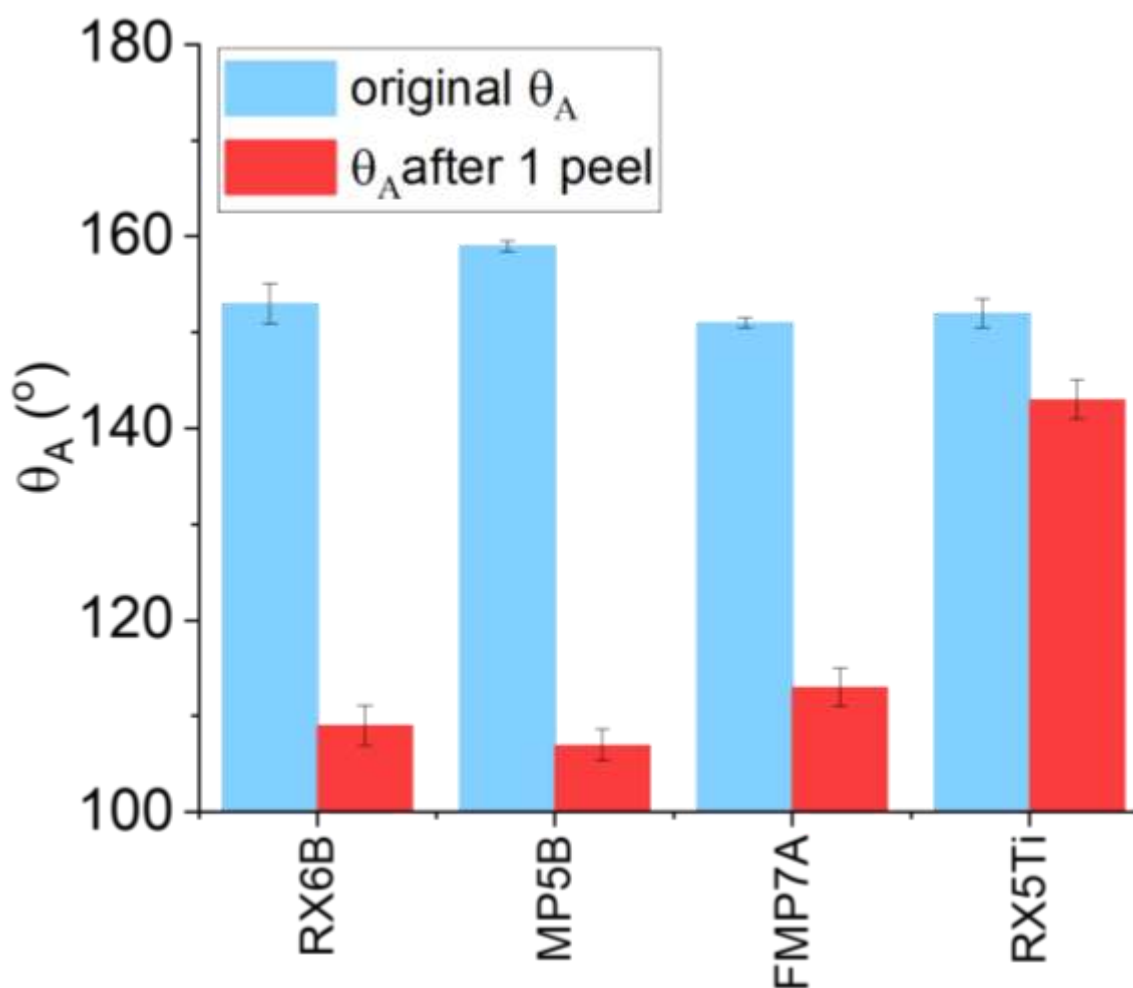


Figure 4.8 Adhesion tape test of the selected nanocomposite concentrations for RX300; MNPS120; FMNPS120; and RX300Ti (hybrid).

The overall durability in term of adhesion to substrate was low as all the coatings show the loss of superhydrophobic behaviour after one tape cycle. The weakest durability can be seen by sample MNPS120 with contact angle reduction from $159^{\circ} \pm 0.5^{\circ}$ to $107^{\circ} \pm 1.6^{\circ}$, which is comparable to that of a smooth hydrophobic surface. This indicates that the coating does not bind to the glass substrate as it was easily removed from the surface using tape adhesive. In support of the hypothesis that the titania pockets promote the adhesion of the coating to the glass substrate, the lowest loss of contact angle was seen by the

RX300Ti coating. The drop of only 12° indicates that there was a much higher degree of adhesion compared to that of the unmodified RX300 which has seen a loss of 46°, almost four times as much.

The results from this initial method application suggests that the coating composite does not work well with spray coating. The hypothesis is that the rapid solvent evaporation experienced in this method inhibits the interactions between the titanium precursor and glass whilst causes larger pockets of titanium to form within deposited droplets hence hindering uniformity and as a result the transparency of the final coating.

4.4.2 Spin Coating

The nanocomposite was formulated of titanium crosslinked PDMS with APTES functionalised mesoporous silica in toluene as solvent. The details of the formulation of the composite can be found in section 4.3.2, while the particles were discussed in full in Chapter 2. The samples were deposited onto glass substrate using dynamic spin coating. The initial study works to understand how particle morphology and functionalisation affects coating behaviour in terms of wetting and transparency. To do this, both mesoporous and non-porous silica particles of the same size were used. This looks to further define the need for structured particles to achieve non-uniform roughness desired for Cassie-Baxter wetting.

Mesopores permit the homogenizing of the particles within the polymer media in relation to achieving greater transparency to non-porous silica particles.^{187,309,337}

Grafting of the APTES groups onto silica nanoparticles through silanization has

been thoroughly discussed in Chapter 2 but two functions of the method are key for this composite and as such are reviewed below.

Firstly, the process reduces the surface energy of the particles which fosters dispersion within organic solvent. This is essential because the polymer used in this work swells more in nonpolar solvents thus the removal of hydroxy functionality of the particles (as previously discussed due to synthesis in polar media) improves the homogeneity of the coating improving transparency and adhesion. Secondly, steric hinderance created by the additional functionality between particles reduces agglomeration in the composite due to the larger size of the groups to that of they original hydroxy groups as seen in Figure 4.9.

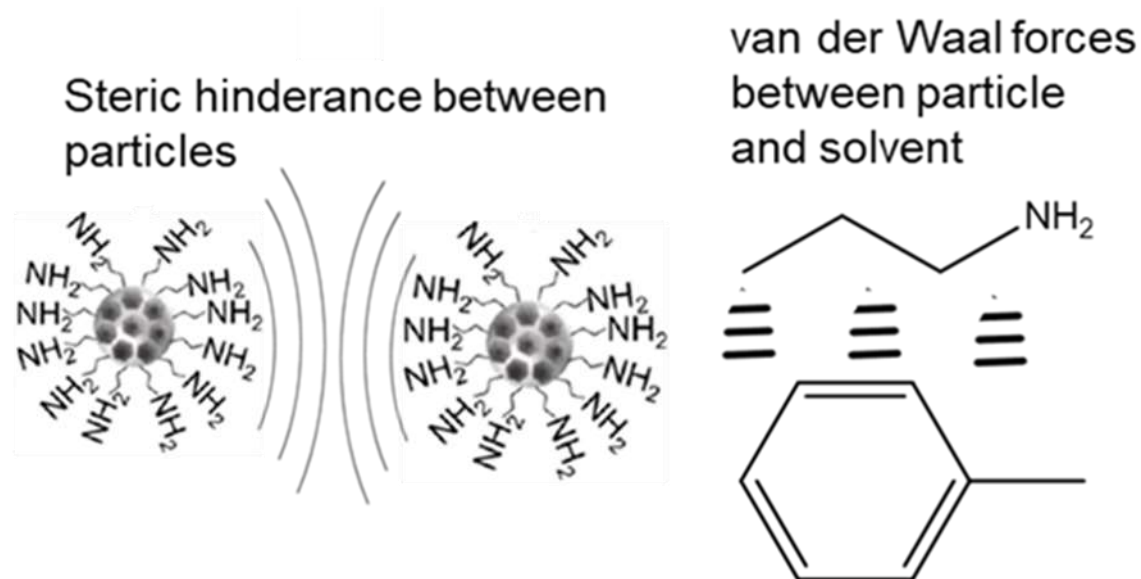


Figure 4.9 Visualization of the effect functionalization of the silica particle has on dispersion in solvent.

To examine the extent of mesoporosity influence on the behavior of the coating in terms of transparency and wetting, two samples (both at 43 wt% particle loading) were prepared by spin coating, using both non-porous and mesoporous particles both at 120 nm silica in size with results presented in

Table 4.3. The synthesis method for both particles can be seen in Chapter 2.3.2.

Particle Type	Particle Conc. (wt%)	θ_A (°)	Transparency at 550 nm (%)
Mesoporous	43	152 ± 2	50.7
Non-porous	43	142 ± 6	47.5

Table 4.3 Evaluation of the effect of mesoporous silica on coating properties versus non-porous silica particles through contact angle and transparency.

From the comparison in Table 4.3, mesopores have a direct impact on the transparency and wetting behaviour of the resulting coating with an enhanced transparency of 3.2% at 550 nm wavelength and an overall improvement in advancing contact angle of 10°. This is supported by the literature which also noted the benefits of reducing the particle (mass) density in order to improve transparency of the coatings as the pores allowed for the polymer to fill the particles increasing homogeneity.³⁰⁹ The difference in the contact angles seen due to the presence of mesopores, means the surface goes from being hydrophobic (below 150°) to superhydrophobic. Further note is within the standard deviation of the measurements which is indicative to the homogeneity of the coating. Due to the aforementioned filling of the pores with the polymer, the surface of the coated material becomes more homogenous in nature while the particle size and arrangement still results in non-uniform roughness needed for Cassie-Baxter wetting.

Having established the benefits of mesoporous particles by both spray coating indirectly and directly by spin coating, the next step was to fabricate coatings with the aim of reaching transparency and superhydrophobicity. As such, the deposition of the formulated nanocomposite was performed using a spin coater with 4,500 rpm for 60 seconds, the results of which are shown in Figure 4.10 - Figure 4.12. Dynamic deposition was selected where the substrate first reached maximum acceleration prior to 1 mL of the coating solution being pipetted onto the spinning glass. The spin coated samples are abbreviated by SC in Figure 4.10 - Figure 4.12. Table 4.4 outlines the samples (e.g. SC1A, SC1B, etc.). Sample SC3C was crosslinked using Sylgard crosslinker as comparison to metal oxide (TTIP) with 50 wt% particle loading concentration and no annealing step.

Name	Particle (wt%)	Annealing step temp (°C)	θ_A (°)
SC1A	33	-	142
SC1B	33	300	140
SC2A	41	-	152
SC2B	41	300	150
SC3A	50	-	154
SC3B	50	300	153

Table 4.4 Experimental design of titanium crosslinked PDMS superhydrophobic coatings for Spin coating with indication of secondary heat treatment or not.

To evaluate the effect of temperature on the crystal structure of titanium species, a second batch of coatings was produced following the same procedure with the addition of an annealing step at 300°C for 60 minutes. The

higher temperatures are comparable to AACVD fabrication, typically done in the range of 200-500 °C, for direct comparison of the two methods.

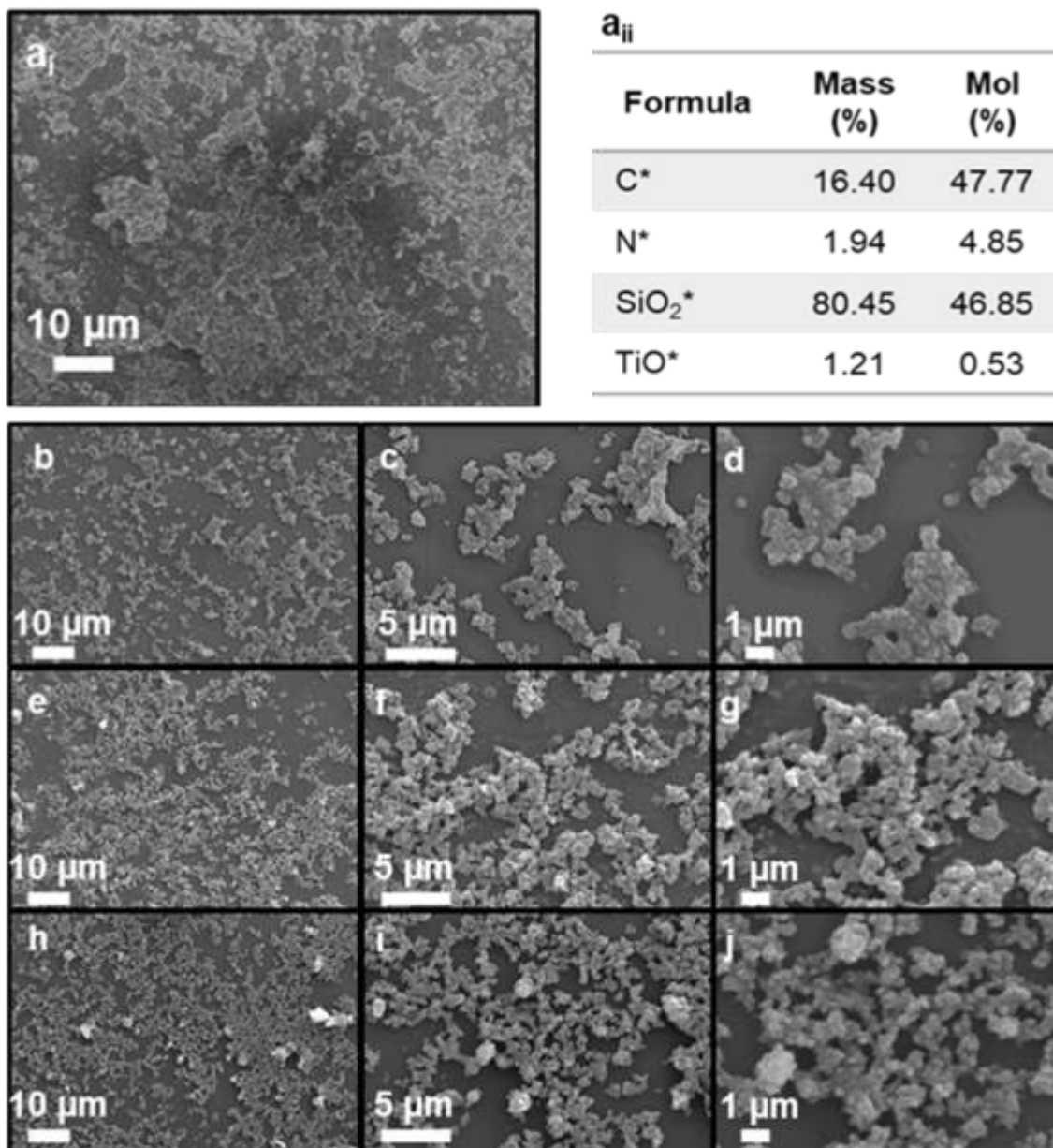


Figure 4.10 Morphology and chemical analysis of SC1A (a) SEM-EDS analysis with data in table. Evaluated zone shown in (a) and data in (a_{ii}). SEM images of spin coated samples (b-j) where (b-d) is SC1A (e-g) SC2A and (h-j) SC3A.

The surface morphology of the resulting coatings, as well as chemical composition, was analysed using scanning electron microscopy Energy-

dispersive X-ray spectroscopy (SEM-EDS) and ATR-FTIR, as shown in Figure 4.10 and Figure 4.11a. The SEM shows that a non-uniform roughness required for Cassie-Baxter state has been formed. However, the resulting coatings were non-homogenous in roughness due to high degree of agglomerates exhibited at the surface seen in the images as micro dense and heavily charging microstructures. This formed despite good dispersion prior to coating the glass substrates and has potential transparency detriments, as the size of these structures is expected to cause scattering of visible light impacting clarity and haze limiting the applicability of the method for this nanocomposite.²⁶⁵

The combined EDS and ATR-FTIR (Figure 4.10a and Figure 4.11a) demonstrates that there was a successful incorporation of the titania species into the matrix with a calculated 1.93% of mass being titanium. The FTIR spectra shows the presence of hydrocarbon groups (peaks around 2900 cm^{-1}) which are attributed to the silane (TMODS) used to lower the surface energy of the resulting material. Further peaks can be seen around 1050 cm^{-1} and 790 cm^{-1} which were described previously in Chapter 2 and as such are corresponding to the silica particles used in the composite. However, the intensity of the peak at 790 cm^{-1} has increased compared to that of particles which is indicative of the Ti-O-Si bond formation. The peak at $\sim 420\text{ cm}^{-1}$ corresponds to Ti-O in amorphous titanium oxide species, which rules out the formation of crystalline titanium such as anatase or rutile and as a result no photocatalytic properties were expected, similarly to what was reported by Dalod *et. al.*⁷ Defined peaks for amorphous silica can be seen at 554 cm^{-1} , 789 cm^{-1} and 1093 cm^{-1} and 2413 cm^{-1} which combined are associated with silica nanoparticles and the polymer (PDMS) matrix.

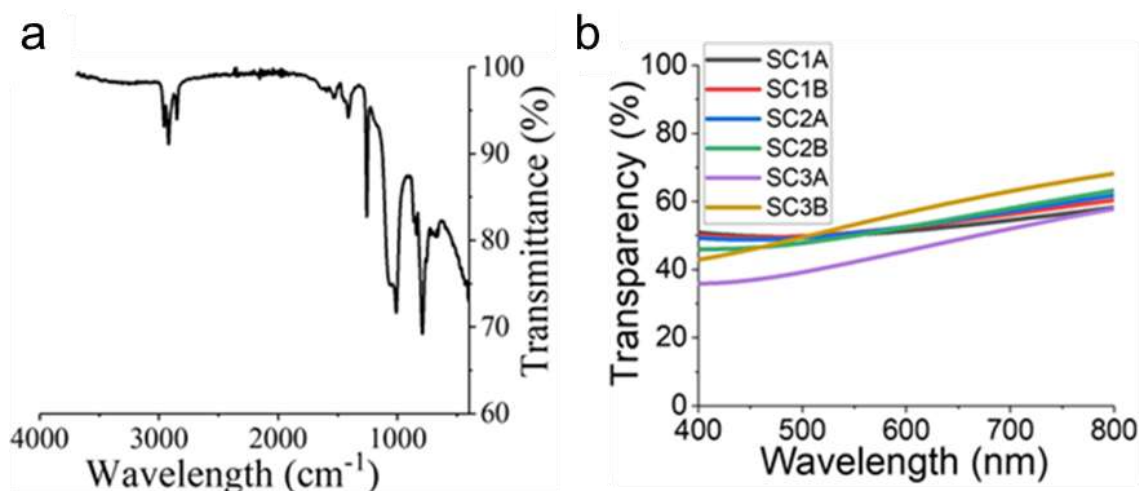


Figure 4.11 (a) ATR-FTIR sample analysis and (b) UV-Vis analysis of coatings with varying particle concentrations (wt%) and heat treatment.

The surface particle agglomeration was less than a few microns in size as shown by SEM imaging (Figure 4.10a and Figure 4.10b-j), and as such the transparency does not seem to differ greatly by particle concentration. As shown in Figure 4.11b, the coatings SC3A and SC3B vary in transmittance by ~10% over the visible light region with average visible transmittance (AVT) of 46% for SC3A and 56% for SC3B; the secondary annealing improves transmittance for higher concentration but this is not seen at the lower concentrations.⁸ This indicates that further functionalization is required to increase the steric hindrance between individual particles and reduce the agglomerates resulting in less scattering and higher optical transparency.

Furthermore, there is a clear similarity between the spin coated samples presented in Figure 4.11b and the spray coated samples in Figure 4.7b where there is a curvature at the lower (below 500 nm) wavelengths. This is indicative of the same problem experienced in the coating method using titanium precursor in nonpolar solvent. The previous hypothesis of deposition being the

driving issue does not hold here as with spray coating the solvent evaporation rate is much slower. This leads to the thinking that the causing factor might be the system temperature. At these lower temperatures, in organic media, the precursor self hydrolyses with any moisture present both at the surface and marginal moisture in the solvent. This results larger clusters of titania species within the polymer.

The functionality assessment was initially conducted through dynamic contact angle measurements (Figure 4.12a) in order to evaluate how effective the fluorine-free nature of the coatings was at repelling water in combination with the morphologies depicted in SEM imaging at increasing magnifications, shown in Figure 4.10b-j for three different concentrations (c.f. Table 4.4). The advancing and receding contact angles were recorded and processed using Matlab from which the difference between the two angles was calculated as the contact angle hysteresis.⁶⁹ This gave a clear indication of the wetting behaviour and droplet mobility at the surface. To better visualise the structures responsible for the achieved contact angles, atomic force microscopy (AFM) was used in 3D mode as shown in Figure 4.12b.

The particle concentration greatly affects the wettability of the resulting coatings due to differences in the roughness. Despite the change being small when comparing SEM images in Figure 4.10b-j, it is substantially more dense and reaching towards higher homogeneity when comparing samples SC1A and SC3A (Figure 4.10b and Figure 4.10h). This is further supported by the AFM analysis depicted in Figure 4.12b which focused on a small section of the coating surface (around 6 μm^2). This as a result leads to the wetting behaviour

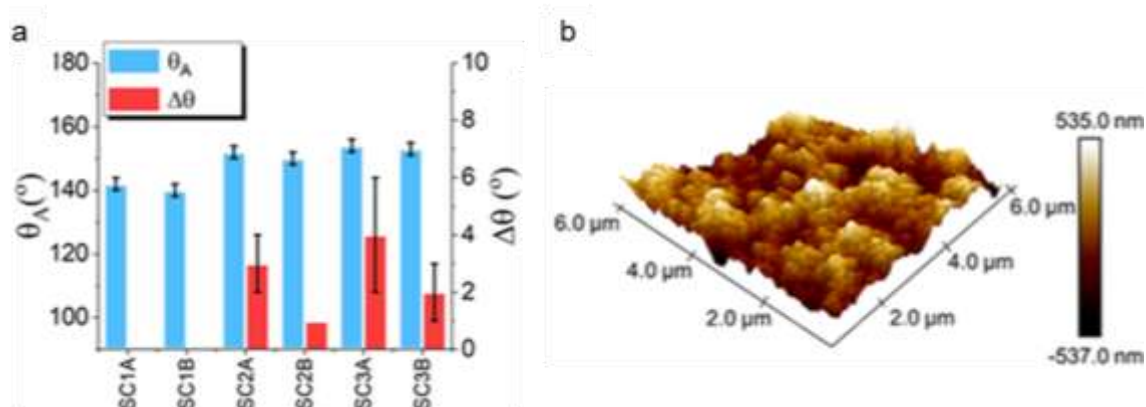


Figure 4.12 Functionality analysis of coatings by (a) dynamic contact angle measurements showing advancing contact angle (θ_A) and hysteresis ($\Delta\theta$) and (b) AFM morphology analysis of SC3A

in Figure 4.12a, where the concentrations shown are 33 wt%, 41 wt% and 50 wt%, the samples remain just hydrophobic at lower concentrations with droplet pinning whilst reaching superhydrophobicity at higher concentrations. This indicates that the roughness created is too low for the lower 33 wt% and while the coating is hydrophobic the droplet is pinned to the surface and is unable to roll-off the material. The first sample to show superhydrophobic behaviour was SC2A with advancing contact angle of 152° and hysteresis of 3° , however the analysis error brings some sites close to falling below superhydrophobicity. This lead to the conclusion that from this set of analysis, the optimal concentration for the particles to reach a stable superhydrophobic level was 50 wt% where the sample reaches advancing contact angle of 154° and hysteresis of 4° .

Further study of the effect of a second annealing step after curing shows that both θ_A and $\Delta\theta$ decrease afterwards which could be explained by the high temperature damaging the structure of the polymer matrix as seen by yellowing of the samples. However, this also increased surface uniformity as the PDMS

was heated and the particles could possibly better set into the matrix hence the improvement in contact angle hysteresis. This is further seen in transparency measurements where the coatings that have undergone thermal treatment exhibit higher levels of transparency.

Overall, using spin coating has addressed a number of issues faced by the spray coating method and helped to clarify issues noted with the method whilst using the titania precursor in place of standard crosslinker. The key finding was that higher system temperature benefit coating uniformity which improved droplet mobility as measured by contact angle hysteresis decreasing by at least 1° compared to no additional heat treatment. However, it is crucial to remember that the lack of initial heat treatment of the substrate or the coating environment still causes the formation of larger clusters of titania species than reported by Dalod et al⁷ as indicated by the curving of the transparency graph in Figure 4.11b and Figure 4.8b for both methods tested so far. This resulted in hypothesis of attempting the fabrication using a system that relies on high temperatures throughout the coating process.

4.4.3 Aerosol Assisted Chemical Vapour Deposition (AACVD)

Water repelling coatings on glass were fabricated using AACVD method from the precursor solutions with variations to particle loading concentrations (specifically 3 concentrations of 9, 17 and 23 wt%) in PDMS/Ti polymer dispersed in toluene solvent. As previously described in Chapter 4.3.2, the polymer network was comprised of Sylgard 184 (PDMS monomer) and titanium isopropoxide as the source of the titanium and the crosslinker for the polymer. This was done to attempt to achieve the benefits of the titania pockets forming

within the polymeric network and form bonds between the glass and the coating material. The deposition was conducted at temperatures between 200 and 400 °C and 15-70 min deposition time to evaluate the effect these two changeable factors have on the resulting material especially in terms of wetting, transparency and durability. In the attempted temperature range PDMS can survive short periods of time before it starts to break down resulting in an unstable and poor coating. Due to the nature of the AACVD method, the particle concentration was kept low to prevent large agglomeration and clogging of the equipment as the nanocomposite was turned into a vapour using a bubbler and a nitrogen gas flow. The variables of each coating have been summarised in Table 4.5 with indications of the resulting advancing contact angles for each sample.

Name	Particle conc. (wt%)	Temp. (°c)	Deposition time (min)	θ_A (°)
AD1A	23	300	70	157
AD2A	17	300	50	161
AD3A	9	300	50	162
AD1B	23	200	55	151 Wenzel
AD1C	23	400	60	164
AD1A15	23	300	15	168
AD1A20	23	300	20	161
AD1A30	23	300	30	167
AD1A50	23	300	50	160
AD1A60	23	300	60	162

Table 4.5 Experimental design of superhydrophobic coatings for AACVD method where AD = AACVD, 1-3 refers to particle concentrations and A-C indicates temperature of the system during deposition.

Surface morphology and chemical composition of the AACVD coated samples were analysed using SEM-EDS, X-ray photoelectron spectroscopy (XPS) and ATR-FTIR (Figure 4.13). Morphology analysis (Figure 4.13a and Figure 4.13b), indicates consistent hierarchical roughness throughout the modified structure which facilitates Cassie-Baxter state. The non-uniform nature of the coating can be attributed to the deposition of droplets onto the surface building up the micro features whilst the particles that are exhibited at the surface form the nanoscale roughness. The EDS map shows consistent coverage of silica and titania where the latter seems be concentrated more around the larger microstructures. Despite playing a crucial role in the morphology of the coating, as expected, the concentration of Ti was low compared to that of Si or O (Figure 4.13c and e) which was expected as these are key constituents of both the particles and polymer. The carbon can be associated with the silane and the polymer.

ATR-FTIR data shown in Figure 4.13d was collected by scrapping the surface layers for sample analysis post fabrication. Clearly defined C-H stretch peaks around 2900 cm^{-1} correspond to the silane functional group and the polymer chains. Peaks corresponding to APTES can be seen in the analysed sample, indicating that the additional silane TMODS most likely binds to PDMS polymer rather than the silica particles. As there is a lack of a strong catalyst in the composite there is a lack of prerequisites to cause amide bond formation between the silanes. That also means that the surface reducing agent can be expected to be throughout the coating meaning that as layers are removed the material will remain superhydrophobic as long as the roughness remains non-uniform and hierarchical.

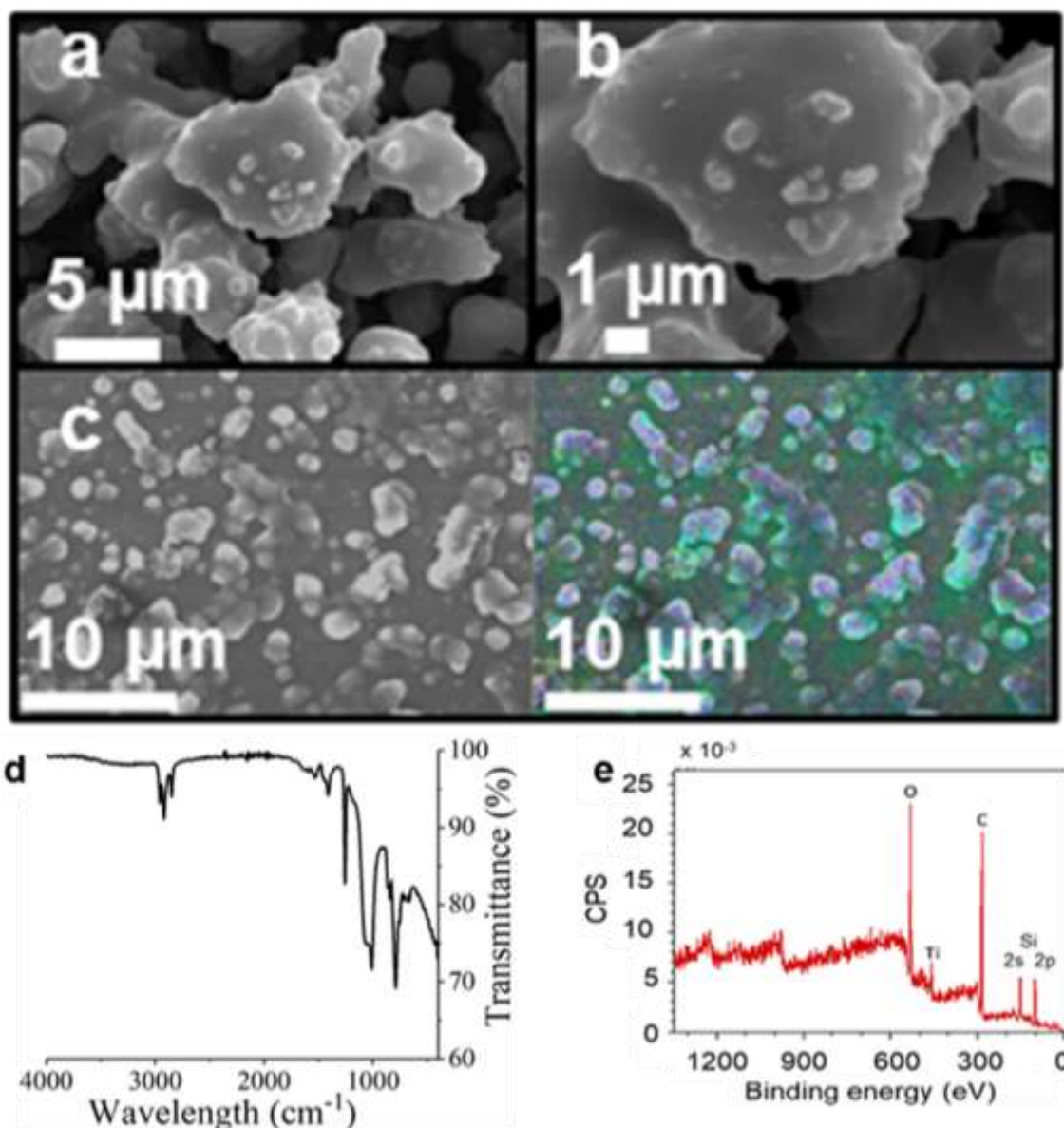


Figure 4.13 Morphology and chemical analysis of AACVD sample (a-b) SEM of AD3A (c) SEM-EDS analysis with composition map where Si - blue, Ti - yellow and O - pink. (d) ATR-FTIR of the coating (e) XPS survey spectra.

Further peaks observed at $\sim 1050\text{ cm}^{-1}$ and 790 cm^{-1} can be attributed to the silica particles as described in the spin coating section. In contrast to spin coated samples, there is a broadening and shift of the Ti-O peak around 420 cm^{-1} region and an emergence of a peak around 1600 cm^{-1} often seen in anatase.

It was theorized that low temperature annealing (heating the sample then holding it at a set temperature before cooling back down to room temperature) of the metal oxide species within the polymer would follow standard procedure of titanium oxide to achieve anatase crystal structures.³¹¹ To better demonstrate this hypothesis, a schematic of the expected annealing process was designed as shown in Figure 4.14. The figure derived from papers reporting on the annealing process of amorphous titanium (IV) oxide species to anatase demonstrates how the low temperature curing of the samples was expected to modify the crystal structure. This was hypothesized as possible due to the size of the particle size within the hybrid polymer.

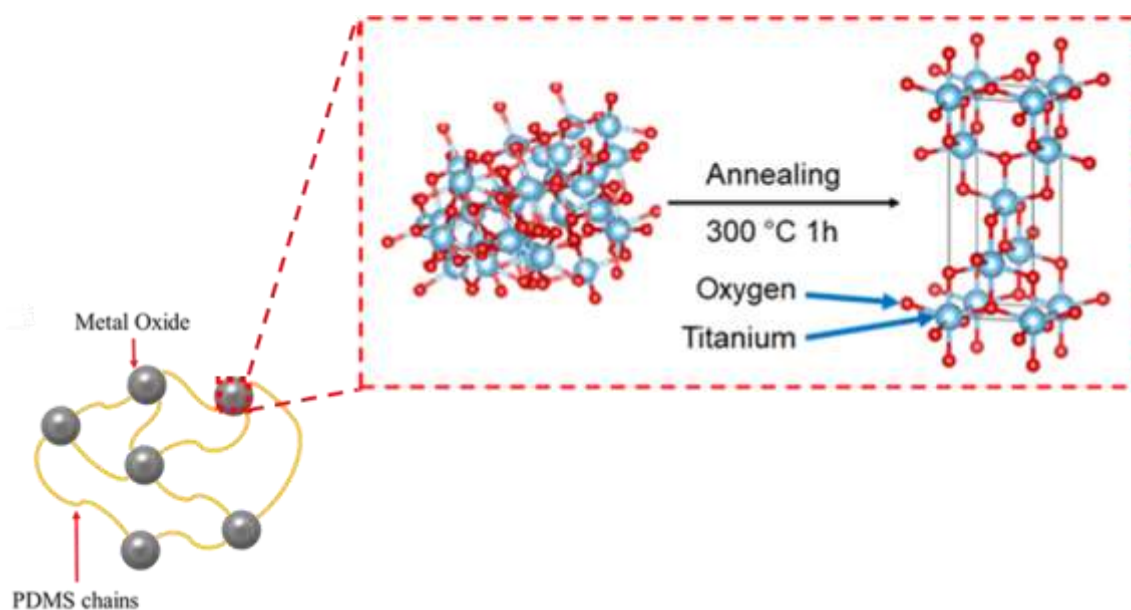


Figure 4.14 Schematic of the hypothesized annealing process for the conversion of titanium oxide particles to anatase.^{8,338}

However, the shift is too insignificant in magnitude to confirm whether there is crystal formation or the beginning of the organisation into crystalline structures. Further evaluation using X-Ray diffraction (XRD) would be necessary to establish the nature of the change. The data from EDS and FTIR was also

supported by XPS (Figure 4.13e) indicating the presence of the four main elements: O, Ti, C and Si.

Evaluation of functionality of the fluorine-free coatings was conducted through UV-Vis spectra and dynamic contact angle measurements, as shown in Figure 4.15a-d. From the dynamic contact angle measurements, advancing (θ_A) and receding (θ_R) contact angles were recorded, with the difference between the two being the contact angle hysteresis ($\Delta\theta$).

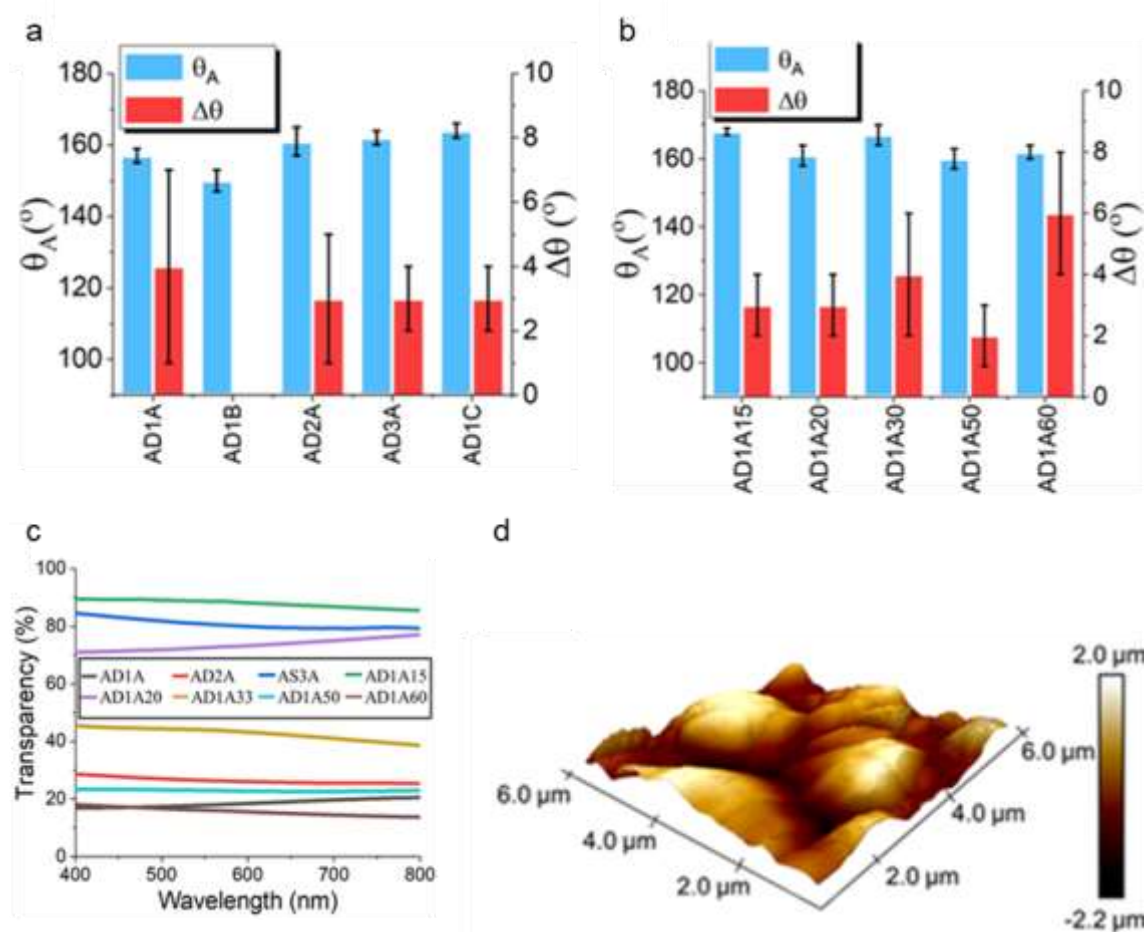


Figure 4.15 Functionality analysis of coatings (a-b) Advancing contact angle and hysteresis of samples with varying (a) temperature and (b) particle concentration (c) UV-Vis analysis of coatings based on change in deposition time (AD1A15-60) and particle conc. (AD1-3A) (d) AFM 3D imaging of AD1A.

All samples made via AACVD achieved contact angles $>150^\circ$ (Figure 4.15a-b), however AD1B exhibited Wenzel state where the droplet pinned to the surface and no $\Delta\theta$ were measured. The only major difference of sample AD1B and other samples was the lower temperature of 200°C used for the deposition which was a finding previously reported in literature^{131,339} indicating that at these lower temperatures there is a process that hinders the fabrication of superhydrophobic coatings. Contact angle hysteresis were recorded below 10° for the Cassie-Baxter coatings, indicating high droplet mobility, which is essential for applications such as for self-cleaning surfaces. The modal hysteresis value for AACVD fabricated coatings was $3^\circ\pm 1^\circ$ showing high reproducibility and uniformity between different coatings with hysteresis values as low as $2^\circ\pm 1^\circ$ for AD1A50. The low hysteresis for that sample can be further explained using the AFM image in Figure 4.15d which shows homogeneity of the roughness at the microscale which would limit the contact between the solid and the liquid phases once a droplet is placed on the surface.

Evaluating the affects of temperature, concentration, and deposition time demonstrate that at system deposition temperatures of 300°C or above there is little variation of the advancing contact angle or the hysteresis with the changes in the other two tested parameters. This is different to the other two tested coating methods (sections 4.4.1 Spray Coating and 4.4.2 Spin Coating) where the dominant drive for superhydrophobicity was particle concentration and not curing temperature. As such, the AACVD method shows as superior in achieving high contact angles and low hysteresis for this nanocomposite and the results work to prove the stated hypothesis of heat being a driving force to the success of the fabrication of superhydrophobic surfaces within this work.

To evaluate the effect of AACVD as a method on the transparency of the coating, UV-Vis (Figure 4.15c) was used. Focusing on the deposition times first, a clear correlation between deposition time and transparency in the visible region was demonstrated similarly to Tombesi *et. al.*⁸⁵ Their trend of decreasing transparency was due to increased time of each layer deposition. However, here the overall composite concentration changes with reduced time where sample AD1A15 was deposited for 15 minutes and exhibited transparency of ~90% compared to glass, whereas AD1A60 which was deposited for 60 minutes and only reached ~20% transparency.⁸ This indicates that with lower deposition time a more transparent coating can be achieved which relates to a lower concentration of the nanocomposite that coats the glass substrate, a trend supported in literature.^{8,85}

Comparing the effect of particle concentration on transparency, the decrease in particle concentration results in a higher degree of transparency from ~20% for 23 wt% to ~85% for 9 wt%.⁸ A similar effect can be seen by decreasing deposition time for the 23 wt% samples as both changes result in a reduction in particle concentration either through reduction in the composite or the amount deposited onto the glass as the deposition is not done to the completion of the nanocomposite.

Therefore, it was concluded that 300 °C was the optimal temperature for the system as there were no noticeable advantages of using higher temperatures whilst detriments were seen when 200 °C was used in terms of contact angle. Furthermore, concentrations as low as 9 wt% of particles was enough to reach superhydrophobicity despite minimal changes were observed while increasing the particle concentration to the contact angle, there was a clear variation in

scattering caused by the other samples. This is supported by literature as higher concentration of particles means there is a greater chance of light being scattered by a particle.²⁶⁵ Thus the additional temperature assisted in the formation of the coatings, however there was a need to compare the effectiveness of this treatment on the durability of the coating, especially between the spin coated samples and AACVD fabricated ones.

4.4.4 Comparison of fabricated coatings

Comparison between AACVD and spin coating as the two methods utilized for fabrication of the superhydrophobic surfaces with the same nanocomposite formulation has revealed a range of characteristic differences. Focusing on the wetting behaviour, composition data and morphology (Figure 4.16), films deposited via AACVD were superior compared to those from spin coating. Table 4.6 outlines the properties of the selected coatings for direct comparison of the two methods. The samples for comparison were based on best performing coatings of the two methods in terms of wetting as analysed in Figure 4.12a, and Figure 4.15.

Name	Particle conc. (wt%)	Temp. (°C)	θ_A (°)
AD1A	23	300	157
SC3A	50	-	154
SC3B	50	300	153
SC3C	50	-	155

Table 4.6 Selection of coatings for comparison of the two methods based on highest concentration of particles for each method.

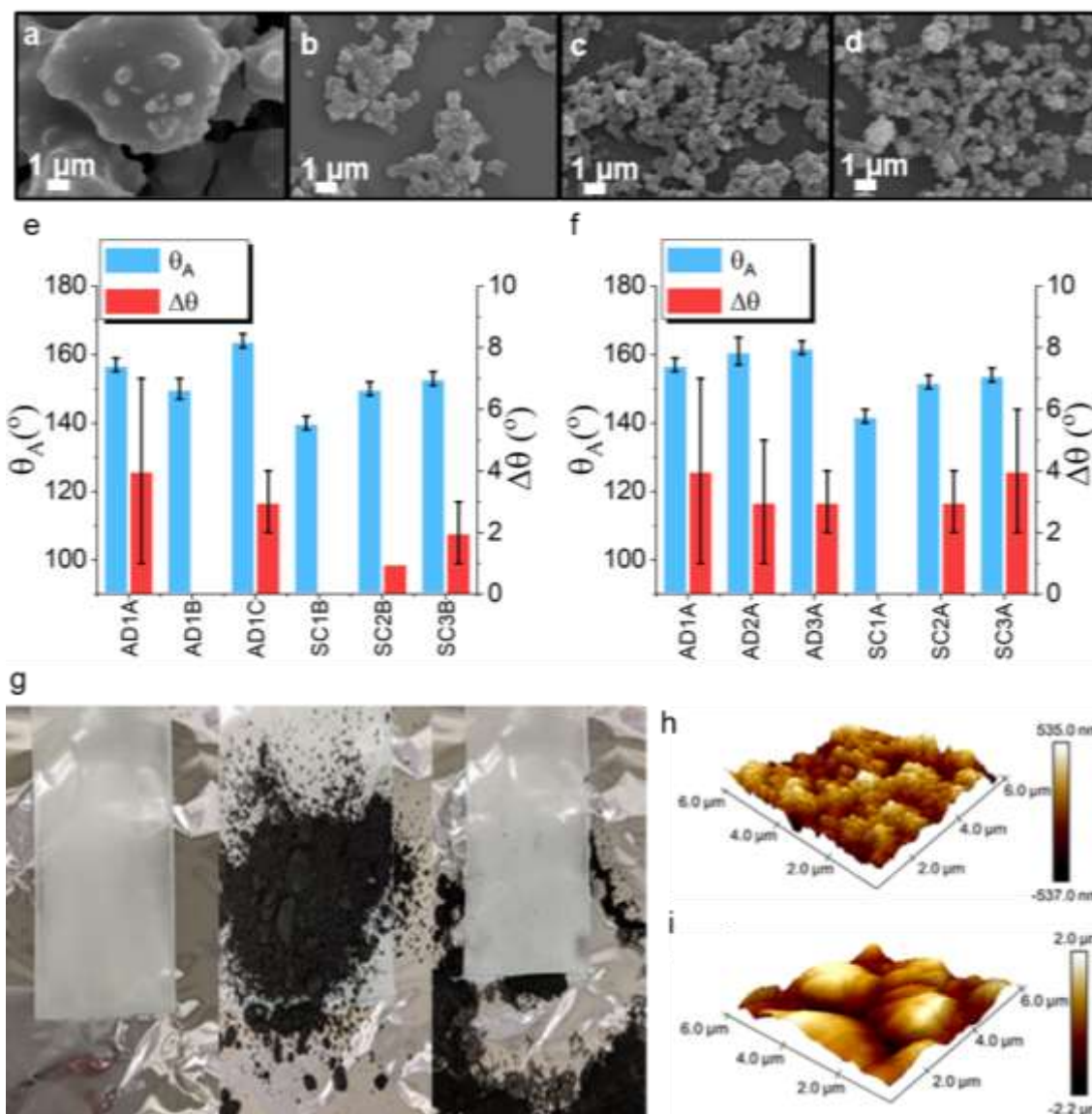


Figure 4.16 Morphology and wettability comparison. SEM analysis of (a) AD1A (b) is SC1A (c) SC2A and (d) SC3A. Influence of (e) particle concentration and (f) temperature on dynamic contact angles of coatings fabricated by both methods (g) self-cleaning of AD1A sample showing before, during and after cleaning. AFM study of (h) SC3A and (i) AD1A.

Morphology comparison of the samples fabricated using the two different approaches is compared in Figure 4.16a-c. Distinct pillar like features previously shown in Figure 4.13 and again in Figure 4.16a have previously been described

in literature,^{118,131,339} however in those works the structures were achieved through *in situ* sol-gel reactions unlike in this work where the composite formulation was done *ex situ*. This indicates that despite having ready made features, such as the particles, the deposition was not adversely affected by it and the resulting coating morphology follows a typical deposition.

Additionally, when comparing the surface morphology of the spin coated (Figure 4.16b-d) samples to that of the AACVD (Figure 4.16a), a distinct advantage in depositing the nanocomposite as an aerosol over relying on centrifugal forces for homogenous distribution can be noticed. The particle arrangement and both the micro and nano structures are more defined which helps to explain the increase in transparency (Figure 4.11b and Figure 4.15) and the enhancement of the wetting behaviour as seen in Figure 4.16e-f. Overall, in contrast to AACVD samples which SEM images indicate the surface morphology was predominantly pillars consisting of particles and polymer, spin coated surfaces in Figure 4.16b-d exhibit predominantly smooth polymer regions with areas of agglomerates.

AACVD prepared sample (AD1A) showed excellent self-cleaning properties (Figure 4.16g) as expected from its morphology (SEM in Figure 4.16a and AFM in Figure 4.15d) and low contact angle hysteresis (Figure 4.16e-f, replotted with data from Figure 4.12a and Figure 4.15). This was observed due to the prevalence of the surface energy reducing groups from the TMODS which have been bonded to the polymer network rather than the particles. Due to the uniformity of the composite via the aerosol deposition, both throughout the material and the surface of the coating express this low surface energy as indicated from ATR-FTIR analysis (Figure 4.11a and Figure 4.13d). The higher

temperatures were not detrimental whilst the surface remained superhydrophobic and the removal of dirt did not weaken the effect as such this coating along with its potential for high transparency (sample AD1A15 reaching 90% as shown in Figure 4.15c) has applicability in smart windows design.

The AFM data indicates a clear difference in the scale of the roughness between the two coating methods with AACVD shown to be in the microscale whilst spin coating remains within the nanoscale. The spin coated sample primarily remains at sub 500 nm roughness whilst the AACVD sample exhibits hierarchal roughness with micro and nano-sized features. The AFM data combined with SEM images provide clear view of the coating morphologies which explain for the difference in wetting behaviour and transparency.

Factors affecting morphologies obtained by AACVD have been extensively studied in literature.^{340–342} The effects of film growth time, temperature, the concentration and choice of precursor, and carrier solvent impacts have been demonstrated to cause distinctive variations in the structures of the resulting coatings, as seen in Figure 4.17.³⁴² Small changes made to the coating deposition and composition within this work support the reported effects as summarised in Table 4.5 and depicted by the examples presented in Figure 4.15. Changing particle concentration, deposition time or temperature has been shown to greatly affect the resulting water contact angle, transparency and morphology.

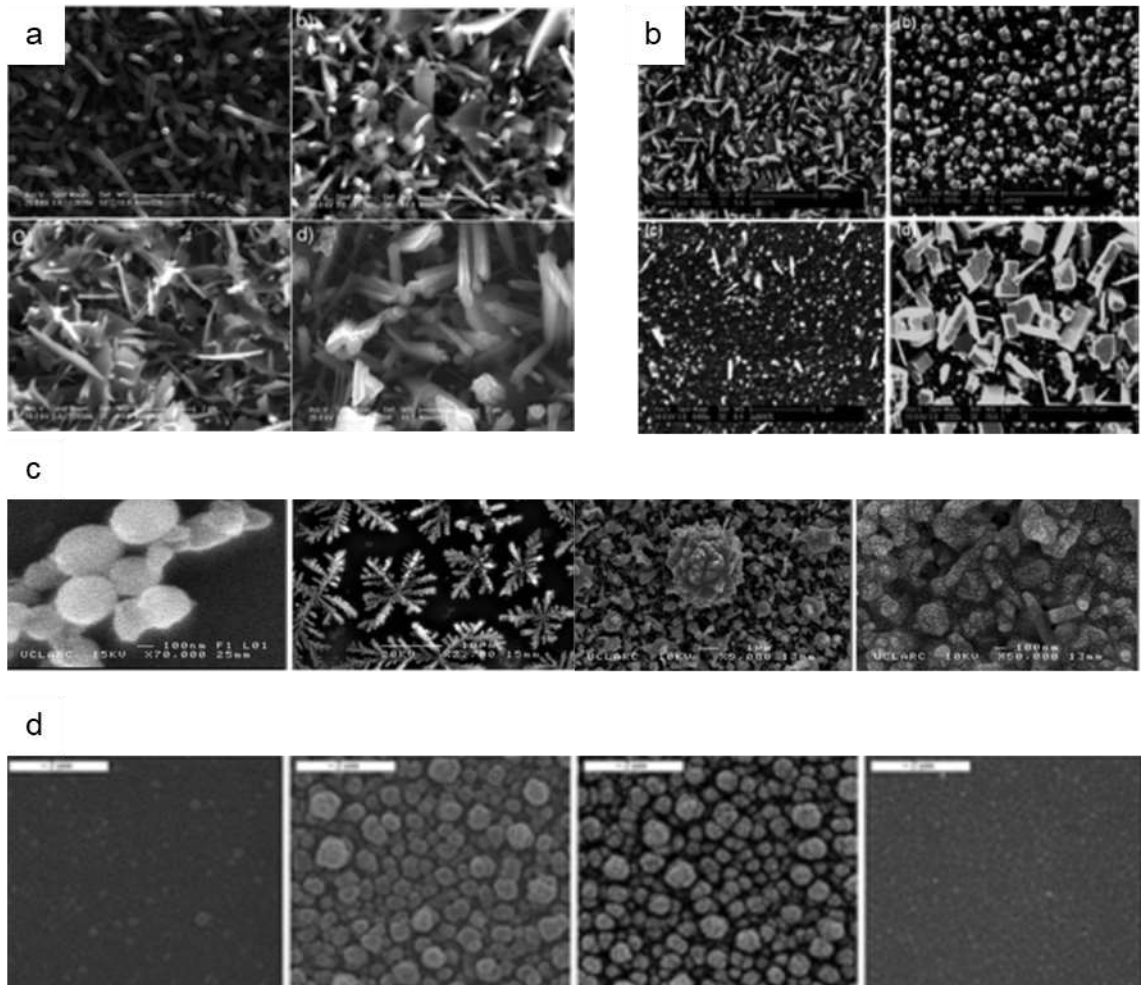


Figure 4.17 SEM images depicting the impact of (a) film growth time³⁴³ (b) temperature³⁴⁴ (c) concentration and choice of precursor³⁴⁵ and (d) carrier solvent³⁴⁶ on the morphology of thin films as prepared by AACVD.³⁴²

The ability to tune a large number of properties of composites greatly benefits the applicability of the method especially in commercial use.³⁴⁰ Design of liquid repelling surfaces especially in the field of transparent and environmentally stable surfaces relies on high hierarchical roughness at low thickness to minimise scattering and improving clarity of the fabricated materials. From the SEM images found in Figure 4.13 it can be seen that the polymer is primarily responsible for the micro-structures which help to explain why the transparency

of the coating is not adversely affected by the increased roughness compared to the spin coated samples as PDMS is transparent in visible light range.⁸ Similar findings have also been reported, where despite high coverage of the glass substrates the resulting transparency readily exceeded 80% compared to untreated glass in the region of 95%.⁸⁵

The hypothesis behind using TTIP was to introduce metal oxide pockets that would form stronger interactions between the substrate and the coating, hence enhancing the adhesion. This was then elaborated into testing the effect of temperature of the coating system based on the preliminary results obtained from the spray coating approach discussed in section 4.1.1 and measured through standard tape test with evaluation of the wetting behaviour in Figure 4.8. This was again tested through the same standard tape test as described in experimental section and analysed using dynamic contact angle measurements as shown in Figure 4.18a due to loss of contact angle with the removal of the coating. To evaluate the effect of the metal oxide compared to standard crosslinker, the samples analysed were compared to a coating prepared using standard crosslinker denoted SC3C (for spin coated samples) provided by Dowsil which was mixed at the recommended ratio of 10:1 polymer to bridging agent. Due to the resulting resistance of the AD1A coating to the tape test, a further durability analysis was conducted using linear sand paper abrasion method (Figure 4.18b) as described in the methodology section. The sample was then further evaluated using AFM imaging to determine the morphology changes from before (Figure 4.18c) and after (Figure 4.18d) the sand paper abrasion.

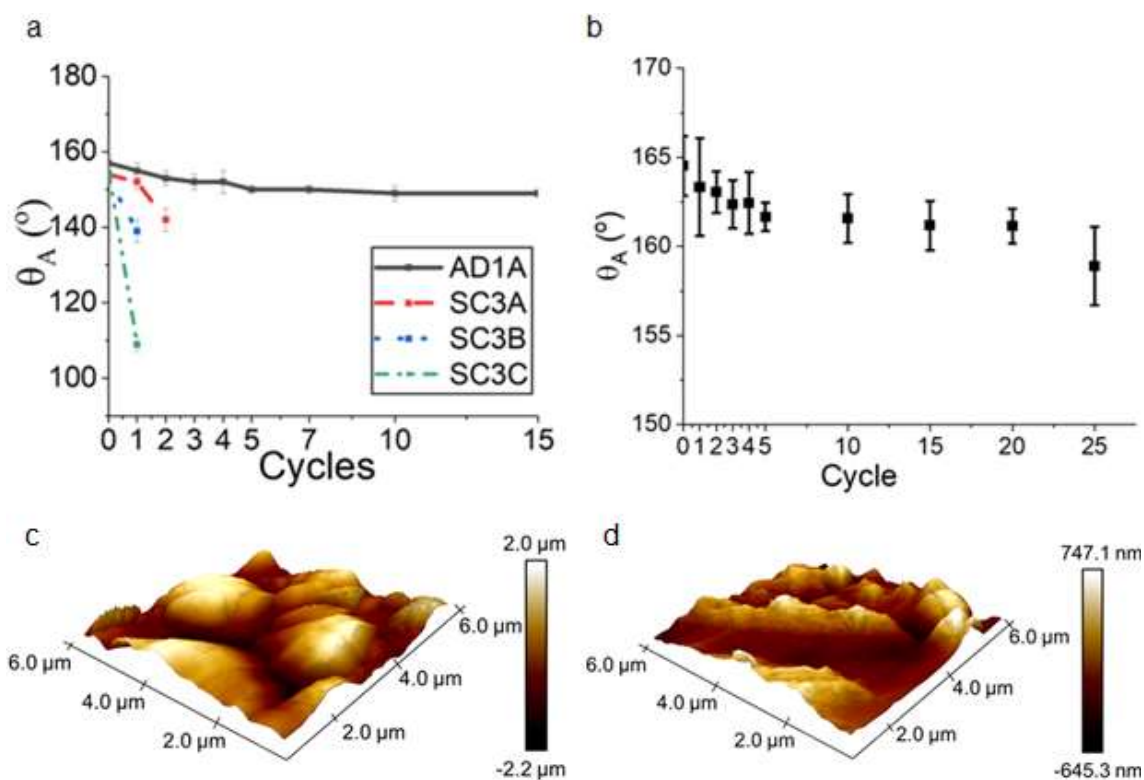


Figure 4.18 Functionality test (a) Cyclic tape peel test to assess substrate adhesion and durability of coatings. AACVD sample are stable well above 10 cycles. (b) Sandpaper abrasion test of AD1A showing durability above 25 linear abrasion cycles. AFM characterization of the surface of AD1A (c) before and (d) after the sandpaper test.⁸

Evaluating the tape test data for AACVD and spin coating, there was a substantial difference between the coating methods. First, when considering just the spin coated samples, the test revealed that the standard crosslinker survived only one peel cycle with a 40° decrease in contact angle which is comparable to that of the data obtained from the spray coating, as demonstrated in Figure 4.8. This is because PDMS does not bond with the glass but rather binds to the substrate, encapsulating it which weakens its durability. As such most of the published coatings rely on prior glass treatments

as discussed earlier in this chapter. The drop in contact angle seen in the Ti/PDMS hybrids was substantially lower with both samples surviving up to 2 peel cycles before reaching contact angles of around 140° which is again comparable to that of the spray coating data.

However, the AACVD samples survived 15 peel cycles and still exhibited superhydrophobic behaviour (Figure 4.18). It was apparent that, although the tape removed a thin layer of the coating, the remaining coating remained superhydrophobic with an overall loss of 7° in advancing contact angle over the 15 peel cycles. This difference in adhesion was the result of the variation in fabrication method since in AACVD the substrate is heated prior to and during deposition whilst in spin coating or spray coating the composite is heated post application to promote curing. This supports the hypothesis that the benefits of the metal oxide are best enhanced in a heated system during fabrication when forming a coating based on the hybrid polymer. In the hydrolysis reaction, heat treatment has been shown to favour the bonds in both gaseous oxygen and the oxygen bonded to the glass to break to free a binding site for the titanium to form O-Ti-O and Ti-O-Si bonds respectively.³¹²

Due to its resistance to the adhesion test, further durability analysis of the coating was conducted through linear sandpaper abrasion cycles as shown in Figure 4.18b. The data demonstrates the high scratch resistance of the AACVD coating beyond 25 cycles when the test was stopped. The coating displayed a total decrease of 6° in terms of advancing contact angle whilst the droplet remained mobile on the surface of the coating indicating that the requirements for Cassie-Baxter state were still being met. Comparatively, coatings in literature exhibit similar or weaker durability to the tested sample such as the

coating reported by Lu et al (40 cycles), Sebastian et al (20 cycles) or Wang et al (45 cycles) though it is worth noting the latter two were tested longitudinally only or in one direction^{278,347,348} where for our method, one cycle was counted as one scratch longitudinally and one vertically. Furthermore, despite the visible damage to the coatings' surface as noted by the AFM imaging seen in Figure 4.18c-d, the high contact angle and Cassie-Baxter state remain which indicates in combination with the adhesion test that as a layer of the coating is removed, the one underneath is also superhydrophobic. This is consistent with the chemical characterisation analysis of conducted on the sample such as XPS (Figure 4.13e), FTIR (Figure 4.13d) or EDS (Figure 4.13c). This lead to the proving of the hypotheses presented throughout this chapter and summarised the AACVD method as superior coating method for the hybrid polymer and particle nanocomposite.

To visualize the differences between all the modified properties to the coatings made using AACVD or spin coating, a summative table (Table 4.7) was designed highlighting the key differences in physical and chemical properties of the coatings.

Sample	Particle conc. (%wt)	Transparent @ 550 nm (%)	Adhesion
AD1A	23	20	15
SC3A	50	40	2
SC3B	50	55	1

Table 4.7 Summary comparison of the coatings based on particle concentration and durability tests and transparency.

The key aspect noted in Table 4.7 is the particle concentration and the resulting adhesion survivability between the coatings. The transparency of the coatings was considered here, however, it is crucial to remember that sample AD1A has the potential to reach 90% transparency when the duration of the deposition is reduced to 15 minutes while retaining the same properties as shown by the contact angle measurements seen in Figure 4.15.

Both methods resulted in superhydrophobic coatings, however AACVD has demonstrated high contact angles ($168^{\circ}\pm 2$) and low hysteresis ($3^{\circ}\pm 1$) at very low particle loading concentrations- as low as 9 wt% (nanoparticle : polymer). Samples produced by AACVD typically achieved higher degrees of superhydrophobicity at lower wt% of particle to polymer with more uniform roughness. All these factors as well as the tunability of the deposition times for the coatings results in higher transparency in the visible region and better adhesion (Figure 4.18) indicating better applicability of the coating.

Utilizing structured and porous silica has been shown by literature to a great extent with success in transparency, durability and self-cleaning.^{85,297-305} Furthermore, the use of both non-fluorinated and fluorinated silanes alongside of these has yielded in very good coatings with high contact angles and low hysteresis.³⁰⁶ However, their application within deposition systems has been limited due to difficulty of achieving homogenous dispersions in polymeric solutions which is why a large number of publications choose to utilize a sol-gel route where precursors are mixed with the polymer then deposited onto substrates where particle growth occurs at the surface of the material.^{85,92,307,308} The use of mesoporous particles synthesized *ex situ* permits to optimize the

structure of the particle prior to coating deposition allowing for control in particle size, morphology and functionality which the benefits can be seen from fabricated coatings. Furthermore, the presence of the pores has been shown to permit the polymer to fill them which resulted in higher transparency by further homogenizing the coating whilst the hierarchal structures gave greater contact angles at lower concentrations.

To better appreciate the presented coatings, Table 4.8 compares two of the best performing samples (AD1A15 and SC3B) to those found in literature. The coatings reported in other publications achieve comparable results to the work presented in this chapter, however it is crucial to distinguish the reported materials by either requiring higher concentrations²⁴⁹ of particle loading in the composite (compared to the polymer) or results are achieved through the use of fluorinated materials^{2,68,70,119,120} either fluoro-polymers or fluoro-silanes. Some examples have been summarized in Table 4.8 showing key variables.

Sample	Particle %wt	Transparency (%)	θ_A (°)	Ref
AD1A15	9	90	168	
SC3B	50	55	153	
MPS-TEOS-POTS	-	90	165	85*
AACVD coated PTFE films	-	91	169	86*
POLYAMIDE 12-SiO₂ (1:4)	4	87	160	349
POTS-SiO₂	100	-	163	90*

Table 4.8 Comparison between manufactured coatings and literature based on particle concentration, transparency and advancing contact angle (θ_A). (*) indicates fluorinated components.

From Table 4.8, AD1A15 shows competitive transparency and contact angle to those reported in literature. This was achieved without the need for fluorination indicating that the produced coating is an environmentally friendlier alternative for the fabrication of transparent superhydrophobic surfaces. The structures formed by the deposition method are comparable to those found in literature as shown in Figure 4.19 despite using *ex situ* approach to particle formation permitting the use of varied morphologies or functionalities as these aspects can be applied through controlled synthesis methods such as sol-gel or silanization without affecting the polymeric network. Whilst reducing deposition times for the AD1A to form AD1A15 has shown transparency of up to 90% in the visible region.

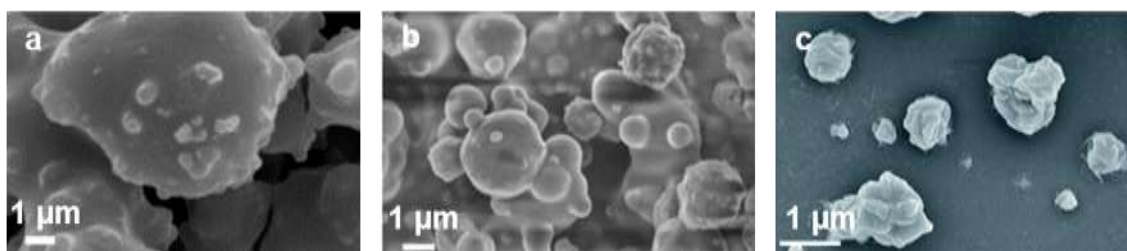


Figure 4.19 Surface morphology comparison between (a) AD1A sample and (b-c) two other coatings from literature fabricated using AACVD.^{85,86}

Furthermore, the successful application of the hybrid titanium-PDMS polymer by Dalod et. al.⁷ modified for use with Sylgard 184 in nonpolar solvents has proven to enhance the durability of the coatings. From the tests performed on the AD1A sample (Figure 4.18) can be seen to be highly competitive to the durability obtained in literature.^{278,347,348} Considering just the methods evaluated by the work, the high temperature of the deposition system proved to be crucial in

achieving this with demonstrated durability beyond 15 adhesion test cycles and 25 abrasion test cycles. This in turn gives the sample a real-life applicability within wall treatments, reducing water waste in cleaning surfaces from dust as well as prevent staining from water-based liquids thanks to the further tested self-cleaning properties of the coating. Additionally, the removal of layers through durability testing revealed that the superhydrophobic nature of the coating is homogenous in AD1A meaning when the top of the modified surface is damaged, it is replaced by another functional layer from underneath.

4.5 Conclusion

Utilizing Sylgard 184 as PDMS source has been demonstrated to be effective for the fabrication of superhydrophobic coatings with high transparency. Several coating methods have benefited from the properties PDMS has such as elasticity, transparency even at high thicknesses and hydrophobic behaviour. This chapter thoroughly applied PDMS in three methods: Spray coating, Spin coating and aerosol assisted chemical vapour deposition. Furthermore, the work took a deeper look at the major drawback of using PDMS which is the limited durability of resulting coatings through further application of the titanium-PDMS hybrid material used in Chapter 3. The original aim was to fabricate durable and transparent superhydrophobic coatings using the hybrid which through extensive contact angle and transparency measurements was achieved using AACVD as the coating method. Despite showing great promise in other methods, the additional heat in the deposition system permitted for the formation of Ti-O-Si bonds between the polymer network and the glass

substrate as demonstrated through extensive adhesion and abrasion testing and seen in the FTIR analysis of the samples.

In terms of further applicability, all methods discussed in this chapter are scalable to industrial scale of production. However, based on the data presented, AACVD showed the best performance at the lowest particle loading concentrations. This along with the high scalability and ease of modification to the method, it shows to be the most attractive method for further coating development. Due to the heating of the deposition system, the introduction of metal oxide (titania) species into polymer matrix was proven to have enhanced the durability of the coating without diminishing desired properties such as transparency or wetting behaviour with a clear indication of the formation of the desired Ti-O-Si bonds through ATR-FTIR indicative of metal oxide bonding to the glass substrate.

The replacement of standard crosslinker for Sylgard 184 PDMS with titania, derived *in situ* from titanium alkoxides precursors, ⁷ a stable fluorine-free material system was formulated for synthesis of transparent superhydrophobic surfaces. The approaches taken, permitted the use of *ex situ* particles providing opportunities to further tailor both the morphology and the functionality of the modified surfaces. Overall, a facile fabrication of fluorine-free superhydrophobic material with good adhesion to substrate has been demonstrated through AACVD, with particle concentrations being as low as 9 wt%. The resulting transparent and fluorine-free coating (AD1A15), demonstrates potential applications in superhydrophobic windows and with further development and testing car windshields.

Chapter 5

Conclusion

Experiments completed with the intention of developing fluorine-free liquid repelling surfaces have focused around the following key research areas: modifying polymer network for enhancement of durability and functionality of the composites, controlled synthesis of mesoporous silica nanoparticles with functionalisation for improved dispersion within nonpolar media and hierarchical structuring of the resulting coating, and assessing coating methods for the fabrication of durable and transparent superhydrophobic surfaces.

Chapter 2 focused on the design and production of structured silica particles with evaluation of porosity and functionalisation processes and has been summarised in Figure 5.1. The formed particles demonstrated uniform porosity of approximately 3 nm in hexagonal geometries which was expected based on the type of surfactant used as pore directing agent. Furthermore, the higher scale of fabrication (10 times to that reported in literature) has proven to yield homogenous particle sizes of 120 ± 5 nm whilst techniques such as TEM were utilised in to visually represent data obtained from ^{29}Si NMR to verify the four environments (Q1-Q4) as porosity. Furthermore, TGA of APTES functionalised particles demonstrated 25% mass loss compared to that of just the particles indicating a very successful grafting process with average of $33.26 \mu\text{mol}$ of APTES has been grafted onto $96.52 \mu\text{mol}$ of particles.

With the design of reproducible and mass scale fabrication of the particles, Chapter 3 then focused on the second key aspect of a nanocomposite which is the polymer itself. Summary of the chapter can be seen in Figure 5.2. To that extent, PDMS was selected as the base polymer for the work due to its transparent and hydrophobic nature. Furthermore, PDMS has been thoroughly used for the design of super water repelling surfaces and as such key improvements have been expressed through literature such as the need for improved adhesion to glass. To that extent, metal oxide hybridisation was evaluated as a potential method to overcome this. Following previously published approaches, transparent films with varying titanium concentrations were prepared to assess the wetting behaviour of increasing metal oxide concentration on the PDMS. To that extent a trend was seen where increasing titanium concentration resulted in reduced contact angle as expected due to hydrophilic nature of the oxide bond.

Following this, the films were then applied into a coating with the idea for the design of stable self-cleaning photocatalytic coatings using anatase as pigment and fumed silica as dopant for stability of the suspension. The resulting coatings followed the same pattern in terms of wetting to the polymer films with only samples A and B reaching superhydrophobicity with contact angles reaching 164° and 162° respectively. Furthermore, carboxylic acid functionalisation at 2.3×10^{-3} mol was sufficient for palmitic and stearic acids to reduce the surface energy enough with the roughness to reach Cassie-Baxter wetting. The crosslinking of Sylgard 184 was also shown as successful in organic solvent with the 10:1 ratio showing similar wetting behaviour (comparing F to H).

This has created the basis for the work in Chapter 4, as summarised in Figure 5.3, where each component of the previous chapters was assessed before being optimised for the fabrication of transparent superhydrophobic coatings. The first method selected was spray coating, this was done due to the rapid and scalable nature of the process. The study found the optimal sonication of the particles at 60 minutes which allowed for the evaluation of the prepared particles against off the shelf hydrophobic fumed silica which highlighted the benefits of both the porosity and functionalisation in achieving transparent superhydrophobic coatings reaching transparency of ~90% and θ_A of ~160°. The introduction of titanium into the polymeric network was shown to enhance durability with a reduced loss in contact angle after a peel test using this method.

This in turn sparked the question of which method would further optimise the coating and achieving durable transparency which has been often difficult without prior treatments to glass substrates (often dangerous and harmful) or using fluorination in order to reduce particle loading. Through testing spin coating and AACVD using the same composite, it was proven that heating the coating system benefits the formation of bonds between the substrate and the composite whilst the aerosol deposition permitted the reduction of particles to sub 10 wt%. The AACVD fabricated coatings readily achieved transparency of above 90 % and θ_A greater than 160° with highs of 169°.

Overall, this thesis demonstrates the design process towards durable, fluorine-free and transparent superhydrophobic coatings. The optimal sample prepared using AACVD (AD1A) showed durability of over 25 sandpaper abrasion cycles and over 15 adhesion peel test cycles whilst AD1A15 (produced at a reduced

deposition time) resulted in transparency of 90% and θ_A of 168°. This work permits for further improvements and additional functionalities both through polymer hybridisation and particle morphologies and functionalisation as it combines the method within an ex situ composite design.

Future work ought to include study into the physical and/or chemical limits encompassing the fabrication of hybrid-polymer networks and the associated impact on the Wenzel, Transition and Cassie-Baxter wetting states. Utilizing different metal oxides, such as ZnO or SiO₂, or even the use of organic compounds such as dicarboxylic acids for the manufacture of the hybrids and the resulting analysis on the physical and chemical behaviour of the polymer films would open a new field of smart materials and facilitate the tailoring of coatings to specific application such as in anti-biofouling, photovoltaic cells or even as thin films for SLIPS modification with known impacts in self-cleaning, anti-icing and anti-fogging research. Finally, further research into the applicability of the SiO₂ mesoporous particles/ hybrid polymer network composites as precursor mixtures in AACVD should be examined using carboxylic acids for reducing surface energy in the fabrication of transparent, durable and environmentally friendly superhydrophobic surfaces.

Chapter 2

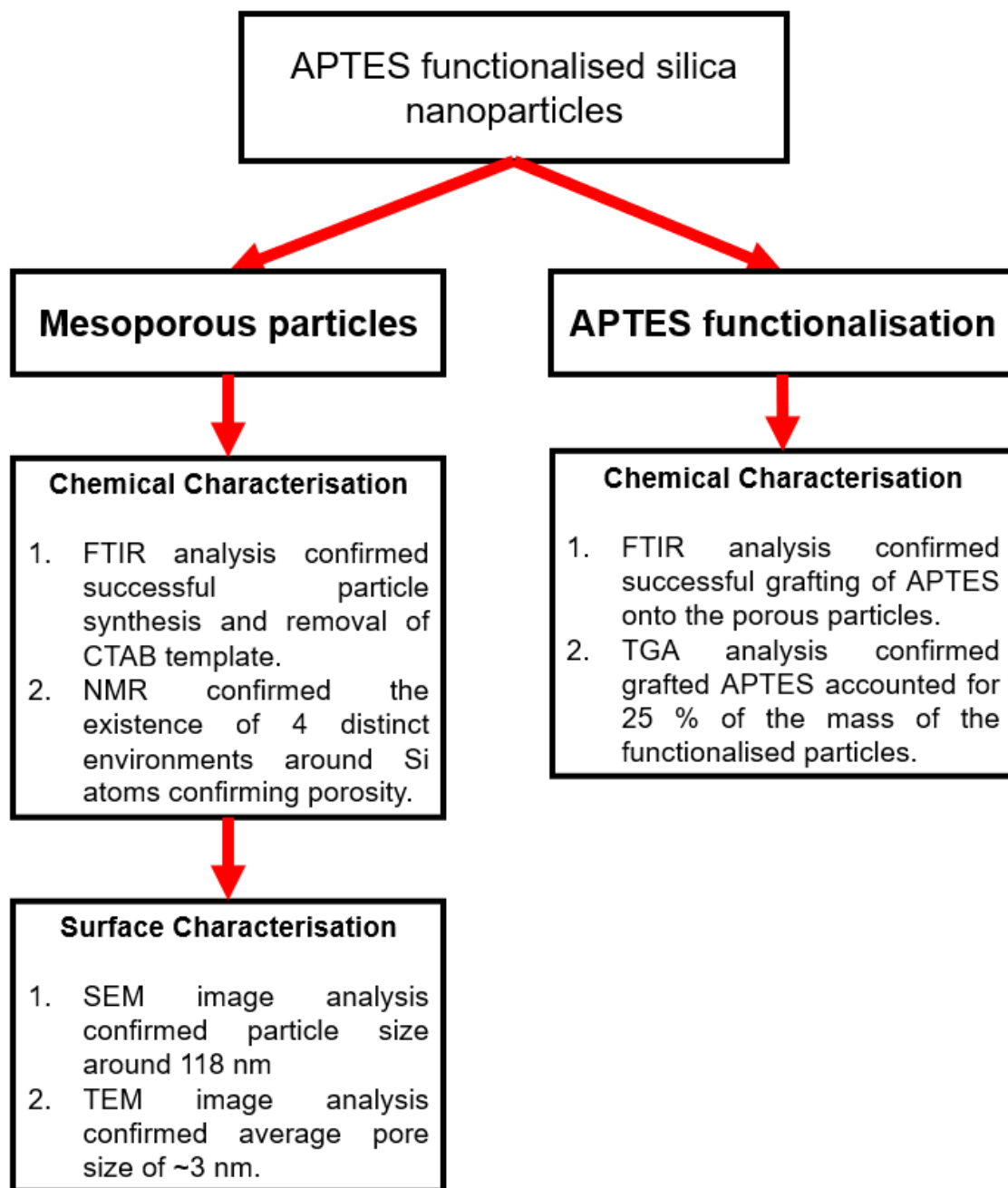


Figure 5.1 Summary of Chapter 2.

Chapter 3

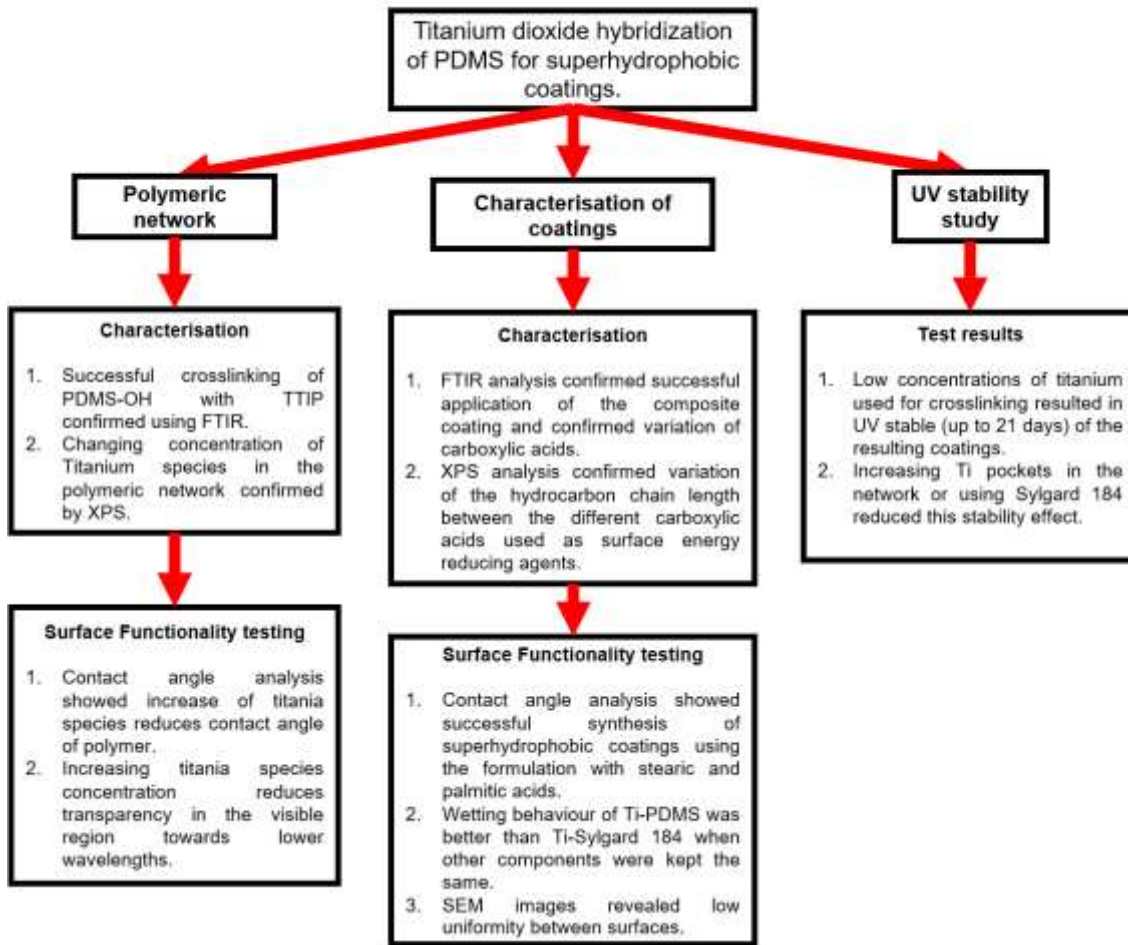


Figure 5.2 Summary of Chapter 3.

Chapter 4

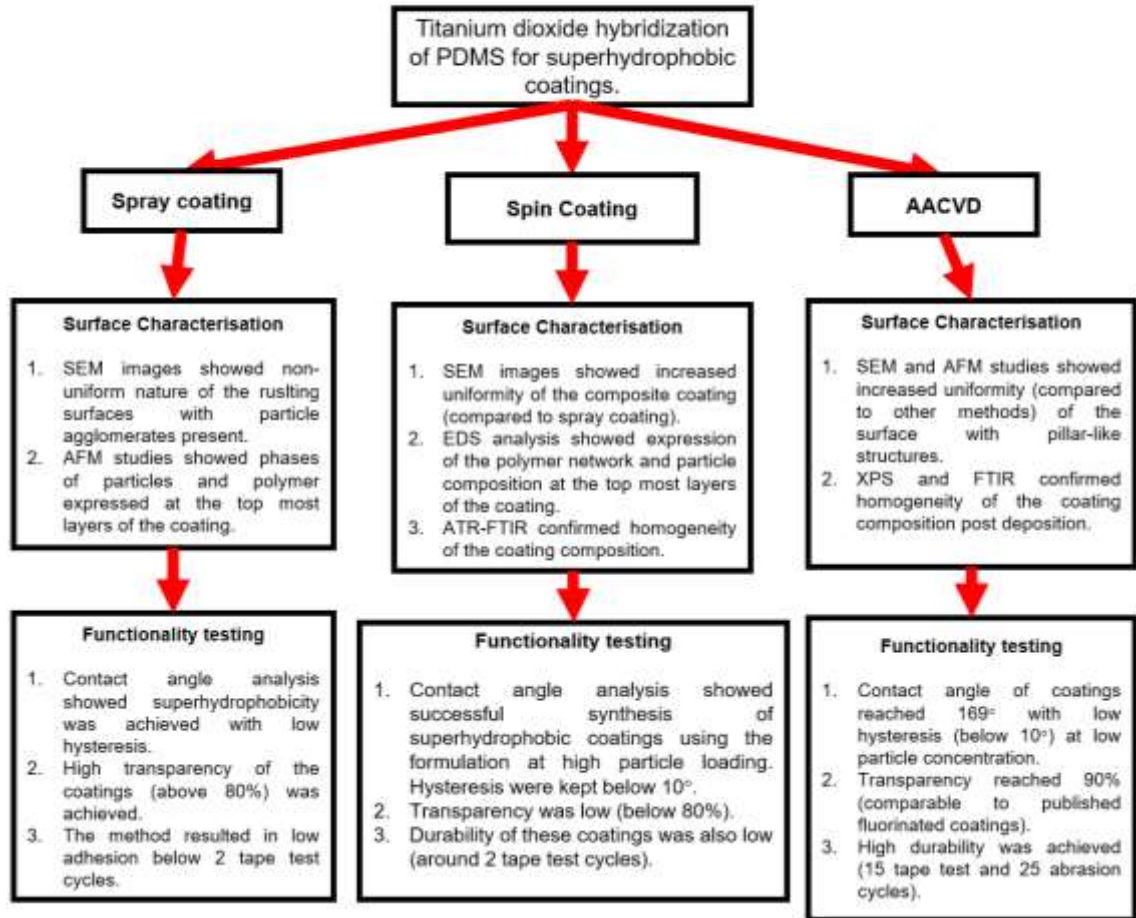


Figure 5.3 Summary of Chapter 4.

Publications

N. J. Janowicz, H. Li, F. L. Heale, I. P. Parkin, I. Papakonstantinou, M. K. Tiwari and C. J. Carmalt, *Langmuir*, 2020, 36, 13426–13438.

B. Bagchi, N. A. Hoque, N. Janowicz, S. Das and M. K. Tiwari, *Nano Energy*, 2020, 105339.

References

- 1 J. Zhi and L. Z. Zhang, *Appl. Surf. Sci.*, 2018, **454**, 239–248.
- 2 Y. Wu, Y. Shen, J. Tao, Z. He, Y. Xie, H. Chen, M. Jin and W. Hou, *New J. Chem.*, 2018, **42**, 18208–18216.
- 3 M. Ruan, Y. Zhan, Y. Wu, X. Wang, W. Li, Y. Chen, M. Wei, X. Wang and X. Deng, *RSC Adv.*, 2017, **7**, 41339–41344.
- 4 M. Grizen, T. Maitra, J. P. Bradley and M. K. Tiwari, *Heat Transf. Eng.*, 2019, 1–10.
- 5 Y. Liu, H. Gu, Y. Jia, J. Liu, H. Zhang, R. Wang, B. Zhang, H. Zhang and Q. Zhang, *Chem. Eng. J.*, 2019, **356**, 318–328.
- 6 S. Das, S. Kumar, S. K. Samal, S. Mohanty and S. K. Nayak, *Ind. Eng. Chem. Res.*, 2018, **57**, 2727–2745.
- 7 A. R. M. Dalod, O. G. Grendal, A. B. Blichfeld, V. Furtula, J. Pérez, L. Henriksen, T. Grande and M. A. Einarsrud, *Nanomaterials*, 2017, **7**, 460.
- 8 N. J. Janowicz, H. Li, F. L. Heale, I. P. Parkin, I. Papakonstantinou, M. K. Tiwari and C. J. Carmalt, *Langmuir*, 2020, **36**, 13426–13438.
- 9 L. Han, Y. Zhou, T. He, G. Song, F. Wu, F. Jiang and J. Hu, *J. Mater. Sci.*, 2013, **48**, 5718–5726.
- 10 Y. Wang, H. Song, M. Yu, C. Xu, Y. Liu, J. Tang, Y. Yang and C. Yu, *J. Mater. Chem. B*, 2018, **6**, 4089–4095.
- 11 Y. Liu, B. Huang, J. Zhu, K. Feng, Y. Yuan and C. Liu, *RSC Adv.*, 2018, **8**,

40598–40610.

- 12 D. Shen, J. Yang, X. Li, L. Zhou, R. Zhang, W. Li, L. Chen, R. Wang, F. Zhang and D. Zhao, *Nano Lett.*, 2014, **14**, 923–932.
- 13 M. Kalantari, Y. Liu, E. Strounina, Y. Yang, H. Song and C. Yu, *J. Mater. Chem. A*, 2018, **6**, 17579–17586.
- 14 C.-P. Hsu, S. N. Ramakrishna, M. Zanini, N. D. Spencer and L. Isa, *Proc. Natl. Acad. Sci.*, 2018, **115**, 5117–5122.
- 15 G. F. Luo, W. H. Chen, Y. Liu, J. Zhang, S. X. Cheng, R. X. Zhuo and X. Z. Zhang, *J. Mater. Chem. B*, 2013, **1**, 5723–5732.
- 16 V. B. Cashin, D. S. Eldridge, A. Yu and D. Zhao, *Environ. Sci. Water Res. Technol.*, 2018, **4**, 110–128.
- 17 S. Chantarak, J. Chang, S. Suwanboon and S. Riyajan, *Mater. Res. Express*, 2018, **5**, 95030.
- 18 A. López-Millán, P. Zavala-Rivera, R. Esquivel, R. Carrillo, E. Alvarez-Ramos, R. Moreno-Corral, R. Guzmán-Zamudio and A. Lucero-Acuña, *Appl. Sci.*, , DOI:10.3390/app7030273.
- 19 A. Kumar, H. Joshi, R. Pasricha, A. B. Mandale and M. Sastry, *J. Colloid Interface Sci.*, 2003, **264**, 396–401.
- 20 S. Underwood and P. Mulvaney, *Langmuir*, 1994, **10**, 3427–3430.
- 21 F. Matter, A. L. Luna and M. Niederberger, *Nano Today*, 2020, **30**, 100827.
- 22 L. Nicole, C. Laberty-Robert, L. Rozes and C. Sanchez, *Nanoscale*, 2014,

- 6, 6267–6292.
- 23 L. S. Shiroma, M. H. O. Piazzetta, G. F. Duarte-Junior, W. K. T. Coltro, E. Carrilho, A. L. Gobbi and R. S. Lima, *Sci. Rep.*, 2016, **6**, 1–12.
- 24 A. M. Galan, G. P. Nordin and S. W. Chiang, *J. Micro/Nanolithography, MEMS, MOEMS*, 2018, **17**, 1.
- 25 K. Raj M and S. Chakraborty, *J. Appl. Polym. Sci.*, 2020, 137, 48958.
- 26 W. Kim, D. Kim, S. Park, D. Lee, H. Hyun and J. Kim, *J. Ind. Eng. Chem.*, 2018, **61**, 39–52.
- 27 J. Oh, S. Yin, C. E. Dana, S. Hong, J. K. Roman, K. D. Jo, S. Chavan, D. Cropek, M. Alleyne and N. Miljkovic, *J. Heat Transfer*, , DOI:10.1115/1.4044677.
- 28 S. P. Dalawai, M. A. Saad Aly, S. S. Latthe, R. Xing, R. S. Sutar, S. Nagappan, C. S. Ha, K. Kumar Sadasivuni and S. Liu, *Prog. Org. Coatings*, 2020, 138, 105381.
- 29 T. Young, *Philos. Trans. R. Soc. London*, 1805, **95**, 65–87.
- 30 R. N. Wenzel, *Ind. Eng. Chem.*, 1936, 28, 988–994.
- 31 A. B. D. Cassie and S. Baxter, *Trans. Faraday Soc.*, 1944, **40**, 546.
- 32 E. G. Shafrin and W. A. Zisman, *J. Phys. Chem.*, 1960, **64**, 519–524.
- 33 S. Wang and L. Jiang, *Adv. Mater.*, 2007, **19**, 3423–3424.
- 34 P.-G. de Gennes, F. Brochard-Wyart and D. Quéré, *Capillarity and wetting phenomena : drops, bubbles, pearls, waves*, 2004.

- 35 S. Dobretsov, J. C. Thomason and D. N. Williams, *Biofouling Methods*, 2014.
- 36 A. W. Adamson and A. P. Gast, *Physical chemistry of surfaces*, 1997.
- 37 T S Chow, *J. Phys. Condens. Matter*, 1998, **10**, 445451.
- 38 K. Y. Law, *J. Phys. Chem. Lett.*, 2014, **5**, 686–688.
- 39 T. Zhao and L. Jiang, *Colloids Surfaces B Biointerfaces*, 2018, **161**, 324–330.
- 40 M. Nosonovsky and R. Ramachandran, *Entropy*, 2015, **17**, 4684–4700.
- 41 Y. Si, C. Yu, Z. Dong and L. Jiang, *Curr. Opin. Colloid Interface Sci.*, 2018, 36, 10–19.
- 42 D. Quéré, *Annu. Rev. Mater. Res.*, 2008, **38**, 71–99.
- 43 R. Tadmor, *Langmuir*, 2004, **20**, 7659–7664.
- 44 A. Dupré and P. Dupré, *Théorie mécanique de la chaleur*, Gauthier-Villars, 1869.
- 45 M. E. Schrader, *Langmuir*, 1995, **11**, 3585–3589.
- 46 Y. Deng, D. Mager, Y. Bai, T. Zhou, Z. Liu, L. Wen, Y. Wu and J. G. Korvink, *Comput. Methods Appl. Mech. Eng.*, 2018, **341**, 113–132.
- 47 M. Silvestrini and C. Brito, *Langmuir*, 2017, **33**, 12535–12545.
- 48 A. Marmur, *Langmuir*, 2003, **19**, 8343–8348.
- 49 A. Lafuma and D. Quéré, *Nat. Mater.*, 2003, 2, 457–460.
- 50 Y. A. Mehanna, E. Sadler, R. L. Upton, A. G. Kempchinsky, Y. Lu and C.

- R. Crick, *Chem. Soc. Rev.*, 2021, 50, 6569–6612.
- 51 C. Ishino and K. Okumura, *Eur. Phys. J. E. Soft Matter*, 2008, **25**, 415–424.
- 52 E. Pierce, F. J. Carmona and A. Amirfazli, *Colloids Surfaces A Physicochem. Eng. Asp.*, 2008, **323**, 73–82.
- 53 B. S. Yilbas, A. Al-Sharafi, H. Ali and N. Al-Aqeeli, *RSC Adv.*, 2017, **7**, 48806–48818.
- 54 G. Hassan, B. S. Yilbas, A. Al-Sharafi and H. Al-Qahtani, *Sci. Rep.*, 2019, **9**, 1–14.
- 55 B. Bhushan and E. K. Her, *Langmuir*, 2010, **26**, 8207–8217.
- 56 T. P. Allred, J. A. Weibel and S. V. Garimella, *Int. J. Heat Mass Transf.*, 2019, **135**, 403–412.
- 57 Z. Shi, Y. Zhang, M. Liu, D. A. H. Hanaor and Y. Gan, *Colloids Surfaces A Physicochem. Eng. Asp.*, 2018, **555**, 365–371.
- 58 R. E. Johnson, *Wettability Volume 49 of Surfactant Science*, CRC Press, New York, 1993.
- 59 D. M. Fopp-Spori, in *Biofouling Methods*, 2014, p. 8.
- 60 M. Zhang, S. Feng, L. Wang and Y. Zheng, *Biotribology*, 2016, **5**, 31–43.
- 61 T. Darmanin and F. Guittard, *Mater. Today*, 2015, **18**, 273–285.
- 62 M. Ghasemlou, F. Daver, E. P. Ivanova and B. Adhikari, *J. Mater. Chem. A*, 2019, **7**, 16643–16670.

- 63 E. Bormashenko, O. Gendelman and G. Whyman, *Langmuir*, 2012, **28**, 14992–14997.
- 64 J. Nickerl, M. Tsurkan, R. Hensel, C. Neinhuis and C. Werner, *J. R. Soc. Interface*, , DOI:10.1098/rsif.2014.0619.
- 65 Xiameter, Guide to Silane Solution Mineral and Filler Treatments Benefits of Silane Treatment Applying Silanes to Fillers, <https://www.azom.com/article.aspx?ArticleID=6774>, (accessed 31 January 2019).
- 66 A. Bede, A. Pop, M. Moldovan and I. Ardelean, *AIP Conf. Proc.*, , DOI:10.1063/1.4938459.
- 67 V. H. Dalvi and P. J. Rossky, *Proc. Natl. Acad. Sci.*, 2010, **107**, 13603–13607.
- 68 S. Pan, R. Guo, M. Björnmalm, J. J. Richardson, L. Li, C. Peng, N. Bertleff-Zieschang, W. Xu, J. Jiang and F. Caruso, *Nat. Mater.*, 2018, **17**, 1040–1047.
- 69 C. Peng, Z. Chen and M. K. Tiwari, *Nat. Mater.*, 2018, **17**, 355–360.
- 70 J. Liu, Z. Janjua, M. Roe, F. Xu, B. Turnbull, K.-S. Choi and X. Hou, *Nanomaterials*, 2016, **6**, 232.
- 71 Z. Wang, I. T. Cousins, M. Scheringer and K. Hungerbuehler, *Environ. Int.*, 2015, **75**, 172–179.
- 72 A. W. Nørgaard, J. S. Hansen, J. B. Sørli, M. Levin, P. Wolkoff, G. D. Nielsen and S. T. Larsen, *Toxicol. Sci.*, 2014, **137**, 179–188.

- 73 A. Blum and A. Soehl, *Highly Fluorinated Chemicals (PFASs): Do the Benefits Justify the Harm?*, 2016.
- 74 A. Blum, Green Science Policy Institute, <https://greensciencepolicy.org/>, (accessed 3 January 2019).
- 75 W. J. Fasano, S. C. Carpenter, S. A. Gannon, T. A. Snow, J. C. Stadler, G. L. Kennedy, R. C. Buck, S. H. Korzeniowski, P. M. Hinderliter and R. A. Kemper, *Toxicol. Sci.*, 2006, **91**, 341–355.
- 76 X. Yu, F. Nishimura and T. Hidaka, *Chemosphere*, 2018, **198**, 311–319.
- 77 T. Eklundh, O. Supervisor, U. Eriksson and A. Kärrman, *Analytical Method Development of Fluorinated Silanes using Mass Spectrometry*, 2018.
- 78 U.S. EPA, *Long-Chain Perfluorinated Chemicals (PFCs) Action Plan*, U.S. Environmental Protection Agency, 12/30/2009, 2009.
- 79 H. M. Ali, M. A. Qasim, S. Malik and G. Murtaza, *Techniques for the Fabrication of Super-Hydrophobic Surfaces and Their Heat Transfer Applications*, InTech, London, 2018.
- 80 S. D. Ponja, I. P. Parkin and C. J. Carmalt, *RSC Adv.*, 2016, **6**, 102956–102960.
- 81 M. J. Powell, D. B. Potter, R. L. Wilson, J. A. Darr, I. P. Parkin and C. J. Carmalt, *Mater. Des.*, 2017, **129**, 116–124.
- 82 N. Chadwick, S. Sathasivam, A. Kafizas, S. M. Bawaked, A. Y. Obaid, S. Al-Thabaiti, S. N. Basahel, I. P. Parkin and C. J. Carmalt, *J. Mater. Chem.*

- A, 2014, **2**, 5108–5116.
- 83 P. Marchand, I. A. Hassan, I. P. Parkin and C. J. Carmalt, *Dalt. Trans.*, 2013, **42**, 9406.
- 84 C. R. Crick and I. P. Parkin, *J. Mater. Chem.*, 2011, **21**, 9362–9366.
- 85 A. Tombesi, S. Li, S. Sathasivam, K. Page, F. L. Heale, C. Pettinari, C. J. Carmalt and I. P. Parkin, *Sci. Rep.*, 2019, **9**, 1–12.
- 86 A. Zhuang, R. Liao, S. C. Dixon, Y. Lu, S. Sathasivam, I. P. Parkin and C. J. Carmalt, *RSC Adv.*, 2017, **7**, 29275–29283.
- 87 K. Vidal, E. Gómez, A. M. Goitandia, A. Angulo-Ibáñez and E. Aranzabe, *Coatings*, 2019, **9**, 627.
- 88 A. B. Gurav, Q. Xu, S. S. Latthe, R. S. Vhatkar, S. Liu, H. Yoon and S. S. Yoon, *Ceram. Int.*, 2015, **41**, 3017–3023.
- 89 Z. H. Zhang, H. J. Wang, Y. H. Liang, X. J. Li, L. Q. Ren, Z. Q. Cui and C. Luo, *Sci. Rep.*, , DOI:10.1038/s41598-018-22241-9.
- 90 Z. Janjua, F. Xu, K.-S. Choi, B. Turnbull, J. Liu, X. Hou and M. Roe, *Nanomaterials*, 2016, **6**, 232.
- 91 S. Nagappan, J. J. Park, S. S. Park and C.-S. Ha, *Nano Converg.*, 2014, **1**, 30.
- 92 Y. Zhang, B. Dong, S. Wang, L. Zhao, L. Wan and E. Wang, *RSC Adv.*, 2017, **7**, 47357–47365.
- 93 M. Long, S. Peng, W. Deng, X. Yang, K. Miao, N. Wen, X. Miao and W. Deng, *J. Colloid Interface Sci.*, 2017, **508**, 18–27.

- 94 L. Xu, R. G. Karunakaran, J. Guo and S. Yang, *ACS Appl. Mater. Interfaces*, 2012, **4**, 1118–1125.
- 95 A. Steele, I. Bayer and E. Loth, *Nano Lett.*, 2009, **9**, 501–505.
- 96 N. K. Neelakantan, P. B. Weisensee, J. W. Overcash, E. J. Torrealba, W. P. King and K. S. Suslick, *RSC Adv.*, 2015, **5**, 69243–69250.
- 97 S. A. Mahadik, D. B. Mahadik, M. S. Kavale, V. G. Parale, P. B. Wagh, H. C. Barshilia, S. C. Gupta, N. D. Hegde and A. V. Rao, *J. Sol-Gel Sci. Technol.*, 2012, **63**, 580–586.
- 98 J. Puetz and M. A. Aegerter, in *Sol-Gel Technologies for Glass Producers and Users*, Springer US, 2004, pp. 37–48.
- 99 M. Thieme, F. Streller, F. Simon, R. Frenzel and A. J. White, *Appl. Surf. Sci.*, 2013, **283**, 1041–1050.
- 100 A. M. Coclite, Y. Shi and K. K. Gleason, *Phys. Procedia*, 2013, **46**, 56–61.
- 101 J. Huang, S. Lyu, F. Fu, H. Chang and S. Wang, *RSC Adv.*, 2016, **6**, 106194–106200.
- 102 A. Berard, G. S. Patience, G. Chouinard and J. R. Tavares, *Sci. Rep.*, 2016, **6**, 1–10.
- 103 M. M. Aljumaily, M. A. Alsaadi, R. Das, S. B. Abd Hamid, N. A. Hashim, M. K. AlOmar, H. M. Alayan, M. Novikov, Q. F. Alsahy and M. A. Hashim, *Sci. Rep.*, 2018, **8**, 1–12.
- 104 J. Yong, F. Chen, Q. Yang and X. Hou, *Soft Matter*, 2015, **11**, 8897–8906.
- 105 J. Ryu, K. Kim, J. Y. Park, B. G. Hwang, Y. C. Ko, H. J. Kim, J. S. Han, E.

- R. Seo, Y. J. Park and S. J. Lee, *Sci. Rep.*, , DOI:10.1038/s41598-017-02108-1.
- 106 M. Hsiao, K. Y. Chen and C. Y. Chen, *Sci. Rep.*, , DOI:10.1038/s41598-018-37853-4.
- 107 C. Du, X. He, F. Tian, X. Bai and C. Yuan, *coatings*, 2019, **9**, 1–10.
- 108 Z. Wei, D. Jiang, J. Chen and X. Guo, *Mater. Lett.*, 2017, **196**, 115–118.
- 109 Z. Zhang, B. Ge, X. Men and Y. Li, *Colloids Surfaces A Physicochem. Eng. Asp.*, 2016, **490**, 182–188.
- 110 A. Kumar and B. Gogoi, *Tribol. Int.*, 2018, **122**, 114–118.
- 111 X. Zhang, J. Zhao, J. Mo, R. Sun, Z. Li and Z. Guo, *Colloids Surfaces A Physicochem. Eng. Asp.*, 2019, **567**, 205–212.
- 112 A. Esmailirad, M. V. Rukosuyev, M. B. G. Jun and F. C. J. M. van Veggel, *Surf. Coatings Technol.*, 2016, **285**, 227–234.
- 113 W. Ye, Q. Shi, J. Hou, J. Jin, Q. Fan, S. C. Wong, X. Xu and J. Yin, *J. Mater. Chem. B*, 2014, **2**, 7186–7191.
- 114 Y. Wang, Y. Zhu, C. Zhang, J. Li and Z. Guan, *ACS Appl. Mater. Interfaces*, 2017, **9**, 4142–4150.
- 115 L. Xu, D. Zhu, X. Lu and Q. Lu, *J. Mater. Chem. A*, 2015, **3**, 3801–3807.
- 116 D. Lv, L. Sheng, J. Wan, J. Dong, H. Ouyang, H. Jiao and J. Liu, *Polym. Chem.*, 2019, **10**, 331–335.
- 117 F. L. Heale, M. Einhorn, K. Page, I. P. Parkin and C. J. Carmalt, *RSC Adv.*, 2019, **9**, 20332–20340.

- 118 F. L. Heale, K. Page, J. S. Wixey, P. Taylor, I. P. Parkin and C. J. Carmalt, *RSC Adv.*, 2018, **8**, 27064–27072.
- 119 Z. He, M. Ma, X. Lan, F. Chen, K. Wang, H. Deng, Q. Zhang and Q. Fu, *Soft Matter*, 2011, **7**, 6435–6443.
- 120 J.-D. Brassard, D. K. Sarkar and J. Perron, *Appl. Sci.*, 2012, **2**, 453–464.
- 121 D. Wang, Q. Sun, M. J. Hokkanen, C. Zhang, F. Y. Lin, Q. Liu, S. P. Zhu, T. Zhou, Q. Chang, B. He, Q. Zhou, L. Chen, Z. Wang, R. H. A. Ras and X. Deng, *Nature*, 2020, **582**, 55–59.
- 122 Q. Zhu, B. Li, S. Li, G. Luo, B. Zheng and J. Zhang, *Sci. Rep.*, 2019, **9**, 1–12.
- 123 F. Wang, Y. Zhou, W. Yang, M. Ni, X. Zhang and C. Liang, *Appl. Therm. Eng.*, 2020, **169**, 114967.
- 124 T. He, X. Chen, Y. Wang, Z. Cheng, Y. Liu, X. Wang, L. Luo, Y. Chen and X. Liu, *Appl. Surf. Sci.*, 2020, **515**, 146006.
- 125 J. Yang, J. Li, P. Xu and B. Chen, *J. Sol-Gel Sci. Technol.*, 2020, **93**, 79–90.
- 126 E. Lee and K. H. Lee, *Sci. Rep.*, 2018, **8**, 4101.
- 127 Y. Zhang, J. Li, F. Huang, S. Li, Y. Shen, A. Xie, W. Duan and F. Wang, *Appl. Phys. A Mater. Sci. Process.*, 2013, **110**, 397–401.
- 128 P. Zhang, S. Dong, B. Li, X. Wei and J. Zhang, *Appl. Clay Sci.*, 2018, **157**, 237–247.
- 129 D. Sriramulu, E. L. Reed, M. Annamalai, T. V. Venkatesan and S.

- Valiyaveettil, *Sci. Rep.*, 2016, **6**, 35993.
- 130 M. Z. Khan, V. Baheti, J. Militky, A. Ali and M. Vikova, *Carbohydr. Polym.*, 2018, **202**, 571–580.
- 131 S. Li, K. Page, S. Sathasivam, F. Heale, G. He, Y. Lu, Y. Lai, G. Chen, C. J. Carmalt and I. P. Parkin, *J. Mater. Chem. A*, 2018, **6**, 17633–17641.
- 132 W. Bai, H. Lin, K. Chen, J. Xu, J. Chen, X. Zhang, R. Zeng, J. Lin and Y. Xu, *Sep. Purif. Technol.*, 2020, **253**, 117545.
- 133 J. Lyu, B. Wu, N. Wu, C. Peng, J. Yang, Y. Meng and S. Xing, *Chem. Eng. J.*, 2021, **404**, 126456.
- 134 Y. Teng, Y. Wang, B. Shi, X. Li and Y. Chen, *Polym. Test.*, 2020, **91**, 106810.
- 135 P. Bandi, V. M. K, S. Kausley and B. Rai, *Mater. Today Commun.*, 2020, **25**, 101625.
- 136 S. Barthwal and S.-H. Lim, *J. Memb. Sci.*, 2020, 118716.
- 137 X. Gong, L. Zhang, S. He, S. Jiang, W. Wang and Y. Wu, *Mater. Des.*, 2020, **196**, 109112.
- 138 B. Majhy, R. Iqbal and A. K. Sen, *Sci. Rep.*, 2018, **8**, 18018.
- 139 B. Thasma Subramanian, J. P. Alla, J. S. Essomba and N. F. Nishter, *J. Clean. Prod.*, 2020, **256**, 120693.
- 140 S. S. Chhatre, J. O. Guardado, B. M. Moore, T. S. Haddad, J. M. Mabry, G. H. McKinley and R. E. Cohen, *ACS Appl. Mater. Interfaces*, 2010, **2**, 3544–3554.

- 141 A. Halpern, *J. Phys. Colloid Chem.*, 1949, **53**, 895–897.
- 142 Y. Wu, J. Zeng, Y. Si, M. Chen and L. Wu, *ACS Nano*, 2018, **12**, 10338–10346.
- 143 C. R. Crick, J. C. Bear, A. Kafizas and I. P. Parkin, *Adv. Mater.*, 2012, **24**, 3505–3508.
- 144 C. Liu, L. Zhu, W. Bu and Y. Liang, *Micron*, 2018, **107**, 94–100.
- 145 Y. Lin, H. Chen, G. Wang and A. Liu, *Coatings*, , DOI:10.3390/coatings8060208.
- 146 M. J. Kreder, J. Alvarenga, P. Kim and J. Aizenberg, *Nat. Rev. Mater.*, 2016, 1.
- 147 F. Piscitelli, A. Chiariello, D. Dabkowski, G. Corrado, F. Marra and L. Di Palma, *Aerospace*, 2020, **7**, 2.
- 148 A. M. A. Mohamed, A. M. Abdullah and N. A. Younan, *Arab. J. Chem.*, 2015, 8, 749–765.
- 149 R. Sharafudeen, in *Advances in Smart Coatings and Thin Films for Future Industrial and Biomedical Engineering Applications*, Elsevier, 2020, pp. 515–534.
- 150 N. Wang, D. Xiong, Y. Deng, Y. Shi and K. Wang, *ACS Appl. Mater. Interfaces*, 2015, **7**, 6260–6272.
- 151 P. Bi, H. Li, G. Zhao, M. Ran, L. Cao, H. Guo and Y. Xue, *Coatings*, 2019, **9**, 452.
- 152 Y. Shen, Z. Wu, J. Tao, Z. Jia, H. Chen, S. Liu, J. Jiang and Z. Wang,

- ACS Appl. Mater. Interfaces*, 2020, **12**, 25484–25493.
- 153 T. Ren, G. Tang, B. Yuan, Z. Yan, L. Ma and X. Huang, *Surf. Coatings Technol.*, 2019, **380**, 125086.
- 154 C. Wang, F. Tang, Q. Li, Y. Zhang and X. Wang, *Colloids Surfaces A Physicochem. Eng. Asp.*, 2017, **514**, 236–242.
- 155 B. K. Tudu, A. Kumar and B. Bhushan, *Philos. Trans. R. Soc. A Math. Phys. Eng. Sci.*, , DOI:10.1098/rsta.2018.0272.
- 156 E. Taghvaei, A. Moosavi, A. Nouri-Borujerdi, M. A. Daeian and S. Vafaeinejad, *Energy*, 2017, **125**, 1–10.
- 157 N. Wang, L. Tang, Y. Cai, W. Tong and D. Xiong, *Colloids Surfaces A Physicochem. Eng. Asp.*, 2018, **555**, 290–295.
- 158 K. Zheng, J. Zhang, H. Dodiuk, S. Kenig, C. Barry, H. Sun and J. Mead, *ACS Appl. Polym. Mater.*, 2020, **2**, 1614–1622.
- 159 N. R. Geraldi, L. E. Dodd, B. B. Xu, G. G. Wells, D. Wood, M. I. Newton and G. McHale, *Surf. Topogr. Metrol. Prop.*, 2017, **5**, 034001.
- 160 U. Eduok, J. Szpunar and E. Ebenso, in *Superhydrophobic Polymer Coatings*, Elsevier, 2019, pp. 245–279.
- 161 R. Tan, H. Xie, J. She, J. Liang, H. He, J. Li, Z. Fan and B. Liu, *Carbon N. Y.*, 2019, **145**, 359–366.
- 162 Q. Cheng, D. Cao, X. Liu, Y. Zheng, Z. Shi, S. Zhu and Z. Cui, *J. Mech. Behav. Biomed. Mater.*, 2019, **98**, 148–156.
- 163 S. Liu, J. Zheng, L. Hao, Y. Yegin, M. Bae, B. Ulugun, T. M. Taylor, E. A.

- Scholar, L. Cisneros-Zevallos, J. K. Oh and M. Akbulut, *ACS Appl. Mater. Interfaces*, 2020, 12, 21311–21321.
- 164 M. S. Selim, H. Yang, S. A. El-Safty, N. A. Fatthallah, M. A. Shenashen, F. Q. Wang and Y. Huang, *Colloids Surfaces A Physicochem. Eng. Asp.*, 2019, **570**, 518–530.
- 165 S. S. Latthe, R. S. Sutar, A. K. Bhosale, K. K. Sadasivuni and S. Liu, in *Superhydrophobic Polymer Coatings*, Elsevier, 2019, pp. 339–356.
- 166 U. Baig, A. Matin, M. A. Gondal and S. M. Zubair, *J. Clean. Prod.*, 2019, **208**, 904–915.
- 167 A. Xie, Y. Chen, J. Cui, J. Lang, C. Li, Y. Yan and J. Dai, *Colloids Surfaces A Physicochem. Eng. Asp.*, 2019, **563**, 120–129.
- 168 M. Khosravi, S. Azizian and R. Boukherroub, *Sep. Purif. Technol.*, 2019, **215**, 573–581.
- 169 S. Martin and B. Bhushan, *J. Colloid Interface Sci.*, 2017, **488**, 118–126.
- 170 J. Zhang, B. Feng Chen, B. Qing Yang, B. Jiale Yong, B. Jinglan Huo, Y. Fang and B. Xun Hou, *Appl. Phys. A*, , DOI:10.1007/s00339-017-1195-8.
- 171 D. Aslanidou, I. Karapanagiotis and D. Lampakis, *Materials (Basel)*, , DOI:10.3390/ma11040585.
- 172 Y. Zhang, Z. Xiao, C. Liu and X. Yu, *Soft Matter*, 2019, **15**, 7374–7380.
- 173 M. Liu, Y. Hou, J. Li, L. Tie and Z. Guo, *Colloids Surfaces A Physicochem. Eng. Asp.*, 2018, **553**, 645–651.
- 174 A. Moiz, R. Padhye and X. Wang, *Coatings*, 2018, **8**, 104.

- 175 R. Das, Z. Ahmad, J. Nauruzbayeva and H. Mishra, *Sci. Rep.*, 2020, **10**, 1–12.
- 176 A. K. Kota, G. Kwon and A. Tuteja, *NPG Asia Mater.*, 2014, 6, 109.
- 177 T. Liu and C. J. Kim, *Science (80-.)*, 2014, **346**, 1096–1100.
- 178 M. Nosonovsky and B. Bhushan, *Philos. Trans. R. Soc. A Math. Phys. Eng. Sci.*, 2016, **374**, 20160185.
- 179 J. Dong and J. Zhang, *Sci. Rep.*, 2018, **8**, 1–12.
- 180 J. Yong, F. Chen, Q. Yang, J. Huo and X. Hou, *Chem. Soc. Rev.*, 2017, 46, 4168–4217.
- 181 Y. Cao, A. Salvini and M. Camaiti, *Coatings*, 2020, **10**, 1–23.
- 182 J. Cui, Q. Wang, A. Xie, J. Lang, Z. Zhou and Y. Yan, *J. Taiwan Inst. Chem. Eng.*, 2019, **104**, 240–249.
- 183 W. Bigui, Y. Cheng, L. Jianlin, W. Gang, D. Liang, S. Xiaosan, W. Fuping, L. Hua and C. Qing, *Sep. Purif. Technol.*, 2019, **229**, 115808.
- 184 H. Li, Y. Yin, L. Zhu, Y. Xiong, X. Li, T. Guo, W. Xing and Q. Xue, *J. Hazard. Mater.*, 2019, **373**, 725–732.
- 185 C. Chen and B. Chen, *Sci. Total Environ.*, 2019, **696**, 133777.
- 186 L. Tian, W. Li, H. Ye, L. Zhu, H. Chen and H. Liu, *Surf. Coatings Technol.*, 2019, **377**, 124892.
- 187 A. Mehmood, H. Ghafar, S. Yaqoob, U. F. Gohar and B. Ahmad, *J. Dev. Drugs*, , DOI:10.4172/2329-6631.1000174.

- 188 L. Baù, B. Bártová, M. Arduini and F. Mancin, *Chem. Commun.*, 2009, 7584–7586.
- 189 S. Chantarak, J. Chang, S. Suwanboon and S. Riyajan, *J. Porous Mater.*, 2018, **25**, 1391–1399.
- 190 A. Bayu, D. Nandiyanto, S.-G. Kim and K. Okuyama, *Microporous Mesoporous Mater.*, 2009, **120**, 447–453.
- 191 D. W. Lee, M. H. Jin, J. H. Park, Y. J. Lee, Y. C. Choi, J. Chan Park and D. H. Chun, *ACS Sustain. Chem. Eng.*, 2018, **6**, 12241–12250.
- 192 N. I. Vazquez, Z. Gonzalez, B. Ferrari and Y. Castro, *Bol. la Soc. Esp. Ceram. y Vidr.*, 2017, **56**, 139–145.
- 193 R. Narayan, U. Y. Nayak, A. M. Raichur and S. Garg, *Pharmaceutics*, 2018, **10**, 1–49.
- 194 I. A. Rahman and V. Padavettan, *J. Nanomater.*, , DOI:10.1155/2012/132424.
- 195 S. H. Wu and H. P. Lin, *Chem. Soc. Rev.*, 2013, **42**, 3862–3875.
- 196 M. M. Ayad, N. L. Torad, I. M. Minisy, R. Izriq and E. Z. M. Ebeid, *J. Porous Mater.*, 2019, **26**, 1731–1741.
- 197 E. J. Park, Y. K. Cho, D. H. Kim, M. G. Jeong, Y. H. Kim and Y. D. Kim, *Langmuir*, 2014, **30**, 10256–10262.
- 198 A. B. D. Nandiyanto, S. G. Kim, F. Iskandar and K. Okuyama, *Microporous Mesoporous Mater.*, 2009, **120**, 447–453.
- 199 F. Sancenõn, L. Pascual, M. Oroval, E. Aznar and R. Martínez-Máñez,

ChemistryOpen, 2015, **4**, 418–437.

- 200 Y. J. Yu, J. L. Xing, J. L. Pang, S. H. Jiang, K. F. Lam, T. Q. Yang, Q. S. Xue, K. Zhang and P. Wu, *ACS Appl. Mater. Interfaces*, 2014, **6**, 22655–22665.
- 201 M. Eslami, M. G. Dekamin, L. Motlagh and A. Maleki, *Green Chem. Lett. Rev.*, 2018, **11**, 36–46.
- 202 M. S. Jang, T. N. Phan, I. S. Chung, I. G. Lee, Y. K. Park and C. H. Ko, *Res. Chem. Intermed.*, 2018, **44**, 3723–3735.
- 203 S. O. Ribeiro, C. M. Granadeiro, M. C. Corvo, J. Pires, J. M. Campos-Martin, B. de Castro and S. S. Balula, *Front. Chem.*, 2019, **7**, 1–13.
- 204 W. Stober and A. Fink, *J. Colloid Interface Sci.*, 1968, **26**, 62–69.
- 205 Z. Chen, B. Peng, J. Q. Xu, X. C. Xiang, D. F. Ren, T. Q. Yang, S. Y. Ma, K. Zhang and Q. M. Chen, *Nanoscale*, 2020, **12**, 3657–3662.
- 206 S. Chen, P. Wang, G. Fan, S. Liao, H. Si and Z. Wang, *PLoS One*, , DOI:10.1371/journal.pone.0216117.
- 207 T. Suteewong, H. Sai, M. Bradbury, L. A. Estroff, S. M. Gruner and U. Wiesner, *Chem. Mater.*, 2012, **24**, 3895–3905.
- 208 L. Luo, Y. Liang, E. S. Erichsen and R. Anwender, *J. Colloid Interface Sci.*, 2017, **495**, 84–93.
- 209 Y. K. Oh, L. Y. Hong, Y. Asthana and D. P. Kim, *J. Ind. Eng. Chem.*, 2006, **12**, 911–917.
- 210 J. Chun, Y. Mo Gu, J. Hwang, K. K. Oh and J. H. Lee, *J. Ind. Eng. Chem.*,

- 2020, **81**, 135–143.
- 211 J. young Kim, K. W. Park and O. Y. Kwon, *Microporous Mesoporous Mater.*, 2019, **285**, 137–141.
- 212 H. El-Didamony, E. El-Fadaly, A. A. Amer and I. H. Abazeed, *Bol. la Soc. Esp. Ceram. y Vidr.*, 2020, **59**, 31–43.
- 213 I. M. Joni, Rukiah and C. Panatarani, in *3RD INTERNATIONAL CONFERENCE ON CONDENSED MATTER AND APPLIED PHYSICS (ICC-2019)*, 2020, vol. 2220, p. 080018.
- 214 C. Chapa-González, A. L. Piñón-Urbina and P. E. García-Casillas, *Materials (Basel)*, , DOI:10.3390/ma11040510.
- 215 B. Purnawira, H. Purwaningsih, Y. Ervianto, V. M. Pratiwi, D. Susanti, R. Rochiem and A. Purniawan, *IOP Conf. Ser. Mater. Sci. Eng.*, , DOI:10.1088/1757-899X/541/1/012018.
- 216 U. Zulfiqar, T. Subhani and S. W. Husain, *J. Asian Ceram. Soc.*, 2016, **4**, 91–96.
- 217 X. Wang, Y. Zhang, W. Luo, A. A. Elzatahry, X. Cheng, A. Alghamdi, A. M. Abdullah, Y. Deng and D. Zhao, *Chem. Mater.*, 2016, **28**, 2356–2362.
- 218 W. D. Xiang, Y. X. Yang, J. L. Zheng, L. Cao, H. J. Ding and X. N. Liu, *Mater. Sci. Pol.*, 2010, **28**, 709–730.
- 219 T. Yokoi and T. Tatsumi, *J. Japan Pet. Inst.*, 2007, **50**, 299–311.
- 220 K. W. Park, J. Y. Kim, H. J. Seo and O. Y. Kwon, *Sci. Rep.*, 2019, **9**, 1–8.
- 221 V. Rizzi, E. A. Prasetyanto, P. Chen, J. Gubitosa, P. Fini, A. Agostiano, L.

- De Cola and P. Cosma, *J. Mol. Liq.*, 2019, **273**, 435–446.
- 222 M. Park and S. Huh, *Mater. Lett.*, 2019, **243**, 30–33.
- 223 L. Travaglini, P. Picchetti, A. Del Giudice, L. Galantini and L. De Cola, *Microporous Mesoporous Mater.*, 2019, **279**, 423–431.
- 224 C. Gao, Y. Sakamoto, K. Sakamoto, O. Terasaki and S. Che, *Angew. Chemie - Int. Ed.*, 2006, **45**, 4295–4298.
- 225 F. Gai, T. Zhou, G. Chu, Y. Li, Y. Liu, Q. Huo and F. Akhtar, *Dalt. Trans.*, 2016, **45**, 508–514.
- 226 H. Li, J. Ke, H. Li, C. Wei, X. Wu, J. Li, Y. Yang, L. Xu, H. Liu, S. Li, M. Yang and M. Wei, *Mater. Sci. Eng. C*, 2018, **93**, 407–418.
- 227 W. Jia, H. Xu, Q. Yang, S. Ren and J. Wang, *J. Dispers. Sci. Technol.*, 2019, **40**, 1664–1674.
- 228 N. Chandra and V. K. Tyagi, *J. Dispers. Sci. Technol.*, 2013, **34**, 800–808.
- 229 B. Fotoohi, M. Kazemzad and L. Mercier, *Ceram. Int.*, 2018, **44**, 20199–20210.
- 230 T. M. Albayati, I. K. Salih and H. F. Alazzawi, *Heliyon*, 2019, **5**, e02539.
- 231 L. dos S. Andrade, B. Castanheira and S. Brochsztain, *Microporous Mesoporous Mater.*, 2020, **294**, 109909.
- 232 A. Ijaz, M. B. Yagci, C. W. Ow-yang, A. L. Demirel and A. Mikó, *Microporous Mesoporous Mater.*, 2020, 110240.
- 233 J. Wang, W. Xiao, J. Wang, J. Lu and J. Yang, *Mater. Lett.*, 2015, **142**, 269–272.

- 234 L. Wu, H. Zhang, M. Wu, Y. Zhong, X. Liu and Z. Jiao, *Microporous Mesoporous Mater.*, 2016, **228**, 318–328.
- 235 J. H. Kim, J. K. Kang, S. C. Lee and S. B. Kim, *J. Taiwan Inst. Chem. Eng.*, 2018, **87**, 140–149.
- 236 J. K. Kang and S. B. Kim, *Microporous Mesoporous Mater.*, 2020, **295**, 109967.
- 237 Y. Guo, L. Wu, K. Gou, Y. Wang, B. Hu, Y. Pang, S. Li and H. Li, *Microporous Mesoporous Mater.*, 2020, **294**, 109862.
- 238 L. Travaglini and L. De Cola, *Chem. Mater.*, 2018, **30**, 4168–4175.
- 239 Y. Jiang, W. Sun, L. Zhou, L. Ma, Y. He and J. Gao, *Appl. Biochem. Biotechnol.*, 2016, **179**, 1155–1169.
- 240 E. Elimbinzi, S. S. Nyandoro, E. B. Mubofu, J. C. Manayil, A. F. Lee and K. Wilson, *Microporous Mesoporous Mater.*, 2020, **294**, 109868.
- 241 N. Koike, W. Chaikittisilp, A. Shimojima and T. Okubo, *RSC Adv.*, 2016, **6**, 90435–90445.
- 242 X. Zuo, Y. Xia, Q. Ji, X. Gao, S. Yin, M. Wang, X. Wang, B. Qiu, A. Wei, Z. Sun, Z. Liu, J. Zhu and Y. J. Cheng, *ACS Nano*, 2017, **11**, 889–899.
- 243 P. Singh, S. Srivastava and S. K. Singh, *ACS Biomater. Sci. Eng.*, 2019, **5**, 4882–4898.
- 244 C. J. Reader and M. Nargiello, *CoatingsTech*, 2020, **17**, 1–9.
- 245 S. Azarshin, J. Moghadasi and Z. A. Aboosadi, *Energy Explor. Exploit.*, 2017, **35**, 685–697.

- 246 M. C. Gomes, A. Cunha, T. Trindade and J. P. C Tom, *J. Innov. Opt. Health Sci.*, 2016, **9**, 1630005.
- 247 G. Anbalagan, A. R. Prabakaran and S. Gunasekaran, *J. Appl. Spectrosc.*, 2010, **77**, 86–94.
- 248 J. Trébosc, J. W. Wiench, S. Huh, V. S. Y. Lin and M. Pruski, *J. Am. Chem. Soc.*, 2005, **127**, 3057–3068.
- 249 L. Ejenstam, A. Swerin and P. M. Claesson, *J. Dispers. Sci. Technol.*, 2016, **37**, 1375–1383.
- 250 G. Li, Z. Li, L. Lu, L. Xue and C. Deng, *J. Wuhan Univ. Technol. Mater. Sci. Ed.*, 2012, **27**, 138–141.
- 251 A. Sabbah, A. Youssef and P. Damman, *Appl. Sci.*, 2016, **6**, 152.
- 252 U. Eduok, O. Faye and J. Szpunar, *Prog. Org. Coatings*, 2017, 111, 124–163.
- 253 S. R. Yadhuraj, S. Babu Gandla, B. G. Sudarshan and S. C. Prasanna Kumar, *Mater. Today Proc.*, 2018, **5**, 21406–21412.
- 254 A. Victor, J. Ribeiro and F. F. Araújo, *J. Mech. Eng. Biomech.*, 2019, **4**, 1–9.
- 255 D. Zhu, S. Handschuh-Wang and X. Zhou, *J. Mater. Chem. A*, 2017, **5**, 16467–16497.
- 256 L. Xiong, P. Chen and Q. Zhou, *J. Adhes. Sci. Technol.*, 2014, **28**, 1046–1054.
- 257 Z. Luo, Y. Li, C. Duan and B. Wang, *RSC Adv.*, 2018, **8**, 16251–16259.

- 258 J. Carlos Almeida, A. G. B. Castro, I. M. Miranda Salvado, F. M. A. Margaça and M. H. Vaz Fernandes, *Mater. Lett.*, 2014, **128**, 105–109.
- 259 E. J. Park, J. K. Sim, M. G. Jeong, H. O. Seo and Y. D. Kim, *RSC Adv.*, 2013, **3**, 12571–12576.
- 260 Y. T. Lin and J. H. Chou, *J. Adhes. Sci. Technol.*, 2016, **30**, 1310–1318.
- 261 Q. Lu, Michigan Technological University, 2013.
- 262 M. S. Selim, M. A. Shenashen, A. Elmarakbi, N. A. Fatthallah, S. ichi Hasegawa and S. A. El- Safty, *Chem. Eng. J.*, 2017, **320**, 653–666.
- 263 S. Martin and B. Bhushan, *J. Colloid Interface Sci.*, 2017, **488**, 118–126.
- 264 S. Krishnan, C. J. Weinman and C. K. Ober, *J. Mater. Chem.*, 2008, **18**, 3405–3413.
- 265 J. Liu, G. Zong, L. He, Y. Zhang, C. Liu and L. Wang, *Micromachines*, 2015, **6**, 855–864.
- 266 C. Sanchez, B. Julián, P. Belleville and M. Popall, *J. Mater. Chem.*, 2005, **15**, 3559–3592.
- 267 S. Parola, B. Julián-López, L. D. Carlos and C. Sanchez, *Adv. Funct. Mater.*, 2016, **26**, 6506–6544.
- 268 T. Bardelli, C. Marano and F. Briatico Vangosa, *J. Appl. Polym. Sci.*, 2021, **138**, 51013.
- 269 S. Mani, P. Cassagnau, M. Bousmina and P. Chaumont, *Macromolecules*, 2009, **42**, 8460–8467.
- 270 Lequynh, *Wacker Chemie AG*, 2018, 105.

- 271 J. Y. Park, *Science (80-.)*, 2018, **361**, 753.
- 272 Q. F. Xu, Y. Liu, F. J. Lin, B. Mondal and A. M. Lyons, *ACS Appl. Mater. Interfaces*, 2013, **5**, 8915–8924.
- 273 J. B. Chemin, S. Bulou, K. Baba, C. Fontaine, T. Sindzingre, N. D. Boscher and P. Choquet, *Sci. Rep.*, 2018, **8**, 9603.
- 274 Y. Liu, J. Li, X. Qiu and C. Burda, in *Water Science and Technology*, 2006, vol. 54, pp. 47–54.
- 275 M. J. Wu, T. Bak, P. J. O'Doherty, M. C. Moffitt, J. Nowotny, T. D. Bailey and C. Kersaitis, *Int. J. Photochem.*, 2014, **2014**, 1–9.
- 276 Q. Wen, J. Di, Y. Zhao, Y. Wang, L. Jiang and J. Yu, *Chem. Sci.*, 2013, **4**, 4378–4382.
- 277 H. Kang, Y. Liu, H. Lai, X. Yu, Z. Cheng and L. Jiang, *ACS Nano*, 2018, **12**, 1074–1082.
- 278 Y. Lu, S. Sathasivam, J. Song, C. R. Crick, C. J. Carmalt and I. P. Parkin, *Science (80-.)*, 2015, **347**, 1132–1135.
- 279 X. Zhang, Y. Guo, Z. Zhang and P. Zhang, *Appl. Surf. Sci.*, 2013, **284**, 319–323.
- 280 M. Castellote and N. Bengtsson, *Appl. Titan. Dioxide Photocatal. to Constr. Mater.*, 2011, 5–10.
- 281 B. Liu, H. Wu and I. P. Parkin, *ACS Omega*, 2020, **5**, 14847–14856.
- 282 M. Pawar, S. T. Sendoğdular and P. Gouma, *J. Nanomater.*, 2018, 2018.
- 283 Q. Guo, C. Zhou, Z. Ma and X. Yang, *Adv. Mater.*, 2019, **31**, 1901997.

- 284 V. Etacheri, C. Di Valentin, J. Schneider, D. Bahnemann and S. C. Pillai, *J. Photochem. Photobiol. C Photochem. Rev.*, 2015, **25**, 1–29.
- 285 C. Liao, Y. Li and S. C. Tjong, *Nanomaterials*, , DOI:10.3390/NANO10010124.
- 286 D. Gurera and B. Bhushan, *Philos. Trans. R. Soc. A*, , DOI:10.1098/RSTA.2018.0273.
- 287 S. Noormohammed and D. K. Sarkar, *Coatings 2021, Vol. 11, Page 432*, 2021, **11**, 432.
- 288 C. Han, J. Lalley, D. Namboodiri, K. Cromer and M. N. Nadagouda, *Curr. Opin. Chem. Eng.*, 2016, **11**, 46–51.
- 289 A. Bonfond, E. González, J. M. Asua, J. R. Leiza, E. Ieva, G. Brinati, S. Carella, A. Marrani, A. Veneroni, J. Kiwi, C. Pulgarin and S. Rtimi, *Crystals*, 2016, **6**, 1–13.
- 290 M. G. Méndez-Medrano, E. Kowalska, A. Lehoux, A. Herissan, B. Ohtani, S. Rau, C. Colbeau-Justin, J. L. Rodríguez-López and H. Remita, *J. Phys. Chem. C*, 2016, **120**, 25010–25022.
- 291 A. J. Haider, Z. N. Jameel and I. H. M. Al-Hussaini, *Energy Procedia*, 2019, **157**, 17–29.
- 292 X. Luo, Z. Zhu, Y. Tian, J. You and L. Jiang, *Catalysts*, 2021, **11**, 1–16.
- 293 M. Tu-Morn, N. Pairoh, W. Sutapun and T. Trongsatitkul, *Mater. Today Proc.*, 2019, **17**, 2048–2061.
- 294 R. E. Day, *Polym. Degrad. Stab.*, 1990, **29**, 73–92.

- 295 S. Alexander, J. Eastoe, A. M. Lord, F. Guittard and A. R. Barron, *ACS Appl. Mater. Interfaces*, 2016, **8**, 660–666.
- 296 P. Nguyen-tri, T. A. Nguyen, P. Carriere and C. N. Xuan, *Int. J. Corros.*, 2018, **2018**, 19.
- 297 X. Gong and S. He, *ACS Omega*, 2020, **5**, 4100–4108.
- 298 F. Li, M. Du, Z. Zheng, Y. Song and Q. Zheng, *Adv. Mater. Interfaces*, 2015, **2**, 1500201.
- 299 Q. Shang and Y. Zhou, *Ceram. Int.*, 2016, **42**, 8706–8712.
- 300 L. Xu and J. He, *Langmuir*, 2012, **28**, 7512–7518.
- 301 D. Zhi, H. Wang, D. Jiang, I. P. Parkin and X. Zhang, *RSC Adv.*, 2019, **9**, 12547–12554.
- 302 X. Zou, C. Tao, K. Yang, F. Yang, H. Lv, L. Yan, H. Yan, Y. Li, Y. Xie, X. Yuan and L. Zhang, *Appl. Surf. Sci.*, 2018, **440**, 700–711.
- 303 X. Zhang, P. Lan, Y. Lu, J. Li, H. Xu, J. Zhang, Y. Lee, J. Y. Rhee, K. L. Choy and W. Song, *ACS Appl. Mater. Interfaces*, 2014, **6**, 1415–1423.
- 304 X. Zhao, D. S. Park, J. Choi, S. Park, S. A. Soper and M. C. Murphy, *J. Colloid Interface Sci.*, 2020, **574**, 347–354.
- 305 X. Deng, L. Mammen, Y. Zhao, P. Lellig, K. Müllen, C. Li, H. J. Butt and D. Vollmer, *Adv. Mater.*, 2011, **23**, 2962–2965.
- 306 X. Zhao, Y. Li, B. Li, T. Hu, Y. Yang, L. Li and J. Zhang, *J. Colloid Interface Sci.*, 2019, **542**, 8–14.
- 307 I. S. Bayer, *Coatings*, , DOI:10.3390/coatings7010012.

- 308 S. A. Mahadik, M. S. Kavale, S. K. Mukherjee and A. V. Rao, *Appl. Surf. Sci.*, 2010, **257**, 333–339.
- 309 N. T. Vo, A. K. Patra and D. Kim, *Phys. Chem. Chem. Phys.*, 2017, **19**, 1937–1944.
- 310 S.-H. Wu, C.-Y. Mou and H.-P. Lin, *Chem. Soc. Rev.*, 2013, **42**, 3649–4258.
- 311 S. K. Warkhade, G. S. Gaikwad, S. P. Zodape, U. Pratap, A. V. Maldhure and A. V. Wankhade, *Mater. Sci. Semicond. Process.*, 2017, **63**, 18–24.
- 312 P. Nyamukamba, O. Okoh, H. Mungondori, R. Taziwa and S. Zinya, *Synthetic Methods for Titanium Dioxide Nanoparticles: A Review*, ItechOpen, London, 2018.
- 313 A. Król, P. Pomastowski, K. Rafińska, V. Railean-Plugaru and B. Buszewski, *Adv. Colloid Interface Sci.*, 2017, 249, 37–52.
- 314 Y. A. Selim, M. A. Azb, I. Ragab and M. H. M. Abd El-Azim, *Sci. Rep.*, 2020, **10**, 1–9.
- 315 G. Singh and S. P. Singh, in *3RD INTERNATIONAL CONFERENCE ON CONDENSED MATTER AND APPLIED PHYSICS (ICC-2019)*, AIP Publishing, 2020, vol. 2220, p. 020184.
- 316 M. Yu, L. Zhou, J. Zhang, P. Yuan, P. Thorn, W. Gu and C. Yu, *J. Colloid Interface Sci.*, 2012, **376**, 67–75.
- 317 J. Shabir, S. Rani, M. Sharma, C. Garkoti, Surabhi and S. Mozumdar, *RSC Adv.*, 2020, **10**, 8140–8151.

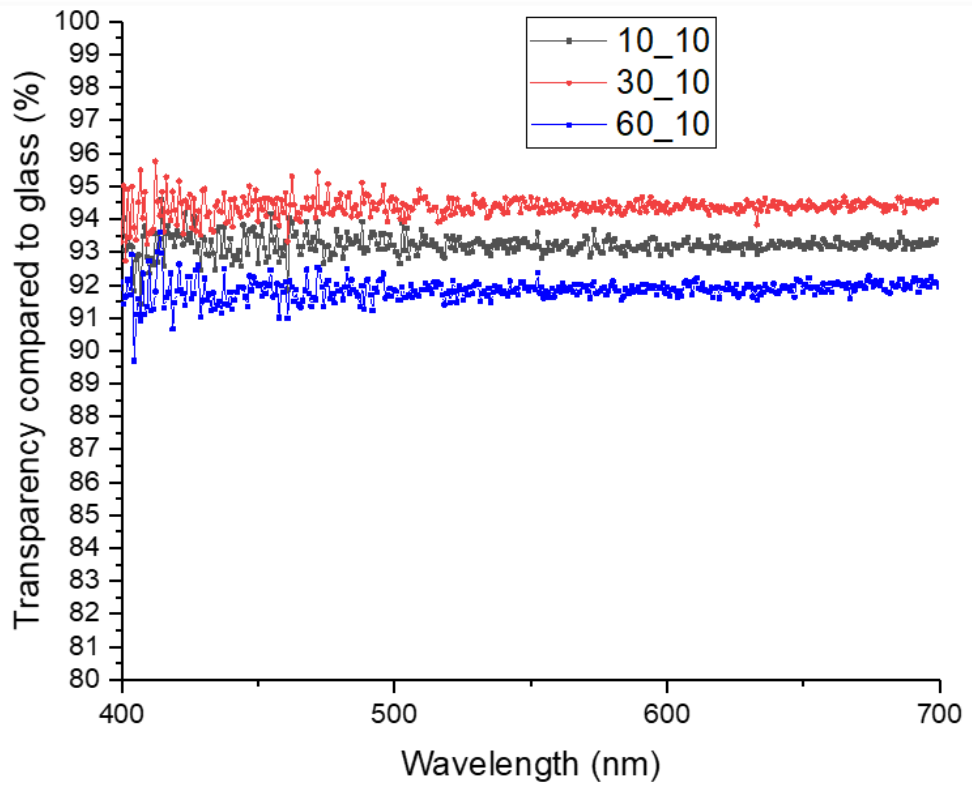
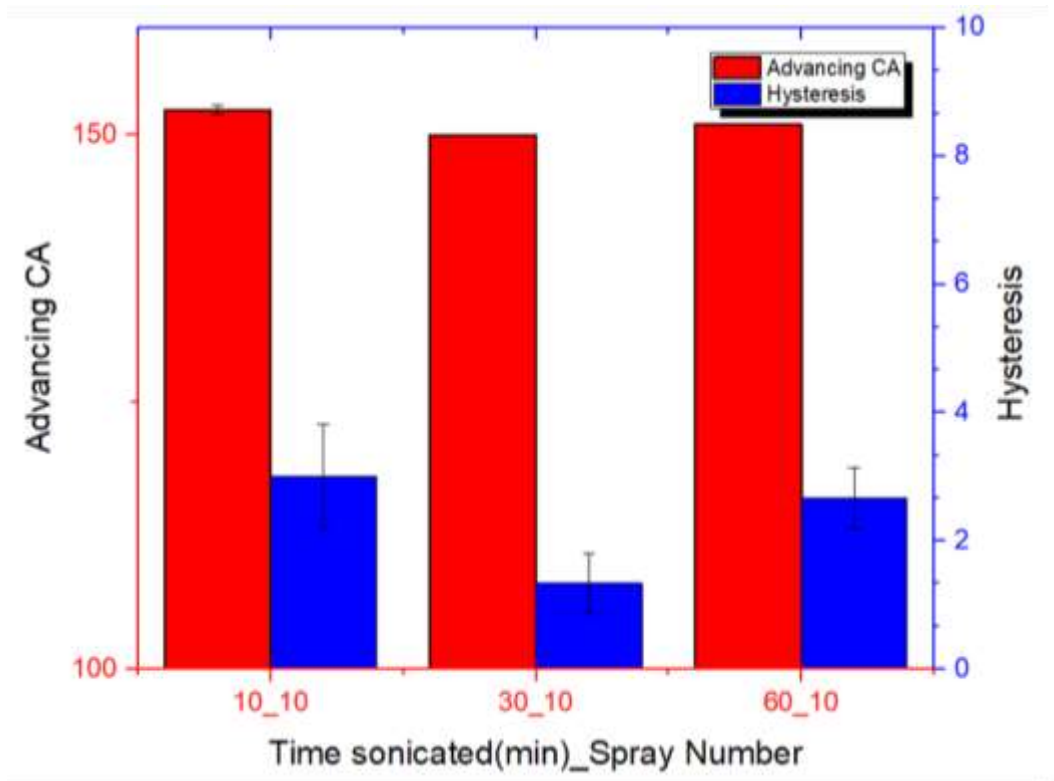
- 318 R. Jin, Z. Liu, Y. Bai, Y. Zhou and X. Chen, *ACS Omega*, 2018, **3**, 4306–4315.
- 319 V. Pareek, A. Bhargava, R. Gupta, N. Jain and J. Panwar, *Adv. Sci. Eng. Med.*, 2017, **9**, 527–544.
- 320 B. G. Trewyn, I. I. Slowing, S. Giri, H. T. Chen and V. S.-Y. Lin, *Acc. Chem. Res.*, 2007, **40**, 846–853.
- 321 Z. Zhang and P. C. Lin, in *Emerging Applications of Nanoparticles and Architectural Nanostructures: Current Prospects and Future Trends*, Elsevier Inc., 2018, pp. 177–233.
- 322 S. Yu, Z. Guo and W. Liu, *Chem. Commun.*, 2015, **51**, 1775–1794.
- 323 M. Luechinger, R. Prins and G. D. Pirngruber, *Microporous Mesoporous Mater.*, 2005, **85**, 111–118.
- 324 B. Sun, G. Zhou and H. Zhang, *Prog. Solid State Chem.*, 2016, **44**, 1–19.
- 325 C. M. Jimenez, Y. G. Rubio, V. Saunier, D. Warther, V. Stojanovic, L. Raehm, C. Frochot, P. Arnoux, M. Garcia, A. Morère, N. Bettache, M. Maynadier, P. Maillard, M. Gary-Bobo and J. O. Durand, *J. Sol-Gel Sci. Technol.*, 2016, **79**, 447–456.
- 326 Z. Yang, L. Wang, W. Sun, S. Li, T. Zhu, W. Liu and G. Liu, *Appl. Surf. Sci.*, 2017, **401**, 146–155.
- 327 Y. Rahmawan, L. Xu and S. Yang, *J. Mater. Chem. A*, 2013, **1**, 2955–2969.
- 328 E. Silla, A. Arnau, I. Tuñón, K. Nakanishi and G. Wypych, *Handb.*

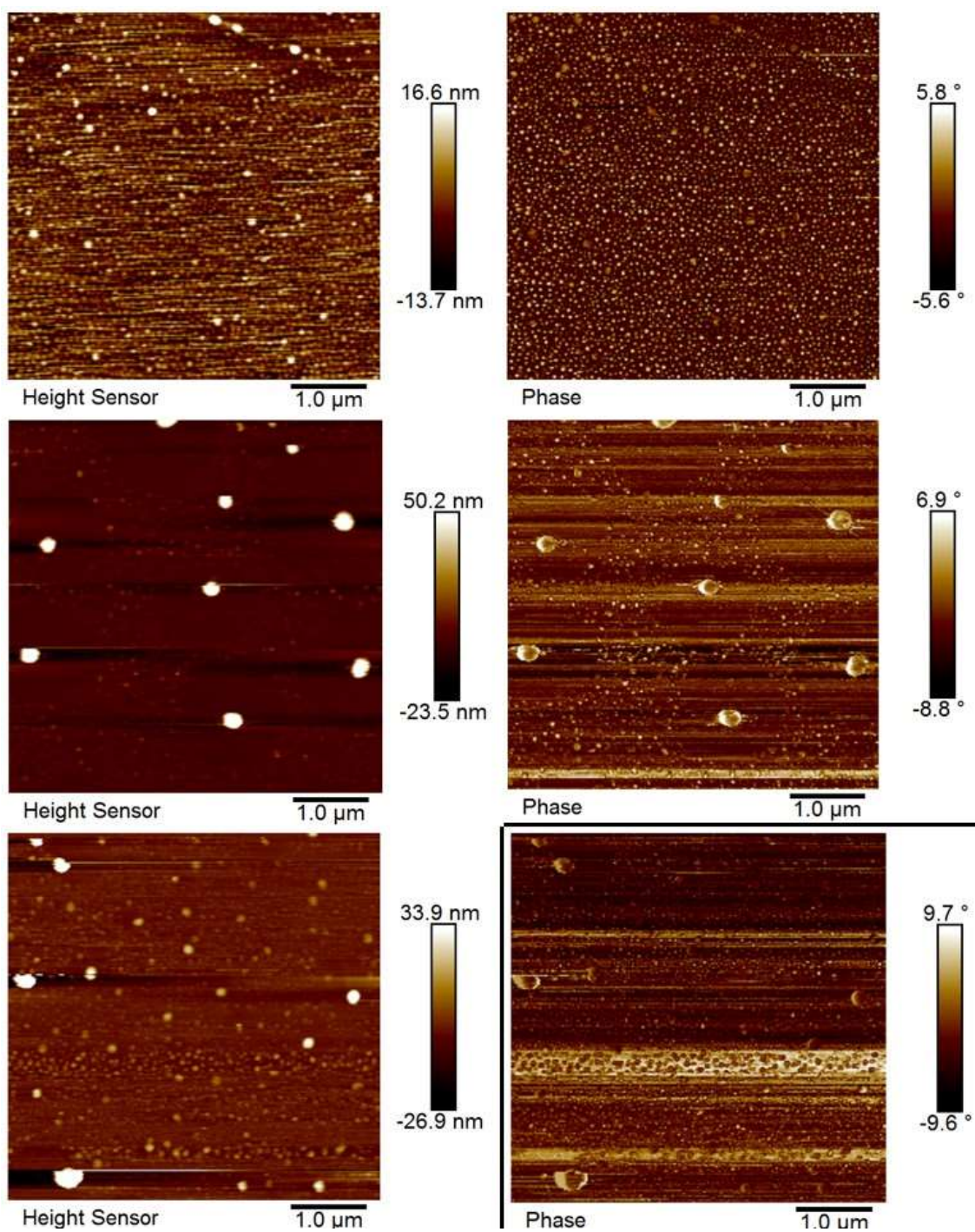
Solvents Second Ed., 2014, **1**, 11–72.

- 329 C. Meichner, A. E. Schedl, C. Neuber, K. Kreger, H. W. Schmidt and L. Kador, *AIP Adv.*, , DOI:10.1063/1.4928654.
- 330 S. Farmer, T. Druffel, E. A. Grulke, N. Mandzy, O. Buazza, M. Lattis and M. Spencer, *Nanophotonic Mater. V*, 2008, **7030**, 70300F.
- 331 I. Martinček, I. Turek and N. Tarjányi, *Opt. Mater. Express*, 2014, **4**, 1997.
- 332 A. Nakajima, K. Hashimoto, T. Watanabe, K. Takai, G. Yamauchi and A. Fujishima, *Langmuir*, 2000, **16**, 7044–7047.
- 333 K. Li, X. Zeng, H. Li, X. Lai and H. Xie, *Colloids Surfaces A Physicochem. Eng. Asp.*, 2014, **445**, 111–118.
- 334 M. Fox, *Optical Properties of Solids*, Oxford University Press, 1st edn., 2001.
- 335 R. P. Donovan and D. Leith, in *Particle Control for Semiconductor Manufacturing*, 2018, pp. 47–59.
- 336 R. B. Penndorf, *J. Opt. Soc. Am.*, 1957, **47**, 1010.
- 337 N. Suzuki, M. B. Zakaria, Y. D. Chiang, K. C. W. Wu and Y. Yamauchi, *Phys. Chem. Chem. Phys.*, 2012, **14**, 7427–7432.
- 338 K. Momma and F. Izumi, *J. Appl. Crystallogr.*, 2011, **44**, 1272–1276.
- 339 X. J. Guo, C. H. Xue, S. Sathasivam, K. Page, G. He, J. Guo, P. Promdet, F. L. Heale, C. J. Carmalt and I. P. Parkin, *J. Mater. Chem. A*, 2019, **7**, 17604–17612.
- 340 M. J. Powell, D. B. Potter, R. L. Wilson, J. A. Darr, I. P. Parkin and C. J.

- Carmalt, *Mater. Des.*, 2017, **129**, 116–124.
- 341 M. J. Powell and C. J. Carmalt, *Chem. - A Eur. J.*, 2017, **23**, 15543–15552.
- 342 P. Marchand, I. A. Hassan, I. P. Parkin and C. J. Carmalt, *Dalt. Trans.*, 2013, **42**, 9406–9422.
- 343 K. Ramasamy, M. A. Malik, J. Raftery, F. Tuna and P. O'brien, *Chem. Mater.*, 2010, **22**, 4919–4930.
- 344 J. Akhtar, M. A. Malik, P. O'Brien and M. Helliwell, *J. Mater. Chem.*, 2010, **20**, 6116–6124.
- 345 S. Basharat, C. J. Carmalt, R. Binions, R. Palgrave and I. P. Parkin, *Dalt. Trans.*, 2008, 591–595.
- 346 E. S. Peters, C. J. Carmalt, I. P. Parkin and D. A. Tocher, *Eur. J. Inorg. Chem.*, 2005, **2005**, 4179–4185.
- 347 D. Sebastian, C. W. Yao and I. Lian, *Coatings*, 2018, **8**, 414.
- 348 J. Wang, Y. Lu, Q. Chu, C. Ma, L. Cai, Z. Shen and H. Chen, *Polymers (Basel)*, , DOI:10.3390/POLYM12040813.
- 349 G. Prasad, R. P. S. Chakradhar, P. Bera, A. A. Prabu and C. Anandan, *Surf. Interface Anal.*, 2017, **49**, 427–433.

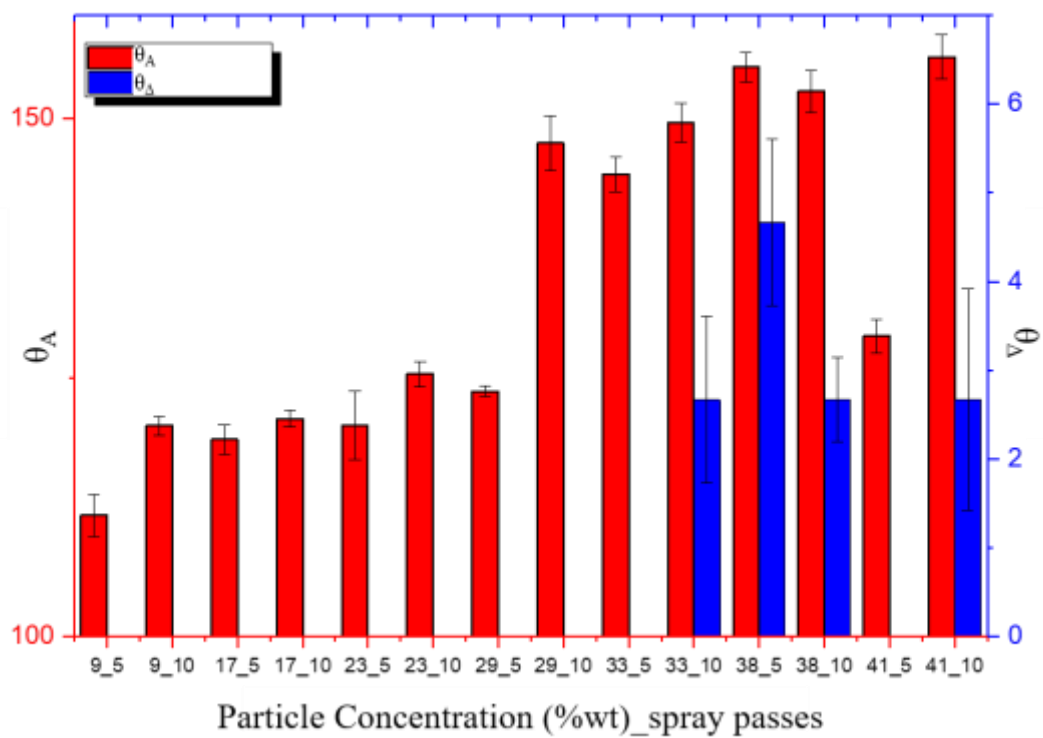
Appendix



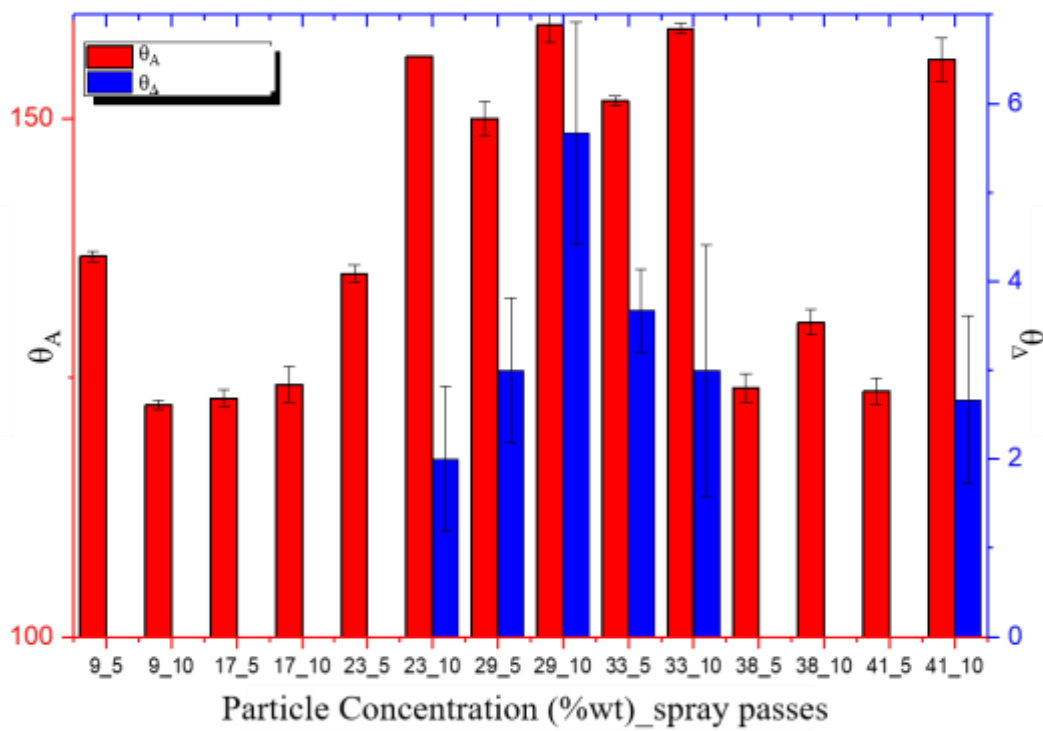


Supplementary Figure 1 Sonication study of 41 %w/w RX300 coating (a) Contact angle measurements (b) Photon transmission test results (c) AFM topographic analysis

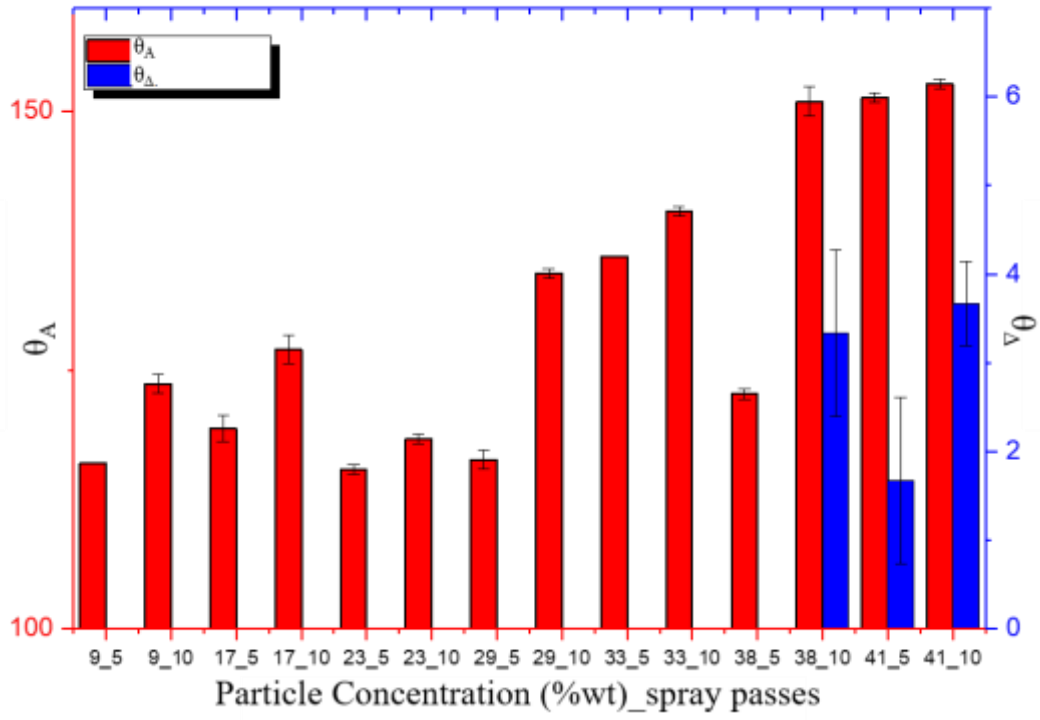
a)



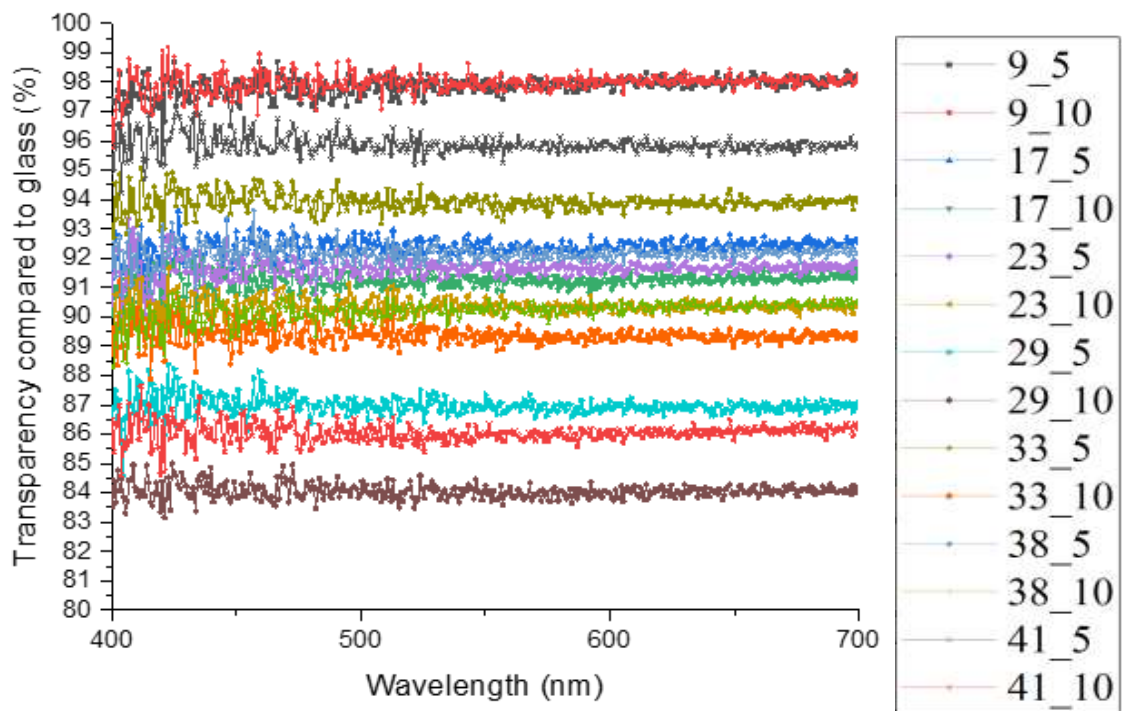
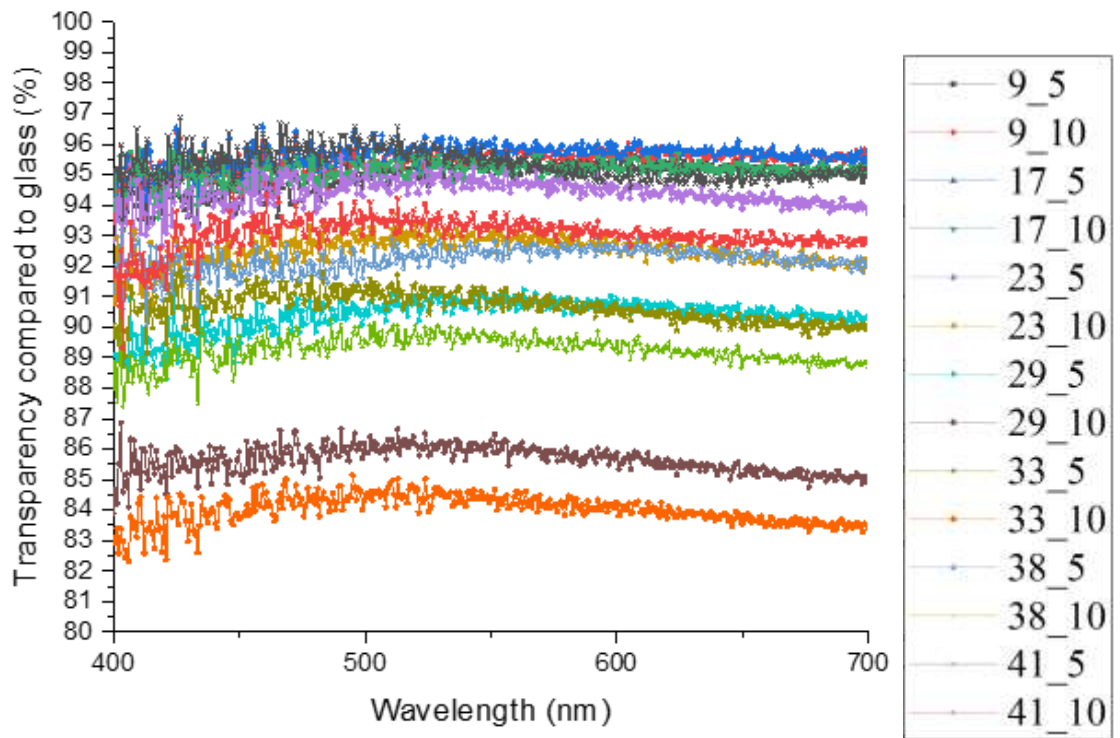
b)

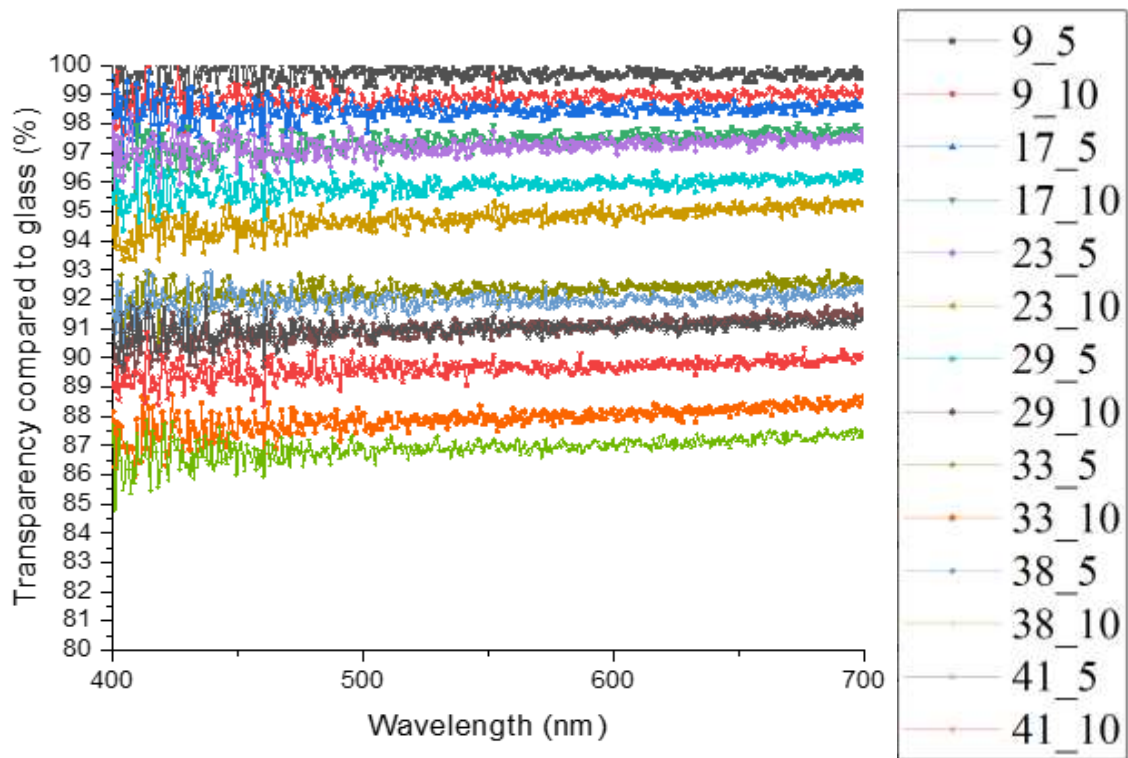


c)

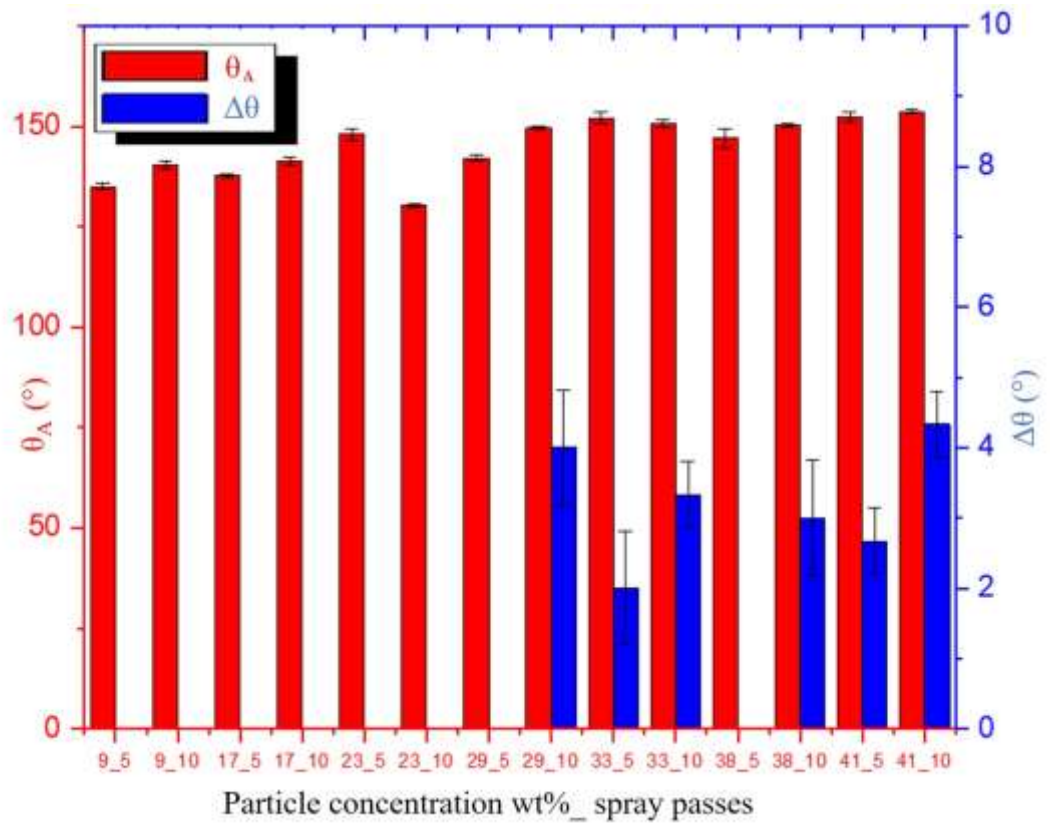


Supplementary Figure 2 Full contact angle analysis of the manufactured coatings

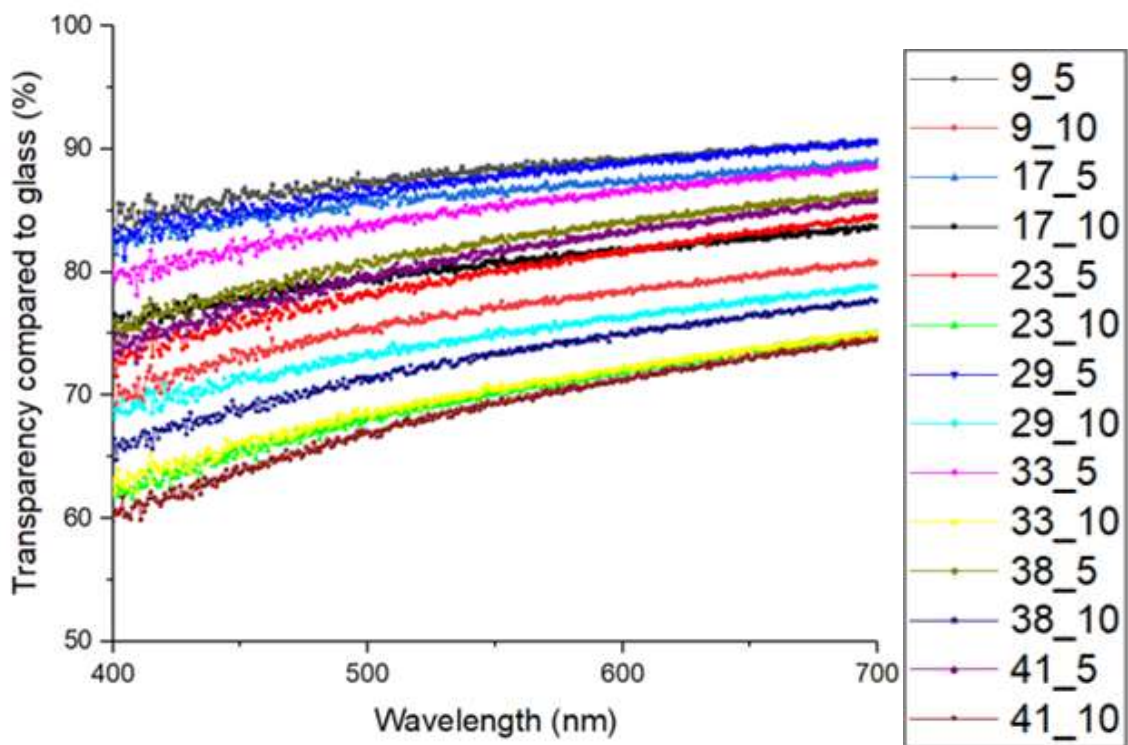




Supplementary Figure 3 Full optical transparency study conducted using photon transmission



Supplementary Figure 4 Complete concentration study of the Ti-PDMS hybrid for the RX300 particles



Supplementary Figure 5 Complete study of photon transmission for all the concentrations of the RX300 particles